博士論文

SINGLE-CELL-RESOLUTION MOUSE BRAIN ATLAS FOR WHOLE-BRAIN ANALYSIS OF CELLS

（一細胞解像度マウス脳アトラスによる全脳全細胞解析）

Tatsuya Murakami

村上 達哉

ABSTRACT

To understand the cellular components and circuits underlying complex physiological behaviors, a technique has been demanded which enables in situ identification and quantification of cellular properties at whole-organ scale. To that end, I revealed the chemical principle underlying tissue clearing by performing the comprehensive chemical screening. Based on the principles, several scalable tissue-clearing protocols were designed which allow whole-organ cell profiling, whole-body imaging including bone tissues, and human tissue imaging. Combining tissue clearing and tissue expansion, I finally identified all cells existing in a mouse brain, hence constructed three-dimensional single-cell-resolution mouse brain atlas (CUBIC-Atlas). With this point-based atlas, I holistically analyzed pharmacologically induced cellular activities in a mouse brain as the first demonstration of whole-organ analysis of cells. Such a bottom-up approach to understand an organ will elucidate the undiscovered relation between cell state and physiology.

PREFACE

The work presented in this thesis consists of two published studies after the introductory chapter, as described below. These studies focused on tissue clearing development, providing the community-wide analytical platform for whole-brain-cell analysis. I also included the general discussion and perspective of the studies.

Introduction - Introduction of the study, referring to the published manuscripts:

Tainaka K*, Murakami TC*, Susaki EA, Shimizu C, Saito R, Takahashi K, Hayashi-Takagi TA, Sekiya H, Arima Y, Nojima S, Ikemura M, Ushiku T, Shimizu Y, Murakami M, Tanaka KF, Iino M, Kasai H, Sasaoka T, Kobayashi K, Miyazono K, Morii E, Isa T, Fukayama M, Kakita A, Ueda HR. Chemical Landscape for Tissue Clearing based on Hydrophilic Reagents. Cell Reports 24, 2196-2210, 2018 (* co-first author).

Murakami TC, Mano T, Saikawa S, Horiguchi SA, Shigeta D, Baba K, Sekiya H, Shimizu Y, Tanaka KF, Kiyonari H, Iino M, Mochizuki H, Tainaka K, Ueda HR. Three-dimensional Single-cell-resolution Whole-brain Atlas Using CUBIC-X Expansion Microscopy and Tissue Clearing. Nature Neuroscience 21, 625-637, 2018.

All co-authors of these research articles agreed with including the corresponding published study in this doctoral thesis. I also referred Tainaka et al., Annu. Rev. Cell Dev. Biol., 32:713–41, 2016. I contributed a part of the paper.

Results 1 - The result of “Chemical Landscape for Tissue Clearing based on Hydrophilic Reagents” and the screening result of “Three-dimensional Single-cell-resolution Whole-brain Atlas Using CUBIC-X Expansion Microscopy and Tissue Clearing”. In this study, I performed comprehensive chemical screening to reveal chemical principles underlying the hydrophilic tissue clearing. The study was designed together with K. Tainaka and H.R. Ueda. K. Tainaka performed the chemical profiling and I statistically analyzed profiled results. C. Shimizu performed the part of the experiments.

Results 2 - The result of “Three-dimensional Single-cell-resolution Whole-brain Atlas Using CUBIC-X Expansion Microscopy and Tissue Clearing”. The study introduces a new type of analytical platform for single-cell-resolution whole-brain-cell analysis. T. Mano constructed the customized light-sheet microscopy described in the study.

Discussion – General discussion and perspective of the studies.

ACKNOWLEDGMENTS

I am deeply grateful to my research adviser Hiroki Ueda for the continuous support of my Ph.D. study. His guidance helped me in all the time of research. Without his scientific instruction, I could not be an independent researcher. I am also grateful to Hiroki for providing an ideal research environment, where all of the members of our group became united to conduct scientific experiments.

I received enormous amounts of instruction by Kazuki Tainaka, who was the member of the lab at the time I joined the group. He mentored me from a detail of an experiment to the philosophy of science. I also thank Etsuo Susaki, Koji Ode, Shoi Shi, Chika Shimizu, Tomoyuki Mano, Shu Saikawa, Shimpei Kubota, Akihiro Kuno, and other lab members for their technical supports.

Japanese Society for the Promotion of Science (JSPS) financially supported my doctoral study by providing Research Fellowship for Young Scientists. Graduate Program for Leaders in Life Innovation (GPLLI) supported my travels for international conferences and talks.

I would like to dedicate this work to my family. My mother and father are the biggest supporters of my life. They were happy to allow me to pursue my carrier as a scientist in spite of unclear future of young Japanese scholars. Finally, I thank my wife, Erika, for the opportunity to figure out life together.

TABLE OF CONTENTS

INTRODUCTION

Since Robert Hooke's discovery of cells about 350 years ago, researchers have explored the diversity of this fundamental unit of lives. So far, various types of cells were identified based on their structures, function, and location. Yet, comprehensive characterization of cells in organ/body has been challenging due to the overwhelming amount of cells [37.2 trillion in case of a whole-human body, (Bianconi et al., 2013)]. To that end, various projects have been launched including Human Cell Atlas (Regev et al., 2017). These projects promote understanding of our cells by utilizing an emerging technique of nucleic acid sequencing. However, the lack of spatial resolution of these techniques has prevented system-level understanding of organs. The technical platform has been demanded to achieve three-dimensional cell profiling with single-cell resolution.

Whole-organ and whole-body imaging by tissue clearing

Emerging whole-organ imaging techniques have facilitated our understanding over a mammalian body (Susaki and Ueda, 2016). The initial attempts of single-cell-resolution whole-organ imaging began with the reconstruction of the two-dimensional sectioned histological sample (Amato et al., 2016; Ragan et al., 2012). By this mean, researchers have revealed gene expression status of cells in reconstructed whole-brains (Lein et al., 2007). Though this technique demonstrated a potential approach for whole-organ comprehensive profiling of cells,

inevitable artifact coming from discontinuities of sections was bottle-neck to achieve single-cell-resolution imaging in a three-dimensional context. More importantly, the choice of molecular labeling for cellular phenotyping is mainly limited to fluorescent protein or light-up molecular dye because labeling on every section requires a large amount of time and make it impractical to perform in whole organ/body.

An alternative solution is tissue clearing. Once the organ/body is rendered transparent, we are able to inspect the inside of the biological specimen. This idea was first proposed around 100 years ago by a German physician, Spalteholz (Spalteholz, 1914), and various clearing methods were proposed so far (**Table 1**). Historically, tissue clearing has been performed with organic solvent, and minor modification has been made to achieve higher transparency. Within the clearing protocols using organic solvent, BABB (benzyl alcohol/benzyl benzoate) was the first protocol which was applied for clearing of a mouse brain (Dodt et al., 2007). In that study, Dodt and colleague first demonstrated whole-mouse brain imaging using light-sheet florescence microscopy. To improve the optical transparency and compatibility with fluorescent protein of BABB, 3DISCO was proposed (Becker et al., 2012; Ertürk et al., 2012). 3DISCO was further modified for clearing of whole-mouse/rat body (Pan et al., 2016; Cai et al., 2019) or for whole-brain immunostaining (Renier et al., 2016; Renier et al., 2014). The limitations of organic solvent were the incompatibility with long-term imaging of fluorescent protein and high autofluorescence caused by residual biological pigments. To overcome these issues, exploration in tissue clearing with hydrophilic reagents began. Historically, various hydrophilic chemicals were tested to clear human skin for clinical purposes first by Tuchin and colleagues (Bakutkin et al., 1995; Zhu et al., 2013) (Bashkatov et al., 1999; Tuchin et al., 1999; Tuchin et al., 1996; Tuchin et al., 1997; Tuchin et al., 2002; Zimnyakov et al., 1996). After the pioneering work of Tuchin and colleagues, the researchers repeatedly compared hydrophilic chemicals for clearing of skins (Chance et al., 1995; Choi et al., 2005; Jiang and Wang, 2004; Vargas et al., 2001; Vargas et al., 1999; Wang et al., 2001; Xu and Wang, 2003). Chiang and colleague further applied hydrophilic chemicals for clearing of a brain, using FocusClear (Chiang et al., 2001), opening a new research field in anatomy and neuroscience (Aoyagi et al., 2015; Hirshburg et al., 2007; Hou et al., 2015; Kuwajima et al., 2013; Liu and Chiang, 2003; Staudt et al., 2007; Tsai et al., 2009). Because the hydrophilic chemicals were less toxic to biomolecules than organic solvent, they were applied for imaging of fluorescent protein (Hama et al., 2011; Ke et al., 2013). Though the clearing performance with hydrophilic reagents was inferior to organic solvent at the beginning, efforts have been made to enhance the transparency

(Susaki et al., 2014), and some researches demonstrated clearing of a whole body of adult mouse (Tainaka et al., 2014; Yang et al., 2014). There are numbers of clearing regents belong to this hydrophilic group, those are well summarized in the previously published review articles (Richardson and Lichtman, 2015; Tainaka et al., 2016). To accelerate the clearing speed of hydrophilic reagents, researchers devised clearing protocols utilizing physicochemical forces as represented by CLARITY (Chung et al., 2013), which uses electric repulsion or SWITCH and MAP (Ku et al., 2016; Murray et al., 2015), which use excessive heat. Since the aggressive clearing changes molecular properties of tissues, these protocols often accompany with hydrogel embedding such as acrylamide and glutaraldehyde. This embedding of biological tissue in hydrogel is originally proposed by Hausen and Dreyer at the begging of 1980s, for the aim to preserve antigeneity of native proteins (Hausen and Dreyer, 1981). However, the additional procedures of the hydrogel embedding and requirements for special devices (Chung et al., 2013; Kim et al., 2015a) reduced the reproducibility and convenience of clearing.

Contrary to the varieties of tissue clearing, they follow the similar procedures, (a) removal of light-scattering molecules (b) removal of light-absorbing molecules, and (c) homogenization of refractive index (RI), prior to obtaining final transparent tissues (**Figure 1A**). Because biological tissues composed of molecules with distinct optical characteristics (e.g. water, lipid, and protein), an initial step toward tissue clearing is to remove unwanted molecules which could disturb the homogenization of RI. We delipidate tissue for this aim because proteins, which deliver biological function, are the major interests of research and because the major cellular molecules beside proteins are lipids (Susaki and Ueda, 2016). In case the tissue includes a bone, additional procedure for decalcification enhances transparency (Greenbaum et al., 2017; Treweek et al., 2015). Removal of light-absorbing molecules is also a major consideration (Tuchin, 2015), because they not only prevent light transmission but also cause autofluorescence, which could deteriorate the quality of imaging. The last step of tissue clearing is a homogenization of RI of the tissue (Tuchin, 2015). We use solutions with high refractive index ranges from 1.44 – 1.56 in most cases (Tainaka et al., 2016). This RI is supposed to be identical to that of residual protein after delipidation or decalcification.

In addition to these clearing-prone investigations, a novel concept using tissue expansion was recently proposed to further advance detailed inspection in three-dimensional tissue. By harnessing the nature of swellable polyelectrolyte hydrogel, which was thoroughly investigated by Toyoichi Tanaka in the late 1970 (Tanaka et al., 1980), Boyden group

physically expanded biological tissues by embedding them in hyperhydrating polymer (Chen et al., 2015). The method, termed expansion microscopy, achieves super-resolution imaging over diffraction limit. An additional benefit of tissue expansion is optical transparency of hydrated tissue. Originally, researchers have utilized tissue hydration for tissue clearing (Hama et al., 2011) (**Figure 1B**). Expansion microscopy further assisted clearing by magnifying the scale of expansion (Chen et al., 2015; Treweek et al., 2015). The polymer-based expansion microscopy was even applied to whole organs (Ku et al., 2016; Gao et al., 2019; Park et al., 2018) though the application of hyperhydrating polymer complicates the molecular labeling procedure (Chen et al., 2015; Ku et al., 2016). Thus, the expansion without external polymer was demanded, but large expansion has not been observed without polymer.

Considering the potential combination with expansion microscopy, tissue clearing with hydrophilic reagent has advantages over organic solvent because organic solvent causes tissue shrinkage by dehydrating tissue (Pan et al., 2016). However, a limited knowledge had been shared so far on the chemical principle of hydrophilic tissue clearing/expansion. The researchers had to develop clearing/expansion protocols by relying on a serendipitous discovery of new chemical reagents. This leads to the lack of the variation of chemical components contrary to the number of proposed hydrophilic clearing reagents (Susaki and Ueda, 2016; Tainaka et al., 2016). The popular components are detergents (e.g. Triton, SDS), alcohols (e.g. glycerol, polyethylene glycol, butanediol, trimethylopropane, sorbitol, xylitol), sugars (e.g. glucose, fructose, sucrose), dimethyl sulfate, 2,2'-thiodiethanol, aminoalcohol, urea, and contrast agents (e.g. diatrizoic acid, Histodenz^{TM}, iodixanol) (Tainaka et al., 2016). Of these molecules, aminoalcohol is widely used for decoloring tissue (Greenbaum et al., 2017; Tainaka et al., 2014). For decalcification, EDTA, which is a chelating agent of calcium ion, is the only option. To achieve improved tissue-clearing techniques, it is important to understand the effective functional groups and chemical properties of each clearing step. Such comprehensive chemical profiling will lead a rational design of clearing reagents.

Single-cell-resolution whole-brain atlas

The next challenge toward whole-organ/body analysis of cells is the development of a methodology to describe the cellular information over an entire organ/body in single-cell resolution. So far, the researchers have evolved single-cell-resolution imaging technique in a large organ using optical sectioning with light-sheet fluorescent microscopy or optical

projection tomography (Dodt et al., 2007; Keller and Ahrens, 2015; Ntziachristos, 2010; Sharpe, 2004). The update of image processing to extract single-cell information from large volumetric imaging datasets enabled comprehensive profiling of cells (Amat et al., 2015; Amat et al., 2014; Chhetri et al., 2015). These advancements both in imaging and informatics facilitated researchers to work on whole-organ/body analysis of cells. However, the large data size of volumetric images has prevented us from sharing data. Therefore, there is an urgent need for building an analytical platform which enables the researchers to collaboratively work on whole-organ/body analysis of cells. Such platform enables researchers to reanalyze published data, further deepening system-level understanding of an organ/body. To that end, editable and sharable whole-organ/body atlas is wanted which can accommodate any cellular information.

So far, a number of mammalian brain atlases including non-human primates have been constructed (Amunts et al., 2013; Calabrese et al., 2015; Dong, 2008; Hawrylycz et al., 2012; Johnson et al., 2010; Mikula et al., 2007; Papp et al., 2014; Rohlfing et al., 2012), and provided useful anatomical platforms. These mammalian brain atlases can be used 1) as a platform for mapping different cellular populations over the entire brain when combined with genome-wide expression data by in situ hybridization (Lein et al., 2007) and microarrays (Kasukawa et al., 2011; Okamura-Oho et al., 2012), 2) as a platform for mapping cellular activities by measuring gene expression of immediate early genes (Kim et al., 2015b; Tatsuki et al., 2016; Vousden et al., 2015), and 3) as a platform for mapping cellular connections when combined with neural projection analysis based on adeno-associated-virus (AAV) (Oh et al., 2014) or rabies virus (RV) (Menegas et al., 2015; Velez-Fort et al., 2014). Although these image-based atlases could provide high-resolution information, enormity of the data prevents flexible editing and update of the atlas. Importantly, these atlases were not designed to accommodate cellular information, thus spatial resolution for systematic comparison of multiple brains is limited in the level of anatomical areas. In addition, the anatomical areas were mainly defined by histological observation, not by cellular function. Considering that the cell is a unit of life, a cell-based atlas would provide one of the attractive alternatives to image-based atlases. Such a cell-based atlas will greatly reduce the data size, resulting in a convenient platform for sharing and distribution of data. The atlas is potentially editable via an open-source platform, and therefore is easily updated by overlaying various cellular functions (e.g. activity, gene expression, cell type, and neural connection). To construct a single-cell-resolution mouse brain atlas, it is essential to accurately identify entire cells in the whole brain. To this end, the imaging technique satisfies both subcellular resolution and whole-brain-scale coverage has been awaited.

In this dissertation, I propose two research tools to promote involvements of research community in whole-organ/body analysis of cells. In the first part of the study, I propose a universal strategy to develop scalable tissue-clearing technique by revealing the chemical principles of tissue clearing. In the first part of the thesis, I comprehensively evaluated clearing abilities of more than 1600 hydrophilic chemicals using high-throughput evaluation systems suitable for each chemical process. I investigated five elemental clearing factors (i.e., delipidation, decoloring, refractive index (RI) matching, decalcification, and hyperhydration) to allow for understanding their independent contributions in the tissue-clearing process. Profiling of the screened chemicals revealed important chemical factors: salt-free amine with high logP for delipidation, N-alkylimidazole for decoloring, aromatic amide for RI matching, protonation of phosphate ion for decalcification, and five-membered heterocycle for hyperhydration. By strategically integrating optimal chemical cocktails, I obtained a series of updated CUBIC protocols that efficiently cleared mouse organs, mouse body including bone, and large primate tissue samples, including marmoset brain and human tissue samples over 10 cm^3.

In the second part of the thesis, I proposed an editable and pointillistic mouse brain atlas with single-cell resolution by an intensive tissue clearing method combined with tissue expansion. Describing whole-mouse brain as an ensemble of cellular points with less than 3 GB of data was achieved by subcellular-resolution imaging of a nuclear-stained brain and automatic detection of cells. By referring anatomical annotations of Allen Brain Atlas (Dong, 2008), this single-cell based brain atlas, termed CUBIC-Atlas, allowed counting the number of cells in the annotated anatomical region. The region-specific cell counting of developing mouse brain revealed a significant decrease in cell number in the cerebral visual and primary somatosensory cortical area during early post-natal development. By probabilistic mapping of pharmacologically activated neural cells onto CUBIC-Atlas, I also discovered a functionally distinct brain region in the hippocampal dentate gyrus. I demonstrated the new approach for whole-organ/body-cell analysis. I believe that the study will accelerate system-level understanding of our body, and pioneer the prospective digitalization/standardization of lives.

MATERIALS AND METHODS

MODEL SYSTEMS AND PERMISSIONS

Mice Model

For the chemical screening, the organs of adult mice (C57BL/6N, ICR, or BALB/c-nu/nu) were used. The mice were sacrificed by an overdose of pentobarbital (> 100 mg/kg, Nacalai Tesque, 02095-04), then transcardially perfused with 15 ml of PBS (pH 7.4) and 20 ml of 4% paraformaldehyde (PFA, Nacalai Tesque, 02890-45) in PBS. Organs were dissected, then post-fixed with 4% PFA-PBS at 4 ℃ overnight. The fixed organs were then washed with PBS prior to the experiments. If necessary, the post-fixed samples were immersed in 20% sucrose in PBS at 4 ℃, and then stocked in O.C.T. compound at -80 ℃ until use.

The Htr5b-tTA (Tanaka et al., 2012):tetO-YC (Kanemaru et al., 2014) (7 weeks old), Plp-tTA (Inamura et al., 2012):tetO-ChR2EYFP (Tanaka et al., 2012) (10 weeks old), Mlc-tTA (Tanaka et al., 2010):tetO-YC (11 weeks old), Drd1-mVenus (Nagai et al., 2016) (7 months old), Th-EGFP (Matsushita et al., 2002) (6 months old), Thy1-YFP-H (Feng et al., 2000) (6 months old), and P(CAG)-EGFP (Okabe et al., 1997) (8 weeks old) mouse strains were used to observe the expression patterns of fluorescently labeled cells in the brain. P(CAG)::mRFP was transduced into mouse brain (8 weeks old) by in utero electroporation as described previously (Hayashi-Takagi et al., 2015). 4-month-old R26-H2B-EGFP male mice (Abe et al., 2011) (Accession No. CDB0238K, http://www.clst.riken.jp/arg/reporter_mice.html) were used for observation of influence of delipidation over nuclei. 8-week-old male mice of C57BL/6J were used to build the whole brain atlas with single-cell resolution. C57BL/6N mice were used to analyze whole-brain cell profiling over different aged mice. 1-week-old male mice were purchased from CLEA Japan, and 3-, 8-week- and 6-month-old male mice were from Japan SLC, Inc.

The human breast cancer cells, MDA-MB-231-5a-D (MDA-231-D), are a highly metastatic clone derived from MDA-MB-231 (Ehata et al., 2007). We established MDA-231-D cells that co-expressed luciferase and mCherry according to our recent report (Kubota et al., 2017). To

elicit experimental bone metastasis by intracardiac (i.c.) injection, MDA-231-D cells (MDA-231-D: 1×10^5 cells/mouse) were injected into BALB/c-nu/nu mice (4-weeks old, female) by puncture into the left ventricle of heart. Mice were sacrificed 4 or 5 weeks after injection.

All experimental procedures and housing conditions were approved by the Animal Care and the Use Committee of the Graduate School of Medicine, University of Tokyo, the Animal Care and the Use Committee of Graduate School of Medicine, Osaka University, and by the Animal Use and Care Committee of Niigata University, and all of the animals were cared for and treated humanely in accordance with the Institutional Guidelines for Experiments using animals.

Marmoset

We studied an adult marmoset at the age of 12 months. Animal was maintained and handled in accordance with the recommendations of the United States National Institutes of Health, and all procedures were approved by the Animal Care and Use Committee of the Graduate School of Medicine, Kyoto University, Japan.

Human Tissue

Human tissues used for this study were obtained from 10 patients (59–90 years old; 9 males and 1 female). Written informed consent for autopsy including the use of tissue for research purposes was obtained from the next of kin. Experiments using human tissues were approved by the institutional review boards of Osaka University School of Medicine, Osaka, Japan, the Graduate School of Medicine, University of Tokyo, Tokyo, Japan, and Niigata University School of Medicine, Niigata, Japan.

METHOD DETAILS FOR RESULTS 1

High-throughput Chemical Screening

Delipidation

To comprehensively assess the ability of chemicals to solubilize lipids in a high-throughput manner, I used a previously reported method (Susaki et al., 2014). In brief, 20 μl of homogenized mouse brain was mixed with 130 μl of each 10%(wt/wt) chemical solution in 96-

well plates and incubated at 37 ℃ overnight. After gentle shaking, the OD600 of the mixture was measured with a PowerWave XS (Bio-Tek). The lipid solubility score was calculated as follows. First, the OD600 of each chemical solution alone was subtracted from the OD600 of the mixture. The lipid solubility score was then determined by plotting the resulting OD600 on a line created by assigning the OD600 of PBS-suspension as 0.0 and the OD600 of the chemical solution alone as 1.0. Among the non-detergent and salt-free chemicals, those that were colored (OD600 $\geq$ 0.1), of low solubility, or lacked a LogP value (octanol-water partition coefficient) were excluded from the chemical profiling. To examine the relationship between tissue phospholipid or cholesterol content and transparency, adult mouse half brains were weighed and then immersed in various delipidating CUBIC chemicals. After 1 day of delipidation at 37 ℃ with gentle shaking, the brains were washed with PBS at room temperature for a half day with gentle shaking. The washed samples were then subjected to phospholipid or cholesterol quantification. To quantify the phospholipid content, the samples were thoroughly crushed, then sonicated in 10% Triton X-100 in PBS to obtain a homogenized suspension. After adjusting for the total weight of each sample, the phospholipid was quantified with LabAssayTM Phospholipid (Wako Pure Chemical Industries Ltd., 296-63801) according to the instruction manual, with OD600. The absolute amount of phospholipid was determined by fitting the OD600 value to a standard curve generated by a serially diluted pure phospholipid standard. The cholesterol content was similarly quantified using LabAssayTM Cholesterol (Wako Pure Chemical Industries Ltd., 296-65801).

To measure the relative transparency, delipidated samples were washed with PBS, and immersed in modified Sca*l*eCUBIC-2 [22.5 wt% antipyrine (Tokyo Chemical Industry, D1876), 22.5 wt% sucrose (Nacalai Tesque, 30403-55), 25 wt% urea (Nacalai Tesque, 35904-45), and 10 wt% triethanolamine (Wako Pure Chemical Industries Ltd., 145-05605)] overnight at room temperature with gentle shaking. The transmittance was quantified with a Spectral Haze Meter SH 7000 (Nippon Denshoku Industries), as described in our previous study (Tainaka et al., 2014).

After comprehensive screening for effective delipidation chemicals, I further assessed their delipidation ability when used in combination with other chemicals. Adult mouse half brains, adult mouse kidneys, and human brain blocks were used to evaluate the chemicals' delipidation ability. Each tissue was weighed prior to the experiment if required for normalization. The mouse tissues were immersed in the cocktails for more than 1 day at 37 ℃ with gentle shaking,

while the human tissues were immersed in the cocktail for more than 4 days at 37 ℃ with gentle shaking. After delipidation, the samples were washed with PBS overnight. If required to improve the transparency of the tissue, the samples were then subjected to RI-matching procedures, consisting of 1:1-diluted CUBIC-R for one day followed by CUBIC-R for one more day. The washed samples were then subjected to phospholipid quantification as described above.

Decoloring Ability

To comprehensively evaluate the decoloring ability of chemicals in a high-throughput manner, I used a previously reported method (Tainaka et al., 2014) with minor modifications. Because a large amount of blood was required for this screen, I used horse blood (Kohjin-Bio Co., Ltd., 12070110). Prior to screening, the blood was fixed in an equal volume of 8% PFA in PBS, and the mixture was then diluted 4-fold with PBS. The fixation was performed at 37 ℃ for 16 hours. After removing clots by filtration, the sample was centrifuged at 1500 G for 3 minutes, and the supernatant was discarded. The pellet was washed with PBS. This centrifugation-washing procedure was repeated for a total of three times. The final pellet was diluted in the same amount of PBS as the original volume of blood. For the comprehensive screening, 50 μl of fixed blood and 150 μl of 10%(wt/wt) CUBIC chemical solution were mixed in 96-well plates. The samples were gently shaken for 1 day at 37 ℃, then spun at 1500 G for 5 minutes, and 100 μl of the supernatant was transferred to another 96-well plate. OD420 and OD700 were measured with an EnSpire plate reader (Perkin Elmer, USA). To calculate the decoloring score, I first subtracted the OD700 from the OD420 to account for light scattering. The resulting value was then divided by the value obtained for Quadrol. Among the non-detergent and salt-free chemicals, low-solubility chemicals were excluded from the chemical profiling. After this comprehensive screening for decoloring chemicals, I used adult mouse spleen to examine the chemicals' decolorization ability in biological tissues. An adult mouse spleen was immersed in 3 ml of the CUBIC chemical solutions at 37 ℃ for 3 hours. Then, 100 μl of each supernatant was subjected to OD400 measurement.

RI Matching

To screen for chemicals with effective RI matching, I assumed that such chemicals would satisfy at least two conditions: colorless with a high RI in 10%(wt/wt) solution, and highly soluble in water. To first identify chemicals with a high RI in 10%(wt/wt) solution, I measured the OD400 with a PowerWave XS and the RI value of each CUBIC-chemical solution with an Abbe refractometer (Atago, DR-A1, Japan). Next, I examined whether the chosen chemicals were soluble in water at 60-70 wt%. The candidates satisfying these two criteria were then evaluated for their clearing performance in mouse lung. Prior to the RI-matching step, the lungs were delipidated with Sca*l*eCUBIC-1 for 2 weeks at 37 ℃. The lungs were dissected into small (3-5-mm) blocks, which were then immersed into 400 μl of 60-70 wt% CUBIC chemical at room temperature overnight. The resulting samples were transferred into 96-well plates, and the OD600 was measured with a PowerWave XS. For combinatorial screening, the whole lungs were first immersed in 2 ml of the chemical cocktail diluted 1:1 with deionized water, then gently shaken at room temperature overnight. The lungs were then immersed in 2 ml of the chemical cocktail with gentle shaking at room temperature overnight.

Decalcification

To measure the decalcifying ability of a chemical, I used a screen based on hydroxyapatite (HAp), a major component of bone, as a surrogate for bone. Because the specific gravity of HAp (about 3.16) is much higher than that of water (= 1), I dissolved 200 mg/ml or 100 mg/ml HAp in 40%(v/v) glycerol to prevent its precipitation during the experiments. I then mixed 20 μl of homogenized HAp solution with 130 μl of the 10%(wt/wt) chemical solutions in 96-well plates. After gentle shaking at 37 ℃ overnight, the plates were centrifuged at 1500 G for 3 minutes, and the OD600 of the mixture was then measured with a PowerWave XS. The decalcification score was calculated by plotting the resulting OD600 on a line in which the OD600 of PBS-HAp suspension was 0.0 and the OD600 of EDTA-2Na-treated suspension or EDTA titrated with CU#0414-treated suspension was 1.0.

Hyperhydration

I used the gelatin type B (Nacalai Tesque, 16631-05) in gelatin-based assay. To prepare gelatin blocks, 10% gelatin aqueous solution was prepared by gentle heating until gelatin powder dissolved, and 1 ml of the solution was dispensed into square shaped dies. Gelatin was gelated

at 4℃ overnight. After gelation, resulting gelatin blocks were fixed by 4% PFA in PBS at 4℃ for more than 12 hours with gentle shaking, and washed with PBS extensively. Gelatin blocks were treated with 10 ml of each chemical at room temperature with gentle shaking for 1 day. I measured 2D projection area (mm^2) of the gelatin blocks by ChemiDocTM XRS Plus (Bio-Rad), and estimated the volume supposing gelatin blocks were isotopically swelled or shrunk by each chemical treatment.

To measure the brain swelling ratio, brain samples of 8-week-old mice were initially delipidated by Sca*l*eCUBIC-1 as mentioned above. Delipidated brains were cut to make hemisphere brains. Hemisphere brains were treated with 10 ml of each chemical at room temperature with gentle shaking for 1 day. I measured 2D projection area (mm^2) of the hemisphere brains by ChemiDocTM XRS Plus (Bio-Rad), and estimated the volume assuming that hemisphere brains were isotopically swelled and shrunk by each chemical treatment. The volume of hemisphere brains was calculated by simply taking the 3/2 power of the 2D projection area. Customized python code was used to quantify the 2D projection area. Initially, Sobel filter was applied to give sufficient contrast to the edges, followed by manually adjusting a threshold to determine the contour of the brains. Finally, I measured inner area as a 2D projection area. Swelling ratio was calculated by the ratio of the obtained volume between brain samples before- and after-chemical treatment.

I measured 2D projection area of whole brains instead of hemisphere brains, and evaluated time course of swelling ratio of whole-brain samples. The volume was estimated as described above. I used the size of PFA-fixed whole brain as an original brain size.

Because isoelectric points of gelatin are different depending on the manufacturing process, I measured both of gelatin type A (MP Biomedicals, 901771) and gelatin type B (Nacalai Tesque, 16631-05), which are processed under acidic and basic condition, respectively. I prepared 0.1% concentration of gelatin in water, and then fixed by 0.8% PFA in water at 4℃ overnight. As a control, I used 0.1% lysozyme aqueous solution (Wako Pure Chemical Industries Ltd., 122-02673). Brain protein was prepared as follows. Adult mouse brains were removed from the skull, chopped with a blade, suspended and sonicated in extraction buffer [20 mM HEPES, 100 mM NaCl, 0.01 M DTT, and protease inhibitors (1× cOmpleteTM, EDTA-free Protease Inhibitor Cocktail, Roche, 05056489001)]. 20 ml volume of the resulting brain suspension (from 10 brain samples) was centrifuged at 12,000g for 15 minutes, and 1 ml of the supernatant was mixed with 14 ml of cold 80% (v/v) acetone and 20% (v/v) methanol solution. The

suspension was incubated at 4 ℃ for 90 minutes. After centrifugation, the pellet was washed with 20 ml of acetone and adequate volume of methanol, and then dried at 37 ℃ over 30 minutes. The pellet was fixed by 2 ml of 4% PFA in PBS at 4 ℃ with gentle shaking overnight. After PBS washing, the pellet was stored in 2 ml of stock solution (20 mM HEPES, 100 mM NaCl, 1 mM EDTA, 1 mM DTT, 0.1% NaN3, and protease inhibitors, pH 7.4). The fixed brain protein was diluted to 1/1000 in water just before zeta potential measurement. Zeta potential was measured with ZetaSizer Nano ZS (Malvern). pH was adjusted by titrating 0.05 M NaOH or 0.05 M HCl to samples. The measured zeta potentials were plotted and fitted to fourth-order polynomials. The isoelectric points were determined by calculating a crossing point of the polynomial with the x-axis.

For high-throughput screening of swelling reagents, I measured 975 nm absorption of gelatin type B (Nacalai Tesque, 16631-05) gel. I used 975 nm absorption because water absorption of near infrared shows a peak around 975 nm (Hale and Querry, 1973), and this peak is widely used to determine optical pathlength of water (Cope et al., 1989; Wray et al., 1988). 9% gelatin type B mixed with 0.8% PFA was prepared. I chose this low concentration of PFA because the hard fixation by 4% PFA caused less swelling of gelatin, hindering the accurate quantification of chemical swelling abilities. 100 μl of the mixture was immediately dispensed into each well of the 96-well plate. The plates were incubated at 4 ℃ overnight. After gelation, gelatin plates were washed with water. For calibration, 100 μl of water was put onto the gelatin, and the 975 nm absorbance was measured with PowerWave XS (Bio-Tek). After removal of the water, 170 μl of 10% (w/w) chemicals were put onto the gelatin, and bubbles were carefully removed. The plates were incubated at room temperature for 3 days with sealing. After incubation, the supernatants were thoroughly removed by washing plates with water for three times. Then, I put 100 μl of water onto the gelatin to avoid surface scattering and refraction. The 975 nm absorbance was measured again with PowerWave XS. Because some chemicals produced precipitation in or on gelatin during incubation, I also measured the 900 nm absorbance as an index of scattering. The same experiments were performed twice. I excluded the chemicals which showed more than 0.1 of the 900 nm absorbance. I linearly normalized the values of 975 nm absorbance of the gel by the value of blank (= 0.0) and the urea-treated gel (= 1.0). Then, I converted the 975 nm absorbance to in-well gelatin swelling score.

Quenching of Fluorescent Proteins (FPs) by Chemicals

The pattern and expression level of FPs in tissue varies due to individual differences, making it difficult to accurately quantify the FP quenching of chemicals, while an in vitro FP quenching assay is more quantitative and has higher reproducibility. Moreover, clearing protocols usually involve some kind of chemical fixation (e.g., PFA, glutaraldehyde, or a Clarity-related embedding hydrogel), and the FP signals can be dramatically affected by the fixation conditions (e.g., the fixative chemicals, concentration, duration, and temperature). For these reasons, I conducted an in vitro FP quenching assay in this study.

To comprehensively measure the effect of CUBIC chemicals on the fluorescence intensity of fluorescent proteins (FPs), I used EGFP and Sirius. Recombinant EGFP at 0.05 mg/ml and Sirius at 0.2 mg/ml were prepared in PBS. Then, 20 μl of the FP solutions were mixed with 130 μl of each 10%(wt/wt) chemical solutions in 96-well plates. After gentle shaking at 37℃ overnight, I measured the 507-nm emission for EGFP by 488-nm excitation, and the 427-nm emission for Sirius by 355-nm excitation, with an EnSpire. A series of standard buffers with a pH range of 2-14 was prepared, including 200 mM glycine (pH 2.5, 3, 3.5, 12, 12.5, and 13; Nacalai Tesque, 17109-35), 100 mM citrate (pH 4, 4.5, 5, 5.5, 6, 6.5, and 7; sodium citrate tribasic dehydrate, Sigma-Aldrich, S4641), PBS (pH 7.5 and 8), 10 mM borate (pH 8.5, 9, 9.5, and 10; borate reference solution, Horiba), 50 mM NaHCO3 (pH 10.5 and 11; Nacalai Tesque, 31212-25), and 100 mM NaH2PO4 (pH 11.5; Nacalai Tesque, 31718-15). To further demonstrate the quenching effect of each CUBIC protocol, I also used 16 mg/ml YFP and 15 mg/ml mCherry. The fluorescence intensities of these FPs were measured as described above, using the appropriate excitation and emission wavelengths.

pH evaluation

Because pH can significantly influence the chemical parameters in tissue clearing, I established a high-throughput pH measurement assay using universal pH indicator paper (As One Corp., 1-1254-01). The papers were cut into circles and placed in the bottom of 96-well plates, followed by the application of 2 μl of CUBIC chemicals. The absorbance at 550, 570, 610, and 660 nm was measured with an EnSpire, then the pH was predicted according to a regression model.

To establish the regression model, I prepared a series of standard solutions with a pH range of 0-14: 200 mM KCl (pH 1, 1.5, and 2; Nacalai Tesque, 28514-75), 200 mM glycine (pH 2.5, 3,

3.5, 12, 12.5, and 13; Nacalai Tesque, 17109-35), 100 mM citrate (pH 4, 4.5, 5, 5.5, 6, 6.5, and 7; sodium citrate tribasic dehydrate, Sigma-Aldrich, S4641), PBS (pH 7.5 and 8), 10 mM borate (pH 8.5, 9, 9.5, and 10; borate reference solution, Horiba), 50 mM NaHCO3 (pH 10.5 and 11; Nacalai Tesque, 31212-25), and 100 mM NaH2PO4 (pH 11.5; Nacalai Tesque, 31718-15). The pH of the standard solutions was adjusted with hydrochloric acid or sodium hydroxide, and measured with a benchtop pH meter (Horiba Ltd., LAQUA F-71). The predicted pH values were less accurate in the low (pH < 3) or high (pH > 12) pH range by the single linear regression model. Therefore, I introduced three regression models: an acid-range, a neutral-range, and a base-range regression model. The pH was first predicted with the neutral-range regression model. If the predicted pH was higher than 11.1, then the base-range regression model was applied. If the predicted pH was lower than 5.5, then the acid-range regression model was applied. These thresholds were statistically determined by comparing the mean square error of the predicted pH and the measured pH.

Evaluation of hyperhydrative RI matching reagent

Brain samples of 8-week-old mice were delipidated by Sca*l*eCUBIC-1 as described above. After delipidation, brain samples were washed with PBS, and then cut to make hemisphere brains. Each hemisphere brain was immersed in 10 ml of CUBIC-X1 [20% imidazole (Tokyo Chemical Industry, I0001)] at room temperature with gentle shaking for 1 day. CUBIC-X1-treated brains were subsequently subjected to 10 ml of RI media at room temperature with gentle shaking for 1 day. I used 60 wt% Histodenz^{TM} (RI = 1.467, Sigma-Aldrich, D2158) (Ke et al., 2016; Yang et al., 2014), 75 wt% fructose (RI = 1.472, Nacalai Tesque, 16315-55), 100 wt% glycerol (RI = 1.473, Nacalai Tesque, 17018-25), 75 wt% TDE (RI = 1.469, 2,2'-Thiodiethanol, Tokyo Chemical Industry, T0202) (Aoyagi et al., 2015; Costantini et al., 2015), Sca*l*eA2 [RI = 1.382, 4 M urea, 10% (w/v) glycerol, and 0.1% (w/v) Triton X-100] (Hama et al., 2011) and Sca*l*eCUBIC-2 (RI = 1.485, 50 wt% sucrose, 25 wt% urea, 10 wt% triethanolamine) (Susaki et al., 2014) in addition to imidazole/antipyrine cocktails. I measured the swelling ratio of the resulting brain samples by ChemiDocTM XRS Plus. RI values of imidazole/antipyrine cocktails were measured by an Abbe refractometer (ATAGO, DR-A1, Japan).

I captured transmission images of swollen brain samples. These samples were prepared as follows. Delipidated brain samples were immersed in 30 ml of CUBIC-X1 at room temperature

with gentle shaking for 3 days. CUBIC-X1 was refreshed every 12 hours. Then, these brains were immersed in 40 ml of each chemical cocktail at room temperature with gentle shaking for 2 days. Each reagent was daily refreshed.

Concern about Potential False Negatives

Each chemical was used as a 10%(wt/wt) solution in all of the first chemical screenings. We hoped to minimize false negatives in the first screening, so we would not miss potential candidates. Although chemicals were likely to have concentration-dependent effects on each parameter, we could avoid false negatives by taking advantage of the chemical diversity of our chemical library. That is, owing to our comprehensive chemical profiling, we could predict whether the performance of a chemical in the first screening was under-estimated or not from its chemical structure.

We also considered the possibility of chemicals with more dramatic concentration-dependent behavior. Concentration-dependent self-aggregation of the solute is one of the most likely causes of dramatic concentration-dependent behavior. In aqueous medium, hydrophobic chemicals precipitate and amphiphilic chemicals form micelles in a concentration-dependent manner. Since precipitates would have no effect on tissue clearing, we focused on the ability of amphiphilic chemicals such as detergents to form water-soluble micelles. To avoid false negatives in the amphiphilic chemicals, we prepared a wide variety of detergents. We categorized a series of detergents according to the polarity head group, because each group of detergents forms micelles with similar chemical properties at concentrations above the critical micelle concentration (CMC). In general, the CMC of a detergent tends to decrease as the hydrophobic part of the detergent molecule grows. **Figure 4B** indicates that the micelle state exhibited much higher delipidation activity than the monomer state. This means that amphiphilic chemicals with a high CMC were potential false negatives in our delipidation screening. That is, the delipidation efficiency of these chemicals in vitro may be much higher at concentrations above the CMC. However, micelle molecules are liable to have low permeability in real tissue as described above, and higher solute concentrations often have a quenching effect on fluorescent proteins. Thus, we did not perform additional experiments on the concentration dependence of such amphiphilic chemicals. In the decoloring screen, micelle molecules had a similar tendency for low permeability as in real tissue. For the RI matching

and decalcification assays, we did not observe significant positive outputs for amphiphilic chemicals.

Taken together, our chemical profiling approach applies chemical insights and hypotheses to tissue clearing, and these insights are helpful for preventing potential false-negatives. Of course, our profiling is not perfect for false-negative detection due to unknown chemical phenomena. Nevertheless, we are confident that our screening system has sufficient detection sensitivity without redundancy and complexity to be useful for this field at the present time.

Comparison of Organic Solvents and Hydrophilic Chemicals

To examine the effects of organic solvents and hydrophilic chemicals, I included several organic solvents in this study, such as tetrahydrofuran (THF, CU#1427), dimethyl sulfoxide (DMSO, CU#1510), 2-propanol (CU#1514), methanol (CU#1515), ethanol (CU#1516), benzyl alcohol (CU#1517), benzyl benzoate (CU#1518), acetone (CU#1520), 1,4-dioxane (CU#1521), acetonitrile (CU#1522), ethyl acetate (CU#1523), and N,N-dimethylformamide (DMF, CU#1524). However, I could not perform a comprehensive evaluation of organic solvents due to experimental feasibility. First, almost all organic solvents (e.g., dichloromethane and diphenyl ether), with the exception of several alcohols and aprotic polar solvents, as listed, are immiscible with water. Second, plastic experimental tools (e.g., microtubes and microplates) are highly labile to many organic solvents (especially at high concentration). Therefore, I included only the above-listed organic solvents in this study. In our chemical screening, I prepared 10%(wt/wt) aqueous mixtures of the organic solvents because of the above concerns and to make fair comparisons. However, these aqueous mixtures displayed quite low performances; thus, organic solvents would exert their clearing performance at a high concentration or in a fully dehydrated condition.

Chemical Parameters

To obtain a chemical profile for the chemicals identified from the screens, we analyzed a series of chemical parameters (e.g., LogP and PSA) using the ChemOffice software. The LogP and LogS value of each chemical was calculated by the MOSES descriptor Community edition (http://www.molecular-networks.com/services/mosesdescriptors). Solubility parameters (e.g., dD and dP) of each chemical were calculated based on the Hansen solubility parameters

(Hansen, 2007). The stability constant of various chemicals for Ca2+ ion according to the NIST Standard Reference Database 46 was used (Smith et al., 2003).

Multivariate Linear Regression Analysis

We prepared a series of parameters consisting of three classes of parameters: functional parameters, solubility parameters (calculated by Hansen solubility parameters), and structural and topological parameters. After normalizing the scores and parameters, I performed partial least squares (PLS) regression using four major PLS components. The variable importance in projection (VIP) scores of two major PLS components were calculated from the results.

CUBIC Protocols

CUBIC Protocol I for Adult Mouse Organ Samples and Marmoset Brain

For the efficient clearing of mouse organs, I first performed an optional transcardiac perfusion of CUBIC-P reagents. After the mouse was sacrificed by an overdose of pentobarbital, 15 ml of PBS was perfused followed by 20 ml of 4% PFA-PBS. After another 15 ml of PBS was perfused, the transcardiac perfusion of 100 ml of CUBIC-P [mixture of 5 wt% 1-methylimidazole (Tokyo Chemical Industry, M0508), 10 wt% CU#0414 (N-Butyldiethanolamine, Tokyo Chemical Industry, B0725) and 5 wt% Triton X-100 (Nacalai Tesque, 12967-45)] from the left ventricle for 10 minutes was performed. After perfusion, the organs were dissected and directly immersed in CUBIC-L (mixture of 10 wt% CU#0414 and 10 wt% Triton X-100). The organs in CUBIC-L were incubated with shaking at 37℃ for 3-7 days. The immersion period was based on the sample size. If the immersion period was longer than 4 days, the CUBIC-L was refreshed at least once. After delipidation, the organs were washed in PBS with gentle shaking at room temperature overnight. If required, the organs were stained with RedDotTM2 (1:100, Biotium Inc, #40061) or propidium iodide (10 μg/ml, PI; Life Technologies, P21493) in 0.1 M phosphate buffer (PB) containing 0.5 M NaCl with shaking at room temperature for 3-5 days. The organs were then immersed in 1:1 water-diluted CUBIC-RA [recommended for FP-expressing organs, a mixture of 45 wt% CU#0640 (antipyrine, Tokyo Chemical Industry, D1876) and 30 wt% CU#1283 (N-methylnicotinamide, Tokyo Chemical Industry, M0374)] or in 1:1 water-diluted CUBIC-R [for other organs, mixture of 45 wt% CU#0640 and 30 wt% CU#0855 (nicotinamide, Tokyo Chemical Industry, N0078)] with

gentle shaking at room temperature for 1 day. The organs were then immersed in CUBIC-RA or CUBIC-R with gentle shaking at room temperature for 1-2 days. The pH of CUBIC-R and CUBIC-RA can be optionally adjusted to approximately 8-9 with CU#0414. If required, the cleared organs were embedded in CUBIC-agarose gel [2% agarose (Nacalai Tesque, 01163-76) dissolved in CUBIC-RA or CUBIC-R].

The clearing and staining of adult marmoset brain was performed as follows. The marmoset was sacrificed by an overdose of pentobarbital (> 100 mg/kg, Nacalai Tesque, 02095-04), then transcardially perfused with 200 ml of cold PBS (pH 7.4) and 300 ml of 4% PFA-PBS. The brain was dissected, then post-fixed with 4% PFA-PBS at 4 ℃ overnight. After washing in PBS, the brain was immersed in CUBIC-L with shaking at 37 ℃ for a total of 5 weeks, and then at 45 ℃ for 1 week. The CUBIC-L was refreshed every 1-2 days throughout the delipidation. After washing in PBS, the brain was immersed in 10 μg/ml propidium iodide (PI) in PB containing 1.5 M NaCl with shaking at 37 ℃ for a total of 19 days. The staining solution was refreshed after day 12. After washing in PBS, the brain was immersed in 10 wt% imidazole (Tokyo Chemical Industry, I0001) aqueous solution with gentle shaking at room temperature for 3 days. The imidazole solution was refreshed every day. The brain was then immersed in 1:1 water-diluted CUBIC-R (pH adjusted to approximately 8-9 with CU#0414) with gentle shaking at room temperature for 3-4 days. Finally, the brain was immersed in CUBIC-R (pH adjusted to approximately 8-9 with CU#0414) with gentle shaking at room temperature for 7 days. The CUBIC-R was refreshed after day 4.

CUBIC Protocol II for Mouse Body or Tissues That Include Bone

PFA-fixed samples were immersed in CUBIC-L with shaking at 37 ℃ for 3-7 days, then washed with PBS at room temperature overnight. The immersion period was based on the sample size. If the immersion period was longer than 4 days, the CUBIC-L was refreshed at least once. The samples were immersed in CUBIC-B [10 wt% EDTA (Nacalai Tesque, 15105-35) and 15 wt% imidazole] with shaking at 37 ℃ for 5-7 days, then washed with PBS at room temperature overnight. During decalcification, the CUBIC-B was refreshed at least once. The samples were immersed in CUBIC-L with shaking at 37 ℃ for 2-4 days, then washed with PBS at room temperature overnight. If required, the organs were stained with 10 μg/ml PI in 0.1 M PB containing 0.5 M NaCl with shaking at 37 ℃ for 5-7 days. The samples were immersed in 1:1 diluted CUBIC-RA or CUBIC-R with gentle shaking at room temperature for 1 day. The

samples were then immersed in CUBIC-RA or CUBIC-R with gentle shaking at room temperature for 1-2 days. If required, the cleared samples were embedded in CUBIC-agarose gel.

CUBIC Protocol III for Aggressive Tissue Clearing

Human tissues were stored in formalin at 4 ℃ until use. The dissected blocks were washed with PBS overnight prior to clearing. The tissue blocks were immersed in CUBIC-HL [mixture of 10 wt% CU#0070 (1,3-bis(aminomethyl)cyclohexane, Tokyo Chemical Industry, B1005) and 10 wt% CU#0631 (sodium dodecylbenzenesulfonate, Tokyo Chemical Industry, D0990), whose pH was adjusted to 12.0 by p-toluenesulfonic acid (Tokyo Chemical Industry, T0267)] with shaking at 37 ℃ (for human brain or kidney) or 45 ℃ (for human heart, liver, lung, or spleen) for 1-2 weeks, then washed with PBS at room temperature. The immersion period was based on the sample size. Since the apparent opacity inside the sample gradually disappears as delipidation progresses, the delipidation period could be easily judged by the appearance of the sample soaked in CUBIC-HL. Note that prolonged delipidation may damage the sample morphology. If delipidation needs to be prolonged beyond 2 weeks, we recommend that the subsequent delipidation be done at a lower temperature or in CUBIC-L. During delipidation, the CUBIC-HL should be refreshed at least once. If required, the organs were stained with 10 μg/ml PI in 0.1 M PB containing 0.5 M NaCl with shaking at 37°C for 5-7 days. After washing in PBS, the samples were immersed in 1:1 diluted CUBIC-R with gentle shaking at room temperature for 1 day. The samples were then immersed in CUBIC-R with gentle shaking at room temperature for 1-2 days. If required, the cleared organs were embedded in CUBIC-agarose gel.

CUBIC Protocol IV for Large Blocks of Human Brain Tissue

Human brain blocks were stored in phosphate-buffered formalin at 4 ℃ until use. The dissected blocks (around 1 cm^3) were washed with PBS overnight prior to clearing. The brain blocks were immersed in CUBIC-L with shaking at 45 ℃ for 1-2 weeks, then washed with PBS at room temperature. The immersion period was based on the volume of white matter. During delipidation, the CUBIC-L was refreshed at least once. After washing in PBS, the samples were immersed in 1:1 diluted CUBIC-R with gentle shaking at room temperature for 1 day. The

samples were then immersed in CUBIC-R with gentle shaking at room temperature for 1-2 days. We noted that the autofluorescence of cerebral cells decreased as the delipidation period increased. We recommend that delipidation be finished by approximately one week to preserve sufficient autofluorescent signals. If required, the cleared samples were embedded in CUBIC-agarose gel.

CUBIC-X protocol

Delipidation of brain samples for CUBIC-X was performed as following. For Thy1-YHP-H, PLP- YFP, Mlc1-YFP mice brain, a modified Sca*l*eCUBIC-1 reagent [5 wt% N,N,N',N'-tetrakis(2-hydroxypropyl)ethylenediamine (Quadrol, Tokyo Chemical Industry, T0781), 25 wt% urea (Nacalai Tesque, 35904-45), and 15 wt% Triton X-100 (Nacalai Tesque, 12967-45)] was applied to suppress quenching of fluorescent proteins. For other brains, Sca*l*eCUBIC-1 reagent (25 wt% Quadrol, 25 wt% urea, 15 wt% Triton X-100) was applied (Susaki et al., 2014). Brain samples were initially immersed in 1/2-water-diluted delipidation reagent at 37 ℃ with gentle shaking for 3 hours. Then, brain samples of Thy1-YHP-H, PLP- YFP and Mlc1-YFP mice were immersed in modified Sca*l*eCUBIC-1 at 37 ℃ with gentle shaking for 8 days. Other brain samples were treated with Sca*l*eCUBIC-1 at 37 ℃ for 5-14 days. Because I noticed long term delipidation made the young (less than 3-week-old) mouse brain too soft to handle properly, I used different duration of delipidation depending on ages; 5 days for 1-week-old mice, 7 days for 3-week-old mice, 14 days for 8-week-old mice, and 14 days for 6-month-old mice. The delipidation cocktails were refreshed every 4 days. After delipidation, the brains were thoroughly washed with PBS at room temperature with gentle shaking overnight.

The brain expansion protocol is composed of four major steps including, delipidation followed by nuclear staining, swelling, RI matching, and gel embedding. Delipidation procedure was already mentioned above. For nuclear staining, I immersed a delipidated brain sample in 3 ml of 30 μg/ml propidium iodide (Life Technologies, P21493) and 1.5 M NaCl in PBS, and incubated at room temperature with gentle shaking for 3 days. The brain sample was washed with PBS at room temperature with gentle shaking for more than 12 hours. Then, I immersed the sample in 30 ml of 20% imidazole, and incubated at 4 ℃ (for Thy1-YFP-H, PLP- YFP and Mlc1-YFP brains) or at room temperature (for other brains) with gentle shaking for 2.5 days. I note that I incubated brain samples expressing fluorescent protein at the lower temperature to avoid possible quenching. Since the expanded brains were fragile, careful handling was

required for all the following procedure. Each expanded brain was immersed in 40 ml of CUBIC-X2 [5% (w/v) imidazole and 55% (w/v) antipyrine (Tokyo Chemical Industry, D1876) cocktail] with gentle shaking at room temperature for 1.5 days. The cocktail was refreshed every 12 hours. For gel embedding, highly cleared swollen brains were embedded in CUBIC-X2 including 2% agarose (Wako Pure Chemical Industries Ltd., 318-01195). Prior to gel embedding, agarose powder was dissolved in CUBIC-X2 by heating, and then I cooled down the mixture to a moderate temperature. Gelation was performed at 4℃ overnight. The gel embedded samples were appropriately dissected for the following imaging.

Measurement of light transmittance and scattering for expanded brains

I measured the light transmittance of the brain samples from 380 to 780 nm at 5 nm intervals with an integrating sphere (Spectral Haze Meter SH 7000, Nippon Denshoku Industries). I put every sample in the optical cell of 2 cm optical path length with each chemical solution. I measured the light transmittance of water, 2% agarose, CUBIC-X2, 2% agarose CUBIC-X2, and CUBIC-X brain in 2% agarose CUBIC-X2. I calculated transmission value for 1 cm long by square root of total transmission value at each wavelength.

For measurement of scattering, I referred the method described by Schwarz et al (Schwarz et al., 2015). Images were taken with macro zoom microscope (MVX10, Olympus) with SDFPLAPO1.6XPF (NA = 0.24, Olympus) objective lens. The brains were immersed in Sca*l*eA2 or CUBIC-X2 respectively in glass cases placed on top of a light source with a positive 1951 USAF chart (Edmund Optics). CUBIC-X2 treated brains were embedded in gel with 2% agarose prior to the imaging. For quantification, minimum and maximum intensity over element 2, group 2 of the chart were used. The absolute differences between the minimum and the maximum were computed, then the local contrast was calculated by normalizing it by blank controls (Sca*l*eA2 reagent or 2% agarose CUBIC-X2 in CUBIC-X2).

Evaluation of application of CUBIC-X to fluorescent protein with confocal microscopy

To evaluate quenching of fluorescent protein by various chemical treatments, purified recombinant EGFP, EYFP and mCherry were used. Each chemical solution was mixed with EGFP (6.7 μg/ml, final concentration), EYFP (8.5 μg/ml, final concentration), or mCherry (200 μg/ml, final concentration). I measured the fluorescence intensity of each sample with Enspire

(Perkin Elmer, USA). To evaluate availability of CUBIC-X protocol to brain samples expressing fluorescent reporter proteins, I acquired image of hippocampal area of Thy1-YFP-H mouse brain from ventral side at 2 μm step by an upright confocal microscope (FV1200, Olympus) equipped with 25× objective lens (XLSLPLN25XGMP, NA = 1.0, WD = 8.0 mm, Olympus). 473 nm laser was used for excitation.

Deformation Analysis of Cleared Brains

Brains after PBS, CUBIC protocol I without pH adjustment, and CUBIC protocol I with pH adjustment to 8-9 were subjected to deformation analysis. Two brains were prepared for each procedure, and then projection images were captured by a ChemiDocTM XRS Plus (Bio-Rad). The brains were manually segmented, then registered to a standard post-fixed brain. The average of the two obtained deformation fields was visualized and mapped onto a representative projection image of the brain.

Long-term Tissue Preservation

To preserve the cleared tissue for a long time, we recommend storing it in O.C.T. compound at −80°C after washing it with PBS as described in our previous paper (Susaki et al., 2015). In this storage medium, FP signals can be preserved for several months to years.

Immunostaining

For **Figure 14D**, an 8-week-old ICR mouse brain was washed with PBS after 4 days of delipidation with CUBIC-HL. The brain was immersed in 40% sucrose for 1 day, embedded in O.C.T. compound (Sakura Finetek), and sectioned with a cryostat (CM3050S, Leica). The brain sections were immersed in 200 μl of PBST with 1% anti-GFAP-Cy3 (C9205, Sigma-Aldrich) or 0.1% anti-NeuN (MAB377, Millipore) antibodies. For NeuN detection, a secondary antibody (A21203, Thermo Fisher Scientific) was applied. For **Figure 14F**, the human brain was washed with PBS overnight and sliced after 9 days of delipidation with CUBIC-L (CUBIC protocol IV). The slice was placed into 400 μl of immunostaining buffer (mixture of PBS, 0.5% Triton X-100, 0.25% casein, and 0.01% NaN3) containing 1:20 diluted rhodamine-conjugated lectin (RL-1062, Vector Laboratories) or 1:10 diluted Alexa647-conjugated α-SMA (alpha smooth

muscle actin) antibody (IC1420R, Novus Biologicals) for 5 days at room temperature with gentle shaking. For the control experiment, the immunostaining buffer without antibody was applied. After washing the samples with PBS for several hours, the samples were immersed into CUBIC-R according to CUBIC protocol IV.

Microscopy

Light-sheet Fluorescence Microscopy (LSFM)

Macroscopic whole-body or organ images were acquired with two custom-built LSF microscopes (MVX10-LS, developed by Olympus). Images were captured using a 0.63× objective lens [numerical aperture (NA) = 0.15, working distance = 87 mm] with digital zoom from 1× to 6.3×. The first LSF microscope was equipped with lasers emitting at 488 nm, 532 nm, 590 nm, and 639 nm. The second was equipped with lasers emitting at 488 nm, 532 nm, 594 nm, and 637 nm. When the stage was moved to the axial direction, the detection objective lens was synchronically moved to the axial direction to avoid defocusing. The RI-matched sample was immersed in an oil mixture (RI = 1.525) composed of silicon oil HIVAC-F4 (RI = 1.555, Shin-Etsu Chemical Co., Ltd.) and mineral oil (RI = 1.467, M8410, Sigma-Aldrich) during image acquisition.

A customized light-sheet microscope was used for the high-resolution-imaging of the organs of adult mice. Fluorescence excited by a 488 nm CW laser (Omicron, SOLE-3) was captured with a sCMOS censor (Andor, Neo) using a 10× objective lens (XLPLN10XSVMP, NA = 0.6, working distance = 8 mm, Olympus). The details of the light-sheet microscope are described in materials and methods for Results 2. To obtain complete views, the regions of interest were divided into 7 × 4 tiles (for the left medial lobe of the mouse liver), or 6 × 8 tiles (for the left lung of the mouse). Images were collected by scanning the sample in the z-direction, with a step size of 5 μm.

Confocal Microscopy

An upright confocal microscope (FV1200, Olympus) was used for microscopic 3D imaging. The microscope was equipped with a 25× objective lens (XLSLPLN25XGMP, NA = 1.0, WD = 8.0 mm, Olympus). A 473 nm laser was used for image acquisition. During image acquisition, RI-matched samples were immersed in a mixture of silicon oil (RI = 1.525) as described above.

In Vivo Bioluminescence Imaging

Mice were anesthetized with avertin, and D-luciferin potassium salt (Promega) was injected intraperitoneally. Ten to fifteen minutes after injection, the luciferase activity was measured using a NightOWL II LB983 (Berthold Technologies GmbH & Co. KG, Bad Wildbad, Germany).

Histological Examination

After CUBIC-based clearing, biological samples were washed with PBS, embedded in paraffin, and subjected to HE staining as previously described (Hoshino et al., 2015) and to a series of immunostainings.

Image Analysis

The Analysis of Cellular Nuclei

The cellular nuclei in organs were comprehensively detected by our image-processing pipeline (**Figure 29**). The process can be divided into two steps: 2D detection of cells and 3D unification of multiply detected cells. The 2D detection of cells was performed by detecting local maxima after applying a mean filter to raw images. Then, 3D local maxima were detected after a 3D mean filter was applied to the 2D-detected cells. The detected cellular nuclei ("points" or "point clouds") were further analyzed for the segmentation of tubular structures. To this end, I used the alpha shape function with the specific alpha radius by using MATLAB. The alpha radius was set at 30 μm for liver and 50 μm for lung. After forming the alpha shape, the surface points composing the alpha shape were used. Since the surface points also included cells located in the outer layer of the organ, I removed those points by applying a manually generated mask.

Multi-directional Image Fusion

Multi-directional image fusion was performed after the acquisition of images from multiple directions unless noted. All the samples were embedded in agarose, and mounted in the LSF microscope. I first performed the imaging with both optical arms of the LSF microscope (i.e.,

left and right) from one direction (top-to-bottom). The samples were then flipped 180° manually, followed by image acquisition (bottom-to-top) with both optical arms. The imaging sequences were then repeated for multi-color imaging. These processes produced four stacks per channel: a right-side-illuminated top-bottom stack (TB-R), left-side-illuminated top-bottom stack (TB-L), right-side-illuminated bottom-top stack (BT-R), and left-side-illuminated bottom-top stack (BT-L). For the registration process, I set the TB-L stack as the fixed images, then three other stacks were registered to TB-L stack. Prior to registration, the stacks were reduced to less than 4 GB by cropping marginal regions, or by downsampling them into isotropic voxel sizes to reduce the computational cost. Then, TB-R and BT-L were directly registered onto TB-L with an affine transformation using ANTs (Avants et al., 2011). Because the direct registration of BT-R to TB-L often ends in misalignment due to the intensity gaps of these two stacks, I performed indirect registration by registering BT-R onto BT-L, followed by the application of the affine matrix obtained from the registration of BT-L onto TB-L. These mutually registered images were fused using the Fiji software, Multiview Reconstruction (Schindelin et al., 2012).

Segmentation

For segmentation of the mouse kidney glomeruli, I used HLoG (Hessian based Difference of Gaussian) developed by Zhang et al. (Zhang et al., 2015) with minor modifications. In the original paper, renal glomeruli were extracted by unsupervised clustering. Because this method was originally optimized for MRI-scanned images and therefore could not show high accuracy, I introduced a manual threshold for the smallest eigenvalue to achieve higher accuracy. For the segmentations of metastatic cancer, the thresholds were applied based on absolute intensity. Manual segmentation was performed to segment the human kidney glomeruli.

Virtual Multiplex Fluorescence Imaging and Analysis of Whole Brain

Fluorescently labeled mouse brains were stained with a far-red nuclear stain, RedDotTM2, prior to the RI-matching process. The cleared brains were embedded in agarose gel as mentioned above. Brain images were captured using a 0.63× objective lens with a 1.25× zoom. The brain structures were visualized by the RedDotTM2 fluorescent signal at 637-nm excitation. The sectional images were taken at 7.5-μm steps from both the right and left sides with a fixed focal

position of the light sheet. The FP signal was then visualized using a laser of appropriate wavelength with sequential shifting of the focal position of the light sheet. The thinnest focal point of the LSF microscope was horizontally scanned 6 times per plane to reduce defocus derived from the Gaussian shape of the beam. The scanning with focus shifts was performed from both sides of the illumination arm as described previously (Gao, 2015; Santi et al., 2009).

The images of the identical horizontal positions (2 images for RedDotTM2 signal, or 12 images for FP signals) were fused using the content-based fusion algorithm proposed by Preibisch et al. (Preibisch et al., 2009). To register individual brains, the fused volumetric nucleus images were downsampled 5:1 in one direction. These downsampled images were registered using the ANTs software in the symmetric normalization (SyN) manner. The obtained transformation information was applied to the original volumetric FP images, thus achieving registration without losing the resolution. To apply the transformation information to large data, I used our customized MATLAB code, because direct application of the transformation with the default algorithm in ANTs requires a huge amount of memory, which makes it practically impossible. The overall process (fusion, registration, application of transformation information) was fully automated.

Volume Rendering and Image Visualization

To generate the tubular structures, visual mapping of the alpha shape was implemented by MATLAB. For other volume rendered images, Imaris software (version 8.1.2, Bitplane) was used. The section images were generated by Imaris or Fiji software.

Protein Quantification

Human brain tissue was weighed and then immersed in PBS, Sca*l*eCUBIC-1, CUBIC-L, or CUBIC-HL. After 4 days of delipidation at 45 ℃ with gentle shaking, the brain samples were washed with PBS at room temperature for half a day with gentle shaking. The washed samples were then subjected to protein quantification. To quantify the residual protein content, the samples were thoroughly crushed, then sonicated in 1% Triton X-100 in PBS to obtain a homogenized suspension. After adjusting for the total weight of each sample, the protein was quantified with the Microplate BCATM Protein Assay Kit-Reducing Agent Compatible (Thermo Fisher Scientific, #23252) according to the instruction manual, with OD570. The

absolute amount of protein was determined by fitting the OD570 value to a standard curve generated by a serially diluted pure Albumin standard.

Quantification of Image Quality

I used discrete cosine transformation Shannon entropy (DCTS) (Royer et al., 2016) to quantify the image quality. The DCTS calculation was performed for every plane image in **Figure 18B**, and for every 10 plane images in **Figure 18H** and **18I**.

METHOD DETAILS FOR RESULTS 2

Evaluation of distortion during a CUBIC-X protocol

To assess non-linear deformation of chemically treated brains, I attempted to prepare a transparent brain preserving original shape as a standard. After delipidation and PI staining, brains were washed with 30 ml of PBS at room temperature with gentle shaking for 12 hours, and then immersed in 10 ml of 1/2-diluted modified Sca*l*eCUBIC-2 [22.5 wt% antipyrine, 22.5 wt% sucrose, 25 wt% urea, 10 wt% triethanolamine (Wako Pure Chemical Industries Ltd., 145-05605), and 80 mM NaCl] at 37 ℃ with gentle shaking overnight. Then, the brains were further immersed with 5 ml of modified Sca*l*eCUBIC-2 at 37 ℃ with gentle shaking for 2 days. The modified Sca*l*eCUBIC-2 was refreshed every day. After image acquisition, the brains were washed with 30 ml of PBS at room temperature with gentle shaking overnight, and then immersed in 30 ml of Sca*l*eCUBIC-1 at 37 ℃ with gentle shaking for 1 day. After PBS washing, the samples were subjected to expansion with CUBIC-X1, followed by RI matching with CUBIC-X2 and gel embedding as described above.

To acquire images, I used a light-sheet fluorescent microscope (developed by Olympus). The before-CUBIC-X brain sample was immersed in oil mixture (RI = 1.490) of silicon oil TSF4300 (Momentive Performance Materials, RI = 1.498) and mineral oil (Sigma-Aldrich, RI = 1.467), and the after-CUBIC-X brain sample was in mineral oil (Sigma-Aldrich, RI = 1.467) during image acquisition. Images were captured with 0.63 × objective lens (NA = 0.15, WD = 87 mm) with 2 × optical zoom for before-CUBIC-X brain or 1 × zoom for after-CUBIC-X brain. 532 nm laser was used for image acquisition. To cover whole-brain, a stage was designed to move both in the lateral direction and the axial direction. When the stage was moved to the axial direction,

the detection objective lens was synchronically moved to the axial direction to avoid defocusing.

I measured the volume of before- and after-CUBIC-X brains by segmenting the brains from acquired images. The segmentations were performed by combining the binarization and morphological opening of the images. The thresholds for the binarization and the radius of morphological openings were manually determined. The voxel numbers of segmented brain volumes were counted, then converted into mm^3.

For non-linear distortion analysis, post-expansion images were registered to pre-expansion images using affine transformation, and then non-linear transformation. I used ANTs (Advanced Normalization Tools) (Avants et al., 2011) as a registration tool because it has been proved successful in a number of image registration tasks (Murphy et al., 2011). Affine transformation was performed with mutual information, 64 bins and 300000 samples as the parameters of the ANTS function. I used $100 \times 10 \times 10$ iterations for non-linear transformation. For non-linear transformation, I used symmetric normalization (SyN) implemented in ANTs. I used the value in "*InverseWarp.nii.gz" deformation field file to evaluate non-linear deformation because this file contained non-linear transformation element of registration. To reduce the computational cost, I applied the images to a 3D grid with 20 voxel spacing, and then collected the voxels in the grid. I calculated two values of L' and L from all pairs of the collected voxels, where L' is the distance between two voxels before-SyN transformed images and L is the distance between two voxels from after-SyN transformed images. Both of L' and L were measured in the scale of the before-SyN transformed image. I created the graphs of $|L - L'|$ as a function of distance L with calculating root mean square error and standard deviation. RMS errors were less than ~20 μm, which is ~0.8% of the measurement length (2,500 μm) in the investigated regions.

Evaluation of cellular loss during a CUBIC-X protocol

I confirmed that none of the nuclei were lost during delipidation process. To visualize the nuclei before delipidation process, I used brains of R26-H2B-EGFP mice. The brains were sectioned into 1 mm-thick coronal slices, then immersed in modified Sca*l*eCUBIC-2 prior to the delipidation process. The fluorescence observation of nuclei was performed with confocal microscopy. Delipidation process with modified Sca*l*eCUBIC-1 was performed after

observation, and samples were gently shaken at 37 ℃. The samples were cleared with modified Sca*l*eCUBIC-2 one hour before the confocal imaging, and delipidated again until the end of the sequential observation. Because repeated observation with confocal microscopy bleaches EGFP signal, propidium iodide was introduced to enhance the signal of nuclei at day 3.

I also confirmed that none of the nuclei were lost during expansion by comparing the images before and after the CUBIC-X treatment. "Before-CUBIC-X" brain was prepared by the delipidation and nuclear staining protocols and imaged by a confocal microscope. Then, the same sample was expanded ("After-CUBIC-X" brain) and imaged by customized LSFM. "after-CUBIC-X" brain was linearly registered to images of "before-CUBIC-X" brain by ANTs using affine transformation. To evaluate how intercellular expansion ratio depends on cell density, images of "after-CUBIC-X" were first registered to images of "before-CUBIC-X" brain by similarity transformation. Then, one pair of 2D images (250 μm × 250 μm) were extracted. The nuclei in the images were segmented by thresholding and converted to circular particles with "Analyze Particles" function in Fiji. 1D-cell density was measured as the number of nuclei on connecting line divided by the connecting line length. Intercellular expansion ratio was measured as L2/L1 for matched pair of the nuclei. Finally, the relationship between intercellular expansion ratio and 1D-cell density was plotted.

Construction of a customized light-sheet fluorescent microscope

Overviews of the customized light sheet microscope are illustrated in **Figure 25**. For the notation of xyz coordinate system, please refer to **Figure 24C** and **24D**. Excitation light source was provided by a fiber-coupled CW laser (Omicron, SOLE-3 equipped with λ = 488, 594, and 642 nm). After collimation, the beam was split into two paths (right and left excitation) using 50:50 beam splitter (Thorlabs). Left and right paths were essentially identical. It is then followed by an electrically tunable lens (ETL, Optotune, EL-10-30) combined with offset lens with f = -50 mm, which was positioned at the conjugated plane with the back focal plane of the illumination objective through a series of 4f relay lenses. The focal length of the ETL was tuned to adjust the focus point of the light sheet. A graduated iris was placed to adjust the diameter of the beam which defined the effective NA of the illumination objective (NA = 0.1, WD = 30 mm, Nikon, CFI Plan 4X). The diameter of the iris was chosen to be 3 mm, which corresponded to effective NA of 0.03. NA = 0.03 corresponds to the minimum beam waist of about 10 μm and Rayleigh length of about 0.64 mm, which ensured the homogeneous light sheet thickness

throughout the field of view (in this setup, 1.4 mm in the x-direction). The first galvo mirror (Thorlabs, GVS001) was placed to adjust the z position of the light sheet so that excitation beam illuminates the focal plane of the detection objective. The second galvo mirror (Cambridge Technology, VM500Plus) was used to generate light sheet, following the scheme of DLSM (Keller et al., 2008). The mirror was swept at 500 Hz and the amplitude was adjusted to sufficiently cover the entire field of view (in this setup, 1.65 mm in the y-direction). The detection objective (XLPLN10XSVMP, NA = 0.6, working distance = 8 mm, Olympus) was inserted directly into the hole located on the side of the custom-made sample chamber, and the chamber was filled with mixture of high RI silicon oil (RI = 1.498, Momentive Performance Materials, TSF4300) and low RI silicon oil (RI = 1.396, Momentive Performance Materials, TSF405) whose RI was adjusted to match to the brain samples (RI = 1.467). The samples were mounted on a motorized xyzθ stage through a custom-made sample holder (x and y stage, Thorlabs, MTS50/M-Z8E; z stage, Physik Instrumente, M-112.1DG; θ stage, Physik Instrumente, M-116.DG). The gel-embedded brain sample was mounted onto the sample holder. The fluorescence of the sample was imaged with an sCMOS camera (Andor, Neo 5.5) through an f = 200 mm tube lens, after passing through a custom-made filter wheel equipped with φ = 1 inch filters. Since the detection objective had a large back pupil, use of 1 inch filters was necessary to prevent the clipping of the collected photon. All electronic devices were integrated and controlled by a home-built program written using LabVIEW (National Instruments).

Tiling sequence in whole-brain imaging

In order to image the entire brain with a limited field of view and a working distance of the detection objective, I designed the following image acquisition sequence. Schematic of the procedures is illustrated in **Figure 24D**. Initially, xy coordinates of the imaging region were defined by specifying the top-left and right-bottom corner. The program then automatically divided the region into two-dimensional tiles, consisting of rectangular blocks whose size was determined by the field of view of the objective (in this setup, x = 1.4 mm and y = 1.65 mm) and the specified overlap value (10% for data shown in **Figure 26B** and **26C**, and 2% for others). Overlap value was defined to ensure that there would not be any loss of brain region, and overlap was considered and handled properly in the data analysis. Next, the range of z-scan was specified. Images were collected by scanning the sample in the z-direction, with a step size

of 5 μm. I also implemented an auto-focus function, which was executed every 200 images, to compensate the slight shift of the focal plane of the detection objective due to the movement of the sample. This shift was considered to be caused by the fact that there was a slight mismatch of the RI between brain sample and immersion oil, and depending on the distance between the sample boundary and objective the light traveled slightly different paths. Auto-focus routine swept several different light sheet positions by adjusting the sheet positioning galvo mirror and calculated the image sharpness by applying Sobel filter and taking the squared sum of the intensity, to find the sheet position with maximum sharpness. After collection of the images from the ventral side, the sample was rotated by 180 degrees using the θ stage, and the second half of the acquisition (dorsal side) was initiated. Since the sample was rotated along the y-axis, it was critical to determine the center of rotation in xz-plane. This was done manually by locating the identical cells or structures near the cerebral aqueduct from $\theta = 0°$ and $\theta = 180°$ sides. In this way, two blocks of images were merged continuously. The errors caused by the rotation as well as the xy-tiling, were quantified, as described below. The excitation laser power was typically 1 mW (measured before the illumination objective), which was low enough to prevent the fluorescence bleaching despite a long imaging time. For a single image acquisition, it took approximately 200 msec (50 msec of exposure, 150 msec of stage motion), achieving an acquisition rate of 5 images/sec. Each image was approximately 11 MB (2160 × 2560 pixels, 16 bit), corresponding to 55 MB/sec of data rate, which can easily be handled with hard disk drive arrays. The total image acquisition was completed within 4 days, yielding approximately 1.3 million images or 14 TB of data. The acquired data was either recorded on local hard disk drives or directly transferred to the storage in the server through 10 Gigabit Ethernet cable.

Imaging of whole mice brains expressing fluorescent proteins at subcellular resolution

To demonstrate subcellular-resolution imaging in a whole-brain scale, I imaged mice brains expressing fluorescent proteins; PLP-YFP and Thy1-YFP-H. Prior to the imaging, these brains were delipidated, PI-stained, expanded and gel embedded as described above, and imaged with the customized LSFM. To further analyze the PLP- YFP mouse brain image, we applied Frangi filter (Frangi et al., 1998) to enhance the fibrous structure. In Frangi filter, a 3D Hessian matrix is constructed at each voxel, and the fiber-ness and the fiber orientation were determined by solving the eigenvalue and eigenvector of the matrix. Prior to the filtering, image tiles were stitched together using TeraStitcher (Bria and Iannello, 2012) to correct the stripes at the tile

boundaries, and the image resolution was reduced down to 5 μm in all axes to ensure the homogeneous resolution. The Frangi filter was implemented by the MATLAB code available online (https://jp.mathworks.com/matlabcentral/fileexchange/24409-hessian-based-frangi-vesselness-filter).

Quantitative measurement of tiling displacements

I used 10 × 10 (x × y) tiles of 600 image stack with the 10% overlap of each stack both in the x- and y-direction to quantitatively evaluate the possible loss of cell detection originated from tile displacement. I selected 10 × 10 tiles so that pictures do not include space of outside of the brain. The brain samples of 1-week-old mice were used for image acquisition. Displacement was calculated with stitching software, TeraStitcher (Bria and Iannello, 2012). In alignment step, it is important to set displacement search regions. I set sV, sH, and sD, whose searching areas are 50 pixels around 200 slice images per layer. Because larger searching regions return more correct value, I set the largest values of sV, sH and sD in the computational setup. In thresholding step, I set 0.5 as a threshold parameter to judge whether the tile is stitchable or not. In placing step, displacement values were calculated by the minimum spanning tree algorithm. The resulting values in xml_merging.xml file were analyzed. The displacement values were extracted both from SOUTH_displacement and EAST_displacement. I repeated the displacement evaluation twice.

To estimate theta tile displacement, I acquired 10 × 10 (x × y) tiles of 600 image stack from θ = 0° and θ = 180° using an identical brain, and then compared. Prior to analysis, these data sets were stitched with TeraStitcher using the same parameter described above. Stitched images were further downsampled so that voxel size would be 45 μm × 45 μm × 45 μm (x × y × z), and images from θ = 180° were registered to θ = 0° images with ANTs similarity transformation. Mutual information with 64 bins was used as the similarity metrics. The resulting matrix was decomposed to estimate the rotation angle around x, y and z-axes.

A computational system and its data storage

The image processing server comprises two 12-core CPUs (Intel Corporation, Xeon E5-2590 v3), Intel C612 Chipset, 256 GB (16 GB × 16 GB) DDR4-2133 SDRAM (Samsung, M393A2G40DB0-CPB, ECC Reg.), four GPUs (Nvidia Corporation, GeForce GTX TITAN

X), a 12 GB/sec SAS RAID card (Avago, MegaRAID SAS 9380-8e) with forty-two hard disks (Seagate, ST100NM0033 and ST5000NM0084), two 1 TB SATA hard disks combined in a RAID-1 for the system, and forty 5 TB SATA hard disks combined in a RAID-0 every ten hard disks for the data. The image processing server is connected to the workstation beside the microscope by a 10 Gigabit Ethernet fiber (Mellanox Technologies, MC3309130-002) via two 10 GbE switches. The storage server comprises a CPU (Intel Corporation, Xeon E5-1620 v3), C612 Chipset (Intel Corporation), 8 GB DDR4-2133 SDRAM (Samsung, M393A1G40DB0-CPB, ECC Reg.), and a RAID controller (Avago, MegaRAID SAS 9361-8i) with thirty-six 6 TB SATA hard disks (HGST, Inc., HUS726060ALE610). One hard disk is a hot spare and other thirty-five hard disks are combined in a RAID-6. Effective capacity of these hard disks is 198 TB (1 TB for the system and about 197 TB for the data).

Algorithms for detection of cells in entire brains

The cell detection was performed by my image processing pipeline. The pipeline was implemented with MATLAB for GPU-based 2D cell detection and python for CPU-based unification of detected cells to remove duplicated detections in z-direction. The local thresholds of the sub-regions were initially determined as follows. Each sub-region (216 pixels × 256 pixels) was determined by dividing single image (2160 pixels × 2560 pixels) into 10 × 10 (x × y) regions. Modes were calculated by the histogram of pixel intensity with the bin size of 10.

Then, I determined the intensity less than 2 × mode as background intensity, and then extracted background signals. Next, I calculated mean intensity and SD from the resulting histogram, and then determined the intensity less than 2 SD above the mean intensity as an image threshold. I determined the range of thresholds both to avoid cell detection in empty regions of the images and to ensure cell detection without loss in the dense regions such as cerebellum. I detected local maxima after applying 2D mean filter kernel with a diameter DM1 in the first 2D cell-detection step. I carefully determined DM1 as 8.45 μm (13 pixels) to maximize the accuracy metric of 2D detection among cerebral cortex, hippocampus, and olfactory bulb. Each intensity and xyz coordinate of detected peaks in each stack were output in csv file format. This GPU-based 2D cell detection was completed within 35 hours. Among the detected cells in the 2D cell-detection step, I excluded the “isolated” 2D cells, which were detected only in a single plane along the z-direction, in order to remove noises. Next, I unified the multiply-detected cells after applying 3D mean filter kernel with a diameter DM2 in the second 3D-cell unifying

step. The depth of 3D mean filter kernel in z-direction was fixed to 20 μm (4 pixels), and the diameter (DM2) was determined depending on the surrounding peak number (NP) in each sub-region. This is because optimal values for DM2 are relatively dependent on the density of cells. For example, 13.0 μm (20 pixels) for DM2 was the most accurate parameter value for the brain region with an intermediate cell density ($20 \leq NP < 40$) whereas 18.2 μm (28 pixels) and 10.4 μm (16 pixels) for DM2 were the more accurate for those with lower ($NP < 20$) and higher ($40 \leq NP$) cell density, respectively. Then, I introduced variable DM2 values optimized for the cell density of the region to maximize the accuracy metric. After mean filter application, the local maxima in the z-direction were detected. Accuracy metric of the fully-automated cell detection among various brain regions was evaluated by comparing the results between automatic detection and manual detection. To facilitate the evaluation of the accuracy metric, I categorized brain areas into two types; densely populated areas (DG and CBgr) and sparsely populated areas (other brain areas). For evaluation of accuracy metric of sparsely populated areas, more than 200 cells were manually detected. Accuracy metric was calculated as frequency of true positive detections divided by the sum of frequency of true positive detection and penalty value. Penalty value was calculated as the sum of frequency of false negative detection, frequency of false positive detection, and frequency of overlapped detection. In frequency of overlapped detection, I counted the number of overlapped detections (e.g. 1 for double detection, 2 for triple detection). For the densely populated areas, I took subvolume images with thinner light sheet. The usual low-illumination-NA condition was FWHM = 11.0 μm (measured) with scanning step size = 5 μm while the high-illumination-NA condition was FWHM = 5.2 μm (measured) with scanning step size = 2 μm. Using high-NA images, independent manual counts by two people were performed and the result was compared with the automatic counting of low-NA images. The calculation of accuracy metric was the same as described above.

To compare the two-step cell-detection algorithm and direct 3D cell-detection algorithm (Shimada et al., 2005), I evaluated the computation time and cell-detection accuracy metric using the three image stacks from striatum, thalamus, and cerebral cortex layer 5/6. Each stack included 100 images. All the images were analyzed for computation time, and parts of the images were used for estimation of accuracy metric. For direct 3D cell-detection algorithm, I applied cylinder-shaped mean filter kernel with a diameter of 8.45 μm (13 pixels) and a height of 25 μm (5 pixels), and detected local maxima. For two-step algorithm, I applied circle-shaped mean filter kernel with a diameter of 8.45 μm (13 pixels), and detected local maxima in the first 2D cell-detection step. Then, I used cylinder-shaped mean filter kernel with a diameter of 8.45

μm (13 pixels) and a height of 25 μm (5 pixels) in the second 3D cell-unifying step. Ratio of computation time and accuracy metric of the cell-detection were compared.

Construction of a single-cell-resolution mouse brain atlas (CUBIC-Atlas)

The detected cells in the CUBIC-X images of C57BL/6J mice brain were annotated in the Allen Brain 25 μm reference Atlas. Prior to annotation of the detected cells, the CUBIC-X images were registered to the Allen Brain 25 μm reference atlas. From Allen Brain Atlas website, I downloaded "atlasVolume" file of CCFv2, which is a 3D assembled Nissl volume of the reference brain used for registration, and "annotation" file of CCFv2, which holds annotation ID in reconstituted brain used for annotation (http://help.brain-map.org/display/mousebrain/API). I prepared both "atlasVolume" and "annotation" in tiff format. Initially, I prepared the downsampled images of CUBIC-X brain before registration because conventional registration software is unable to handle large files. The downsampled image size was 361 × 428 × 230 (x × y × z) with the voxel size of 80.12 μm × 80.10 μm × 80.00 μm, saved as tiff format. I fitted the image file in this size by appending pixels with a signal intensity of zero. Then, the downsampled image was registered to "atlasVolume" (I term it ABA brain below) with affine transformation using ANTs software. For affine transformation, mutual information was used for the similarity metrics with the 64 bins and 300000 samples as parameters of ANTS function. The WarpImageMultiTransform command was next used in order to generate aligned image. I could not smoothly map 3D images of the CUBIC-X brain onto the ABA brain simply by using diffeomorphic registrations such as B-spline transformation or SyN transformation. Thus, I introduced an alternative registration based on the virtual coronal slices. After rough alignment of the CUBIC-X images by above affine transformation, I generated 111 of overlapping 3D coronal slices with a 2.2-mm thickness at a 100-μm step both from the CUBIC-X and ABA brain. Then, each coronal-slice image of the CUBIC-X brain was non-linearly registered onto the coronal-slice images of the ABA brain. As non-linear transformation, I used symmetric normalization model (SyN). I used 100 × 10 × 10 iterations for SyN with the cross-correlation as the similarity metrics. Because the transformation information was output as Affine.txt files for affine transformation and InverseWarp.nii.gz files for non-linear transformation, I can trace the same registration process. In this procedure, each coronal plane of the CUBIC-X brain was mapped 22 times onto the ABA brain. I then calculated the normalized cross-correlations (NCCs) of each CUBIC-X

coronal image with the ABA coronal images. Next, I applied individual cells to 22 different deformation fields, and then calculated 22 different destinations. By referring NCCs of coronal plane images in the individual destinations, I identified the optimal deformation field displaying the highest NCC. According to this procedure, I registered the individual cells of the CUBIC-X brain to ABA brain. Overall, it takes about 3 days with the image processing server to complete whole registration. I noted that the coronal slice-based registration demonstrated a better performance in annotating the detected cells when compared with a simple affine transformation or SyN transformation. After virtual-coronal-slices based registration, I next annotated the detected cells by referring "annotation". I analyzed the annotation data from all of the detected cells, and removed the cells annotated to the out of space of the ABA brain. According to this procedure of registration and annotation, I generated a novel 3D mouse brain atlas with a single-cell resolution and named this pointillistic brain atlas CUBIC-Atlas.

In order to generate 3D annotation region, I applied MATLAB function "alphashape", and input the alpha diameter of 300 as a parameter for each annotated point sets. To generate 2D annotation regions, I extracted point sets in the selected plane with the width of 100 μm. Followed by projection to 2D plane, alpha shape was formed.

Mapping of a Thy1-YFP-H mouse brain onto a CUBIC-Atlas

To see how accurately anatomical annotations of a CUBIC-Atlas are performed, I overlaid cerebral cortical layers of a Thy1-YFP-H mouse brain onto those of CUBIC-Atlas. A Thy1-YFP-H mouse brain was delipidated, PI stained, expanded and gel embedded as described above. Following the imaging of fluorescence of PI and YFP with our customized LSFM, the images were downsampled prior to the registration. The downsampled image of PI signal was then registered onto a CUBIC-Atlas with affine transformation followed by non-linear SyN transformation. The resulting affine matrix and deformation fields were applied to both PI signal and YFP signal. Cerebral cortical layers of a CUBIC-Atlas are also visualized with pseudo colors, and overlaid with the registered images of PI and YFP, respectively.

Whole-brain cell profiling over different aged mice

I performed whole-brain cell profiling of 1-, 3-, 8-week-old and 6-month-old C57BL/6N mice according to the CUBIC-X pipeline. The detected cells in the entire brain were registered and

annotated to the anatomical regions in CUBIC-Atlas as a reference. In this step, I applied an affine transformation and the following non-linear SyN transformation to individual cells in each CUBIC-X image of different aged mice. After registration, I detected the nearest neighbor cell as a reference in CUBIC-Atlas to the cell of interest in the obtained images. To reduce computational cost, I performed this search in the locally allocated grids (120 μm × 120 μm × 120 μm) partitioned from the atlas space. I annotated the corresponding anatomical region of the nearest neighbor cell in CUBIC-Atlas to the region of the cell of interest, and excluded the cells which were annotated to outside of the brain and allocated to outside of the atlas space. To characterize the developmental progression of cell numbers over each age, I first analyzed the average cell number and the standard deviation (SD) over 1-, 3-, 8-week-old, and 6-month-old mice in each region. To calculate these values, I first calculated the average of cell numbers in each area for each developmental stage so that I can eliminate the influence of individual differences in the following analysis. I calculated average cell number and the SD with these values. I calculated the coefficient of variation (CV) which means normalized SD by the average cell number, and mapped CV on the mouse brain schema. The dendrogram schema was constructed by networkX (Hagberg et al., 2008) and Gephi (Bastian et al., 2009) software, and indicated the hierarchical annotation structure of ABA. To investigate the developmental progression of cell numbers across the entire brain, I calculated the normalized cell numbers of each region by setting the cell number averaged over ages to 1.0. For hierarchical clustering analysis, averaged values of the normalized cell number within same age were used. Brain regions were then clustered based on their normalized cell numbers over different ages, using the heatmap.2 function in the gplots R package (Warnes et al., 2009), with Euclidean distance and the "ward.D2" clustering method. Four clusters were determined by "cutree" function in the stats of R package. This clustering analysis revealed four major clusters.

To see how accurately the brains during early postnatal development were anatomically annotated, I visualized the nucleic images of 1-week-old and 3-week-old mice with the anatomical annotations of the detected cells. Cerebral cortical layers of somatosensory areas, posterior parietal association areas, and visual areas are visualized with pseudo colors.

Probabilistic annotation of CUBIC-Atlas

Hyper-activated cells were detected as in our previous paper (Tatsuki et al., 2016), then the detected cells were registered and annotated as above. For probabilistic annotation of the

CUBIC-Atlas, Gaussian probabilistic distribution (σ = 60 μm, in the scale of "after-CUBIC-X") was generated around the registered cells. After integration of the probabilistic distribution generated from all registered cells, I annotated the cell in the atlas by referring to the value of the corresponding location in the resulting activity distribution. The probabilistically annotated cells in CUBIC-Atlas were then clustered with kmean++ algorithm implemented in MATLAB.

STATISTICAL ANALYSIS

Statistical Analysis

Statistical analyses were performed by R version 3.1.0./3.3.1,Origin 2016 (OriginLab, Northampton, MA, USA) and GraphPad Prism.

For the chemical profiling involving functional analysis and pH dependency, normality was evaluated by the Kolmogorov-Smirnov test with a significance level of 0.05. These analyses showed that not all members of the group were normal. The chemical functional group and pH dependency were compared to the control (alcohol group and pH 7-8, respectively) by the Steel test.

For analysis of swelling of gelatin blocks or brains, one-way analysis of variance with Tukey post hoc test was used when the groups were normal distribution with equal variance, or Dunnett's Modified Tukey-Kramer pairwise multiple comparison test was used when groups were normal distribution without equal variance. For comparison of computation time, accuracy metric, normalized cell number, and cell number, Student's t-test was used after confirmation of normal distribution with equal variance.

For the other chemical analyses, normality was evaluated by the Kolmogorov-Smirnov test with a significance level of 0.05. When all of the members of the group were normal, the homogeneous variance for each group was evaluated by Bartlett's test with a significance level of 0.05. When all of the groups were normal distributions with equal variance, the Turkey-Kramer test was used, when the groups were normal distributions without equal variance, the Games-Howell test was used, and otherwise the Steel-Dwass test was applied. In this study, $p < 0.05$ was considered as significant (*$p < 0.05$, **$p < 0.01$, ***$p < 0.001$, and n.s. for not significant evaluations).

SOFTWARE AND DATA AVAILABILITY

Code availability.

The source codes to perform detection of cells as well as mapping and annotation of the detected cells onto CUBIC-Atlas are available from our website (http://cubic-atlas.riken.jp). Our customized MATLAB codes used for the virtual multiplex fluorescence imaging and analysis are publicly available at https://github.com/DSP-sleep/Landscape_pipeline. The other codes used in this study including LabVIEW code that control a custom LSFM are available upon request.

Data availability.

The CUBIC-Atlas can be downloaded from our website (http://cubic-atlas.riken.jp). The data supporting the findings of this study are available upon request.

RESULTS 1

Chemical landscape for tissue clearing based on hydrophilic reagents

Rational chemical profiles for tissue clearing obtained by comprehensively screening more than 1600 CUBIC chemicals

To realize bottom-up design of new clearing reagents, we analyzed critical chemical parameters by performing chemical screening. To comprehensively screen chemicals for hydrophilic chemical-based clearing methods, more than 1600 commercially available chemical candidates were chosen based on their potential solubility in aqueous media (**Figure 2A**). If a chemical was sufficiently soluble in water, a 10%(wt/wt) stock solution was prepared in deionized water without adjusting the pH. These chemical solutions were then subjected to a series of easy and high-throughput CUBIC assays (for pH, fluorescent quenching of FPs, lipid solubility, decoloring, RI matching, decalcification, and swelling) (**Figures 2B-2G**). After the first chemical screening, I narrowed down the candidates by a second evaluation using real tissue. The pH of each stock solution was estimated by the colorimetric analysis of pH-indicator paper (**Figures 3A-3C**). To evaluate the quenching effect of each chemical, recombinant EGFP and Sirius were used as described previously (**Figures 2G** and **3D-3E**) (Susaki et al., 2014).

Delipidation and decoloring

Qualitatively, the lipid solubility of a chemical is inversely correlated with the turbidity of a fixed brain suspension treated with the chemical (Susaki et al., 2014). Thus, I obtained lipid solubility (LS) scores from the OD600 of a mixture of brain suspension and each 10%(wt/wt) chemical solution (**Figure 2B**). I classified the chemicals into three groups: detergents, salts,

and other non-detergent and salt-free chemicals. Anionic and non-ionic detergents with a suitable LogP (octanol-water partition coefficient) value of the hydrophobic group exhibited significantly higher LS while organic salts were less effective (**Figures 4A-4C**). The other water-soluble chemicals were subjected to further functional chemical profiling. Aliphatic amines, aminoalcohols, and aminoethers were found to be the most effective functional groups for lipid solubility (**Figure 4D**). A basic condition (pH > 10) was significantly superior to an acidic one (pH < 6) (**Figure 4E**). To determine the effective chemical parameters for delipidation, I used a multivariate linear regression model. I prepared a series of parameters consisting of three classes, related to functional groups, solubility [calculated by Hansen's solubility parameters (Hansen, 2007)], and structure and topology (**Figure 5A**). **Figure 5B** shows examples of how I counted the functional groups. The model revealed LogP to be the most influential property (**Figure 4F**). Actually, the LS score of less polar amines (LogP ≥ −2.0) was linearly correlated with their LogP (**Figure 4G**). Therefore, water-soluble, relatively hydrophobic, and uncharged amine derivatives had the potential for high lipid solubility. Next, I measured the residual phospholipid and cholesterol contents of mouse brains treated with the chemicals, and evaluated the relative transmittance of these brains after RI matching with the modified Sca*l*eCUBIC-2 (**Figures 4H** and **4I**). The delipidation efficiency, especially for the phospholipid content, was correlated with the final tissue transparency, indicating that delipidation is essential for thorough tissue clearing. Aliphatic amines exhibited a much better delipidation efficiency than aminoalcohols or detergents (**Figure 4J**). Importantly, the LogP value of these chemicals could predict the final transparency of the chemically treated brain (**Figure 4K**). Therefore, the variability within aliphatic amines and N-alcohols could be explained by their LogP value. It is likely that detergents were inferior to aliphatic amines in tissue permeability in spite of their high potential lipophilicity.

I established a high-throughput screening system for the decoloring ability of chemicals by measuring the OD420 of the supernatant obtained from a fixed blood suspension treated with the chemical (Tainaka et al., 2014) (**Figure 2C**). Cationic detergents tended to elute heme more efficiently, while organic salts were significantly less active (**Figure 6A** and **6B**). The pH dependency of the decoloring was also similar to that of the lipid solubility (**Figure 6C**). The functional chemical profiling of the other water-soluble chemicals revealed chemical groups similar to those identified in the lipid solubility assay (**Figure 6D**). I noted that N-alkylimidazoles (CU#0938 and CU#0484) were the most effective decoloring chemicals. Next, I investigated how well these chemicals decolored heme-rich mouse spleen, by soaking this

tissue in the chemical solution and measuring the OD400 of the supernatant. N-alkylimidazole was found to be the best decoloring chemical among several chemical categories (**Figure 6E**). However, since N-alkylimidazole showed a low delipidation efficiency, I further analyzed decoloring chemicals that had a high delipidation efficiency. I applied the multivariate linear regression model to amine groups, and the model revealed the chain length to be the most influential parameter (**Figure 6F**). Actually, multiple polar groups (e.g., $–NH_2$ and –OH) and a longer chain length between the polar groups (C-C length ≥ 3) were associated with efficient decoloring ability (**Figure 6G**).

Among the screened chemicals, I highlight the following four chemicals. CU#0414 (N-butyldiethanolamine) and CU#0070 [1,3-bis(aminomethyl)cyclohexane] are a cost-effective, high-performance aminoalcohol and aliphatic amine, respectively. CU#1051 (1,2-hexanediol) is an exceptional aliphatic diol that acts as a neutral delipidation chemical, and 1-methylimidazole is especially effective for tissue decoloring (**Figure 6H**).

RI matching

To clarify whether the RI value of the medium itself is important for the final transparency or whether specific chemical groups are important for RI homogenization, I used a non-biased approach to determine the best RI-matched chemicals. To develop an alternative high-RI medium based on hydrophilic chemicals, I selected candidate chemicals that had high water solubility and a high RI value per unit weight, because the RI value of aqueous medium increases according to the solute concentration. Chemical profiling of the RI values of 10%(wt/wt) chemical solutions with an Abbe refractometer (**Figure 2D**) revealed that aromatic groups (phenyl, pyridine, and azole groups) exhibited higher RI values among the chemical groups (**Figure 7A**). I then chose candidate chemicals with high RI values ($RI \geq 1.350$) and low absorbance ($OD400 < 0.07$) to avoid incoming light absorption by the medium itself (**Figure 7B**). I chose 21 extremely water-soluble RI-matching candidates, including Histodenz (soluble in water at 60-70 wt%), whose RIs ranged from 1.47 to 1.52. To examine the clearing performance of these chemicals qualitatively, the OD600 of small pieces of chemically treated mouse lung was measured (**Figure 7C**). The RI values of the mounting medium showed no correlation with the tissue transparency, suggesting that the clearing performance does not depend solely on the RI value of the medium but also reflects some chemical properties of the constituent. I further applied the multivariate linear regression model to this result.

Interestingly, the amide group showed a significantly higher clearing performance than the other chemical groups (**Figures 7D**, **7E**, and **7F**). Finally, I introduced CU#0640 (antipyrine) and CU#1283 (N-methylnicotinamide) as RI-matching chemicals (**Figure 7G**). N-methylnicotinamide had the highest clearing performance among the candidates. In addition to its high clearing performance, antipyrine avoided tissue shrinkage, even with a dense solution, because this chemical causes tissue swelling (**Figure 10**).

Decalcification

Inorganic bone mineral mostly consists of carbonated hydroxyapatite (HAp). Thus, I developed an HAp-based screening system to identify potent decalcification chemicals by measuring the OD600 of a chemically treated HAp suspension (**Figure 2E**). The OD600 of HAp suspensions was linearly correlated with the HAp concentration below 10 mg/ml (**Figure 8A**). Decalcification was strongly promoted by an acidic condition, especially below pH 2.0 (**Figure 8B**). Because phosphate ion has a pK_{a1} value of 2.12 (Weast, 1983), the facilitated decalcification under acidic conditions may have been associated with an equilibrium shift in the phosphate ion. Because acid-based decalcification was incompatible with many of the other tissue-clearing steps, we sought other decalcifying chemicals that would act in neutral medium. We found that the decalcification efficiency of a 10 wt% EDTA-Na solution markedly decreased over pH 8.0 (**Figure 8C**). Although this result apparently contradicts the pH dependency of EDTA's stability constant for the calcium ion (Harris, 2011), an unexpected pH dependency was already reported for both the decalcification and demineralization by EDTA (Kiviranta et al., 1980), (Serper and Calt, 2002). This may also reflect the equilibrium shift of the phosphate ion because of its pK_{a2} value of 7.21. It is also noteworthy that a 10 wt% EDTA solution neutralized with CU#0414 exhibited significantly higher decalcification efficiency at pH 8.0 than EDTA-Na (**Figure 8C**), implying that decalcification would be greatly facilitated by neutralization with an organic base instead of an inorganic base, NaOH. Therefore, we screened EDTA-related acids and CU#0414-related organic bases among the listed chemicals. While EDTA-related calcium chelators including CU#0065 (CyDTA) and CU#0624 (PDTA) were the most effective decalcification acids, heterocyclic amines without primary amine were found to be the optimal organic base (**Figures 8D** and **8E**. EDTA-related chemicals (e.g., EDTA, CyDTA, and PDTA) were still superior to other chelators, even to DOTA and EGTA, which have higher stability constants for calcium ion (LogK) than EDTA (**Figure 8F**),

suggesting that the specific chemical nature of EDTA may play an important role in an organic base-assisted decalcification. Collectively, the combined cocktail of EDTA and CU#1352 (imidazole) appeared to be the optimal decalcification solution (**Figure 8G**).

Hyperhydration

To identify the chemicals which achieve hyperhydration of tissue, I used gelatin instead of brains because of the high similarity between PFA-fixed gelatin and PFA-fixed delipidated brains in terms of swelling behavior and isoelectric points (**Figure 9A-9D**). These results prompted me to establish high-throughput screening of swelling agents based on PFA-fixed gelatin gel (type B). To quantitatively evaluate the swelling ability, I measured the water absorption at 975 nm in chemically treated gelatin gel (**Figure 9E** and **10A**). The screening revealed 11 chemicals that have higher swelling ability compared to a conventional swelling chemical, urea (**Figure 10B**), and further screening using mouse brains revealed that 6 chemicals actually swelled the delipidated brain more than urea (**Figure 10C**). We also found that chemicals except amine possess a five-membered backbone structure. I next asked whether these chemicals can promote further swelling if mixed together. To simplify the experiment, I classified these final candidates into three groups, imidazole, pyrazolone and amine groups, based on their chemical structures, and chose a representative chemical from each group. The combinatorial swelling effect was tested in the forms of a mixture or a sequential procedure with fixed gelatin blocks. The result suggested significant synergistic effect of imidazole and antipyrine (**Figure 10D**).

Rapid and scalable tissue clearing by updated CUBIC protocols combining various CUBIC cocktails

The above experiments independently identified a series of CUBIC chemicals with high performance for delipidation, decoloring, RI matching, decalcification, and hyperhydration. Because the requisite chemical properties for tissue clearing differ depending on the nature of the sample (e.g., lipid content, FP expression, existence of bone tissue, etc.), I sought to develop representative CUBIC cocktails that cover existing clearing demands. I began by developing two kinds of delipidation and decoloring cocktails, representing upgrades of Sca*l*eCUBIC-1: one for FP-compatible rapid delipidation and decoloring (CUBIC-L) and another for very rapid

delipidation and decoloring (CUBIC-HL). According to the screening results, N-butyldiethanolamine (CU#0414) and 1,3-bis(aminomethyl)cyclohexane (CU#0070) were chosen for the main component of CUBIC-L and CUBIC-HL, respectively, because they had both high LS and D scores. The combinatorial evaluation of detergents was performed using biological tissues. Since it is difficult to distinguish the clearing performance of individual cocktails under a long incubation time, I applied N-butyldiethanolamine (CU#0414)-based cocktails to mouse brain and kidney, and to human brain with a brief incubation (**Figures 11A**). The cocktail of N-butyldiethanolamine (CU#0414) and Triton X-100 (termed CUBIC-L) exhibited the highest clearing ability for all of the specimens. The delipidation efficiency of all the tested solutions was comparable in mouse brain and kidney, while anionic detergent-based cocktails [sodium dodecyl sulfate (SDS), CU#0631 (sodium dodecylbenzenesulfonate), and CU#0865 (sodium nonanoate)] exhibited slightly higher efficiencies than other solutions in human brain (**Figure 11B**). Notably, the tissue transparency of CUBIC-L was superior to that of other anionic detergent-based cocktails. On the other hand, sodium dodecylbenzenesulfonate (CU#0631) was optimal for clearing human brain and kidney among the 1,3-bis(aminomethyl)cyclohexane (CU#0070)-based cocktails (**Figures 11C** and **11D**). The cocktail of 1,3-bis(aminomethyl)cyclohexane (CU#0070) and sodium dodecylbenzenesulfonate (CU#0631) (termed CUBIC-HL) achieved almost full delipidation. Next, I sought to optimize the RI-matching medium, an upgrade of Sca*l*eCUBIC-2, based on N-methylnicotinamide (CU#1283). Combinatorial experiments revealed that the cocktails of N-methylnicotinamide (CU#1283)-Histodenz and CU#1283-antipyrine (CU#0640) showed much higher clearing performance than the single chemical solutions and other N-methylnicotinamide (CU#1283)-based cocktails (**Figures 11E**). In terms of cost efficiency, I chose the cocktail containing 30 wt% N-methylnicotinamide (CU#1283) and 45 wt% antipyrine (CU#0640) as the RI-matching medium (CUBIC-RA). The even less expensive nicotinamide (CU#0855), a demethylated derivative of CU#1283, served as a convenient surrogate for N-methylnicotinamide (CU#1283) in combination with antipyrine (CU#0640); this cocktail was named CUBIC-R (**Figure 11F**).

We previously reported that a transient perfusion of Sca*l*eCUBIC-1 effectively cleared whole-body samples (Susaki et al., 2015; Tainaka et al., 2014). For this purpose, I introduced an optional CUBIC-L-based perfusion cocktail that included the decoloring-effective 1-methylimidazole, named CUBIC-P. To achieve efficient decalcification compatible with whole-body clearing, I chose the cocktail of 10 wt% EDTA and 15 wt% imidazole (CU#1352),

named CUBIC-B. The proposed CUBIC cocktails except CUBIC-HL sufficiently preserved the fluorescent signal of mCherry (**Figure 12A**). CUBIC-RA is more feasible for various FPs such as EGFP and YFP than CUBIC-R (**Figure 12A**). These series of CUBIC cocktails are summarized in **Figure 12B**, and four CUBIC protocols sequentially combining these cocktails in **Figure 12C**. By applying the protocols to a variety of tissue samples including large human tissues, I demonstrated the effects of the updated CUBIC protocols (**Figures 12D-12I**). To demonstrate how the CUBIC protocols could outperform other clearing methods, I compared CUBIC protocol I with previously reported clearing methods. The final clearing performance of the CUBIC protocols was significantly better than that of other protocols (**Figure 13**).

Inspection of the tissue integrity of CUBIC-treated organs

The updated CUBIC protocol also improved the imaging quality at deeper regions of the sample (**Figures 14A**). Since tissue clearing is often accompanied by macro-scale tissue deformation, I also examined the effect of clearing on the brain macro-shape. Because the final morphology of tissues was influenced by the pH of CUBIC-R, I tested both neutral and weakly basic CUBIC-R. The neutral CUBIC-R showed little deformation, while the weakly basic CUBIC-R exhibited swelling (**Figure 14B**). In addition, a cleared mouse brain (CUBIC protocol I) showed preserved subcellular microstructures (**Figure 14C**). To evaluate protein loss during the clearing process, I quantified the amount of residual protein after a 4-day delipidation using human brain tissue. Most of the endogenous protein was retained in the brain after CUBIC-delipidation, even using the harshest CUBIC-HL protocol (**Figure 14D**). I also tested the antigenicity of delipidated mouse brain by immunohistochemistry using anti-GFAP and anti-NeuN antibodies, and found that the antigenicity was preserved after a 4-day CUBIC-HL treatment (**Figure 14D**). In addition, using various antibodies on delipidated human brain, I observed that the antigenicity remained unaltered after a 9-day CUBIC-L treatment (**Figure 14E**). We further demonstrated the applicability of the protocols for three-dimensional staining using lectin and an anti-SMA antibody on CUBIC-L delipidated human brain (**Figure 14F**). These findings indicated that the proposed protocols largely retain the amount and antigenicity of the proteins.

CUBIC-X for whole-brain expansion with retention of native proteins

To apply the identified chemical for expansion microscopy, I additionally developed the following four-step protocol: 1) tissue delipidation, 2) volume expansion, 3) RI matching, and 4) gel embedding. Brains were delipidated by Sca*l*eCUBIC-1, then immersed in aqueous imidazole solutions as a volume expansion step. The 20% imidazole solution, termed CUBIC-X1, was the minimal concentration to achieve the largest expansion volume (**Figure 15A**). To promote the transparency of expanded brains, I next explored a high RI medium compatible with the expanded brain tissue. Antipyrine, which was another candidate for a swelling reagent, displayed remarkable water solubility and high molar refractivity (**Figure 15B**). I found that the mixture of 5% imidazole and varying amount of antipyrine showed high transparency while maintaining the expansion (**Figure 15D** and **15E**). On the other hand, other examined conventional aqueous RI media could not maintain the expanded size or lack high clearing ability (**Figure 15C-15E**). The clearing performance of an imidazole/antipyrine cocktail was also quantitatively confirmed with USAF chart (**Figure 15G-15I**). In view of handling, I chose the 5%/55% imidazole/antipyrine cocktail (RI = 1.467) as the RI medium, termed CUBIC-X2. In the final 5-day expansion protocol, I obtained a 10-times expanded brain with almost full transparency (**Figure 15D-15F**). For a rigid sample mounting on a microscope, gelation was performed by adding 2% agarose to the CUBIC-X2 medium. CUBIC-X2-based agarose gel was highly transparent and solid (**Figure 16A-16D**). A series of expanded tissue clearing protocol, termed CUBIC-X, was applicable to the fluorescent dye staining of cell nucleus (**Figure 16D**). Furthermore, the CUBIC-X protocol was also compatible with fluorescent reporter proteins by using a modified Sca*l*eCUBIC-1 reagent (5 wt% Quadrol, 10 wt% Triton X-100, and 25 wt% urea) at the delipidation step (**Figure 17A**). I performed LSFM imaging of brains expressing YFP under Thy1, PLP and Mlc1, promoters, demonstrating clear imaging of fluorescent protein deep inside of the tissues (**Figure 17B-17D** and **17F**). High NA (= 1.0) confocal imaging of Thy1-YFP mouse brain suggested the applicability of CUBIC-X to imaging of subcellular structure with CUBIC-X protocol (**Figure 17E**).

Application of CUBIC protocols to comprehensive cellular analysis at the whole-organ scale

We applied our high-performance tissue-clearing CUBIC protocols to the comprehensive cell analysis at the whole-organ scale, enabling extraction of functional cellular assemblies or cell-based organ architecture. First, we comprehensively analyzed the glomeruli in mouse kidney

using CUBIC Protocol I. After nuclear staining, a cleared kidney was embedded in the gel and mounted in the LSFM. To maximize the imaging quality, we used a multi-directional imaging and processing scheme (**Figure 18A**), which achieved the highly resolved volumetric imaging of cell nuclei. To evaluate the imaging quality at the whole-organ scale quantitatively, we applied the discrete cosine transformation Shannon entropy (DCTS, which indicates metric focusness of image) algorithm (Royer et al., 2016) to the imaging data as a robust criterion of imaging quality. The glomeruli were clearly visualized, even in the most deteriorated section of the volumetric images according to DCTS scores, as shown in **Figure 18B**. Then, the renal glomeruli in the whole kidney were comprehensively analyzed by a Hessian-based difference of Gaussian (Zhang et al., 2015) (HLoG, which highlights blob structure). The segmentation accuracy was 94.6% even in the cortex region with the lowest DCTS score (**Figure 18C**). From the spatial distribution of the glomeruli (**Figure 18D-18E**), the kidney was calculated to contain 12,662 total glomeruli, which is comparable to the reported number (Cullen-McEwen et al., 2003; Klingberg et al., 2017).

We performed customized LSFM imaging of nuclear-stained mouse organs by a continuous tiling scheme with a high numerical aperture objective lens (NA = 0.6, 10×, XLPLN10XSVMP, Olympus; **Figure 18F** and **18G**), with the goal of comprehensive cell detection in part of the left medial lobe of the liver and left lung by detecting nuclei. **Figure 18H** and **18I** show representative magnified images at the indicated positions, one of which had the lowest DCTS score (red frame). The cell detection accuracy for the liver and lung was greater than 75% and 79%, respectively. From the analysis, the organs were expressed as an ensemble of detected cellular nuclei ("point cloud"), facilitating extraction of the organ architectures. Duct-like shapes were extracted in both the liver (**Figure 18J** and **18K**) and lung (**Figure 18L** and **18M**), suggesting that the pattern of a certain cell population enables the description of part of a functional component of an organ.

Scalable imaging of mouse whole body including the inside of bone, and of large human organ blocks by CUBIC protocols

To perform exhaustive whole-body imaging, I applied CUBIC protocol II to render transparent the whole body of a P7 mouse, and stained it with nuclear-staining dye (**Figure 19A**). The volume rendered whole-body image showed strong fluorescence inside bones, as seen in the densely concentrated cells in the bone marrow (**Figure 19B**). CUBIC protocol II enabled brain

and spine imaging at single-cell resolution in the skull and backbone (**Figures 19C** and **19D**). Next, I applied this protocol to metastatic bone tumors in the leg of an MDA-231-D-injected mouse (**Figures 19E-19H**), and observed the infiltration of metastatic cancer cells from bone tissue to the adjacent soft tissues.

To examine the scalability of the CUBIC protocols, I applied CUBIC protocol III to large human tissue blocks; a large chunk of dissected human lung (about 43.4 × 16.0 × 26.4 mm^3), dissected human kidneys. Using light-sheet fluorescence microscopy (LSFM), multi-directional imaging was performed to acquire autofluorescence images throughout the blocks. I confirmed that the fluorescent signal was sufficient for imaging even deep within the blocks (**Figures 19I**). To examine the feasibility of volumetric imaging of human kidney at single-cell resolution, I visualized the 3D structure of the glomerulus after nuclear staining. Confocal imaging of the highly cleared tissue enabled the identification and segmentation of glomeruli in the magnified view (**Figure 19J**), and even the comprehensive detection of glomerular cells in the magnified view (**Figures 19K** and **19L**).

I next performed the whole-brain imaging of an adult marmoset. The brain of a 1-year-old male marmoset was cleared using a modified CUBIC protocol I with PI staining, resulting in a cleared PI-stained brain without apparent morphological distortion (**Figure 19P**). The whole brain images were acquired with LSFM and subjected to 3D image reconstitution to generate a volume-rendered image (**Figures 19M** and **19N**). Individual cells were distinguishable even in the deep region of the brain (**Figure 19O**).

Multiple visualization of genetically labeled FPs in mouse brain

Simple immersion-based CUBIC protocols should be applicable and highly reproducible for tissue clearing without the significant quenching of FPs. I next used the CUBIC I protocol combined with the visualization of a series of fluorescently labeled mouse samples. I prepared mouse brains with a wide variety of genetically encoded FPs (Thy1-YFP (Feng et al., 2000), P(CAG)-EGFP (Okabe et al., 1997), Drd1-mVenus (Nagai et al., 2016), Th-EGFP (Matsushita et al., 2002), Mcl1-YFP [Mlc1-tTA (Tanaka et al., 2010)::tetO-YC (Kanemaru et al., 2014)], Plp-YFP [Plp-tTA (Inamura et al., 2012)::tetO-ChR2EYFP (Tanaka et al., 2012)], and Htr5b-YFP [Htr5b-tTA (Tanaka et al., 2012)::tetO-YC]). The brain samples were subjected to the CUBIC I protocol with CUBIC-RA as an RI matching reagent to preserve the FP signals. All

of the brains were treated with a nuclear staining dye (RedDot^{TM}2) for registration, and images were acquired with LSFM, resulting in two volumetric images (one for the nuclear stain and the other for the FP signal) for each brain. I registered the nuclear images to that of a reference brain, and directly compared the FP signals by overlaying their registered images as we reported previously (Susaki et al., 2014; Susaki et al., 2015), thus achieving virtual multiplex whole-brain imaging (**Figures 20A**). The overlaid image made it possible to compare the global distribution of pyramidal neurons (Thy1-YFP), astrocytes (Mlc1-YFP), oligodendrocytes (Plp-YFP), dopaminergic neurons (Th-EGFP), serotonin receptor 5B (Htr5b-YFP), and dopamine receptor D1 (Drd1-mVenus), at the whole-brain scale (**Figures 20B**). This systematic approach to analyzing the global distribution of expressed genes enabled me to investigate the distribution of neural subtypes in the cerebral cortical layers (**Figures 20C** and **20D**). In utero electroporation is another method for introducing an exogenous gene. We unilaterally introduced P(CAG)::mRFP into mouse brain by in utero electroporation (Hayashi-Takagi et al., 2015), and analyzed the spatial distribution of the induced genes by virtual multiplex whole-brain imaging, demonstrating that the mRFPs were mainly expressed into layer 4 (**Figures 20E-20G**). Furthermore, FP expressed in metastatic tumor cells (MDA-231-D cancer cells expressing mCherry) was also clearly visible using CUBIC I protocol, allowing the morphological analysis of cancer metastasis (**Figure 20H**).

So far, I demonstrated single-cell-resolution imaging by combining various CUBIC chemicals. The potential users of these clearing protocols can freely modify the chemical composition by referring the screening result up on their experimental needs. A visual guide of the design strategy is shown in **Figure 21**. In the following chapter, I introduce single-cell-resolution whole-brain atlas. With the atlas, the researchers can collectively analyze cellular information obtained from various whole-brain imaging results.

RESULTS 2

A three-dimensional single-cell-resolution whole-brain atlas

Whole-brain nuclei imaging of a CUBIC-X expanded brain with customized LSFM

Construction of a single-cell-resolution mouse brain atlas requires accurate identification of entire cells in the whole brain. Because of irregular and diversified morphologies of cells, comprehensive identification of cell bodies in a whole brain is challenging. Because relatively uniform round nuclei have facilitated global cell detection and tracing (Keller et al., 2008), I decided to identify the locations of nuclei as a surrogate for cell body. To this end, propidium iodide (PI), an organic small molecule staining DNA, was applied in the following experiments of the whole-brain cell detection. To clarify whether CUBIC-X improves imaging quality, I performed imaging of before- and after-CUBIC-X brains by commercially available low-magnification LSFM. The resulting images revealed highly resolved fluorescent signals from the thalamus, located deep inside a brain (**Figure 22**). I then asked whether a CUBIC-X expanded brain retains original spatial information of nuclei. To verify whether brains hold nuclei during delipidation procedure, I performed sequential observation of the nuclei with 1 mm-thick brains of R26-H2B-EGFP mice. I confirmed none of the nuclei were lost during delipidation procedure (**Figure 23A**). Next, I verified that none of the nuclei were lost during expansion procedure by observing the nuclei in the corresponding regions of before- and after-CUBIC-X brain (**Figure 23B**). Together, I concluded that none of the nuclei were lost during whole procedures to make CUBIC-X brain. The degree of the expansion is not dependent on cell density (**Figure 23C-23E**). I next quantified the amount of distortion in macro-structural scale. By three dimensionally comparing the “Before-CUBIC-X” brain and “After-CUBIC-X” brain, root-mean-square errors (RMS errors) were measured (Chen et al., 2015). RMS errors were estimated less than ~20 μm, which was ~0.8% of the measurement length (2,500 μm) in the investigated regions (**Figure 24A** and **24B**).

In order to visualize CUBIC-X brain in subcellular resolution by LSFM, we implemented a customized LSFM equipped with a long WD detection objective lens (Olympus XLPLN10XSVMP, NA = 0.6, WD = 8 mm) (**Figure 24C** and **Figure 25**). I chose this lens because lens with higher NA (e.g. XLSLPLN25XGMP, NA = 1.0, WD = 8 mm) is highly sensitive to the aberration caused by inhomogeneity of refractive index of a cleared brain. The imaging region was divided into an xy grid, which typically consisted of 17-20 tiles in the x direction and 18-21 tiles in the y direction. The sample was scanned in z direction with a step size of 5 μm to obtain a stack of images. To cover an entire brain, we also introduced rotation sequences (**Figure 24D**). As a result, we obtained clearly resolved images across the brain (**Figure 24E**). We also note that the possible displacements of the imaging sequences were small enough (xy tiling: ≤12 μm, θ tiling: ≤1.3%) to perform following whole-brain cell detection (**Figure 26**). The resulting whole-brain image data was approximately 14 TB with 16-bit raw TIFF format. We also performed whole-brain imaging of brains expressing YFP under PLP and Thy1 promoters. These applications demonstrated subcellular-resolution imaging of fluorescent reporter proteins from whole-mouse brains (**Figure 27**).

Construction of a single-cell-resolution mouse brain atlas (CUBIC-Atlas)

The next challenge towards constructing a single-cell-resolution atlas is accurately detecting all cells from the acquired images (**Figure 28A**). To this end, I devised cell-detection algorithm based on two-step convolution (**Figure 28B** and **28C**), which was analogous to a one-step convolution algorithm developed by Shimada et al (Shimada et al., 2005). In this two-step algorithm, I applied the first convolution with a 2D mean filter of a kernel diameter DM1, resulting an image which has local maximum values at the center of the cellular nuclei (**Figure 28D** and **28E**). I kept the pixels with local maximum values and other pixels were replaced with zero. Then, I unified the multiply-detected cells by performing the second convolution upon this image, with a 3D mean filter of a kernel diameter DM2 (**Figure 28E-28F**). Finally, I detected each cell by finding the local maximum in 3D by automatically comparing determined local thresholds (**Figure 28H**). By tuning diameters of two convolution kernels, DM1 and DM2, I succeeded in the fully-automated cell detection. Evaluated by comparing the result to manual detection, the accuracy metric was more than 94% in interbrain (thalamus), midbrain, and cerebrum (except hippocampus and olfactory bulb granular layer), 91% in hippocampal CA1, 90% in olfactory bulb granular layer, 89% in dentate gyrus and 79% in the densest area,

cerebellum granular layer (**Figure 29**). I did not observe morphology- or size-dependent errors of cell detection with the algorithm. As a result, spatial information of whole-brain cellular nuclei was represented as an ensemble of cellular points with ~3 GB, providing the pointillistic anatomical platform, termed CUBIC-Atlas. The CUBIC-Atlas is an editable platform, which can also accommodate multiple cellular information in single-cell resolution, such as anatomical area, gene expression, cell type and cellular connection. As an initial step, anatomical information was annotated onto CUBIC-Atlas by adopting anatomical annotations in the Allen Brain Atlas (ABA) (Lein et al., 2007). Because the ABA brain was reconstituted from a series of coronal-slice images, I created a registration based on the virtual coronal slices (**Figure 30**). Using this registration, each individual cell in CUBIC-Atlas was assigned an anatomical ID of ABA (**Figure 31A-31I** and **Figure 32**). To examine how accurately CUBIC-Atlas was annotated, a nucleus stained brain of a Thy1-YFP-H mouse was registered onto CUBIC-Atlas. I confirmed that YFP signals of the brain could be accurately mapped to the known anatomical locations such as cerebral cortex layer 5 and layer 6 (Feng et al., 2000) (**Figure 33**).

Whole-brain cell counting of mice

One of the attractive applications of the CUBIC-Atlas is whole-brain cell counting of adult mice. For this purpose, I first sampled three brains of adult C57BL/6N male mice (8-week old), which were then cleared, expanded, imaged and profiled according to the experimental workflow termed CUBIC-X pipeline (**Figure 31J**). As a result, the total cell number in the 8-week-old male mouse brain was counted to be $(7.22 \pm 0.52) \times 10^7$ (the coefficient of variation, CV = 7.14%). I could also register and annotate the detected individual cells to anatomical areas in the CUBIC-Atlas, which provided the cell-number information for the individual brain areas (**Figure 31L**).

To comprehensively analyze regional developmental progression of cell numbers during postnatal development, I also performed whole-brain cell profiling of 1-, 3-week-old and 6-month-old C57BL/6N male mice according to the CUBIC-X pipeline in addition to 8-week-old mice (**Figure 34A**). In this analysis, I focused on the brain areas except the cerebellum and the olfactory bulb due to their morphological change during early postnatal development. I first investigated whether anatomical areas of adult brain atlas could be applied to data sets from younger ages. Automatic annotation of cortical layers based on adult brain atlas was

achieved with high accuracy metric (**Figure 35**). Thus, I applied the anatomical annotations of adult (P56) mouse brain atlas to data sets from other ages, and compared cell numbers in the corresponding areas. To characterize the developmental progression of cell numbers in different brain regions, I analyzed the average cell number and the standard deviation (SD) over 1-, 3-, 8-week, and 6-month-old mice in each area (**Figure 34B** and **34C**), and revealed that a variation of the developmental progression over age highly depended on brain areas. The analysis of coefficient of variation (CV) also supported high variability of the developmental progression of cell numbers (**Figure 34D** and **34E**). To further investigate the developmental progression of cell numbers across the entire brain, I first calculated the normalized cell numbers of each area by setting the cell number averaged over ages to 1.0. To extract the characteristic patterns of developmental progression, I performed hierarchical clustering analysis of the normalized cell numbers (**Figure 34F**). This clustering analysis revealed four major clusters (**Figure 34G** and **34H**). A blue cluster was a largest cluster which spread over the entire brain (**Figure 34I**). On the other hand, pink and yellow clusters were relatively localized in cortex and olfactory area, whereas a purple cluster was localized especially in midbrain (**Figure 34I**).

I next focused on the differences of the normalized cell number between 1- and 3-week old, in which the normalized cell number in purple and yellow clusters markedly increased and decreased, respectively. I first analyzed large brain areas such as cerebrum, interbrain, midbrain and hindbrain, and found that the midbrain displayed a higher increase of cell number than other areas (**Figure 36A**), which was consistent with the enriched distribution of a purple cluster in the midbrain (**Figure 34H** and **34I**). I then mapped the normalized cell number increase between 1- and 3-week old onto the midbrain, which revealed that the cell number increase was enriched in the anterior part of the midbrain (**Figure 36B** and **36C**). During the early postnatal period between 1-week and 3-weeks of age, the normalized cell number significantly increased in the motor-related areas and the behavioral-state-related areas whereas the normalized cell number did not significantly change in the sensory-related areas (**Figure 36D**). These findings in normalized cell numbers were also confirmed by significant changes of actual cell numbers in these areas (**Figure 37A**).

I also expected a decrease of normalized cell numbers in the cortex during early postnatal period according to the enriched distribution of the yellow cluster in the cortex (**Figure 34H** and **34I**). I focused on the cortical areas except layer 1 because the cell numbers of this outermost area of the brain could be influenced by the residual arachnoid matter or the

possible damages during the dissection procedures. As expected, layer 2/3 and 4 displayed a decrease of normalized cell number during early postnatal period (**Figure 36E**). I further analyzed the normalized cell number changes of individual cortical areas between 1- and 3-week old during the early postnatal period and between 3- and 8-week old during the maturation period (**Figure 36F**). This whole-cortex cell profiling demonstrated a decrease of normalized cell numbers during the early postnatal period mainly in the layer 2/3 and 4 of gustatory area (GU), posterior parietal association area (PTL), auditory area (AUD), somatosensory area (SS), motor area (MO), temporal association area (TEa) and visual area (VIS), respectively. Since the visual and primary somatosensory areas were intensively studied in relation to their critical periods (Hensch, 2005), I focused on the layer 2/3 and 4 of these areas and analyzed the temporal patterns of normalized cell numbers in these areas (**Figure 36G**), which demonstrated a significant decrease of normalized cell numbers in the layer 2/3 of these areas as well as actual cell numbers (**Figure 37B** and **37C**). Although there were a number of studies on the decrease of synapses during early postnatal development in the cerebral cortex (Chechik et al., 1998; Hensch, 2005), this observation was, to the best of our best knowledge, the first report on the significant decrease of total cell numbers in the layer 2/3 during the early postnatal development.

Probabilistic annotation of CUBIC-Atlas revealed a functionally distinct structure in granule cell layer of hippocampal dentate gyrus

To demonstrate the power of the CUBIC-Atlas, I applied the atlas to identify the functionally distinct brain areas. Because mammalian brains do not have identical cellular structure due to individual differences, I developed a probabilistic method to define areas within the CUBIC-Atlas (**Figure 38A**). As its initial demonstration, I re-analysed previously published brain image data of Arc-dVenus mice to investigate the pharmacologically activated cells (high dVenus signal) in response to chronic administration of the NMDA-receptor inhibitor (MK-801) (Tatsuki et al., 2016). I first confirmed that the activated cells annotated with the CUBIC-Atlas more frequently emerge in the cerebral cortex (**Figure 38B**), which is consistent with our previous report. By assuming the Gaussian probabilistic distribution around the registered activated cells, I allocated the probabilistic activity to each cell within CUBIC-Atlas, then performed k-means clustering analysis against all cells in the atlas. The results revealed four clusters distinctly emerging at each circadian time (**Figure 38C**). Because the cells of Cluster

1 and Cluster 2 are in the granule cell layer of DG (DG-sg) (**Figure 38D** and **38E**), I further investigated distribution of the clusters over DG-sg. Mapping of the cluster of cells in the DG-sg reveals functional differences between upper DG-sg, where the majority of dorsal cell population belongs to Cluster 1, and lower DG-sg, where most of cells belong to Cluster 2 (**Figure 38F** and **38G**), suggesting the applicability of CUBIC-Atlas to discover new functionally distinct sub-areas. Interestingly, this clear separation of the clusters is consistent with inhomogeneity characteristics of the hippocampus (Fanselow and Dong, 2010). Importantly, discovery of functional areas is possible even without prior anatomical information. Based on these results, I propose a new approach for exploring and mapping of functionally distinct areas by using the single-cell-resolution atlas.

DISCUSSION

In the first part of the study, I proposed a strategy to develop scalable tissue clearing regents. Despite the seeming maturity of these chemical clearing methods, the underlying chemical principle in each clearing step has not been completely understood. Here, I developed a series of novel hydrophilic cocktails using non-biased chemical profiling for delipidation, decoloring, RI matching, decalcification, and hyperhydration. In addition, the findings lead us to ascertain plausible hypotheses for how a certain hydrophilic chemical facilitates tissue clearing.

In the second part of the study, I proposed an editable and sharable single-cell-resolution atlas. To clarify the underlying cellular mechanisms in complex neural circuits, an alternative atlas describing whole-mouse brain as an ensemble of cellular points is promising in addition to the current pixel- or voxel-based brain atlases. Herein, I proposed a novel single-cell-resolution mouse-brain atlas, CUBIC-Atlas. Because CUBIC-Atlas was derived from the seamless three-dimensional images, my atlas would be suitable for analysis of volumetric images generated from cleared brains. The protocol may also play a pivotal role in global analysis of gene expression and neural circuit through continuous update of CUBIC-Atlas by overlaying various cellular functions. Together, these technical platforms will accelerate comprehensive cellular digitalization and standardization of an organ/body.

Clearing chemistry of delipidation and decolorization

Organic salts had poor efficiencies for delipidation and decoloring (**Figures 4A** and **6A**). The undesirable effect of ionic charge in these steps was probably related to its effect on the molecular flux between a tissue and the external medium (Hama et al., 2011; Hou et al., 2015). Deionization by an osmotic-pressure gradient is a straightforward way to increase molecular flux; therefore, non-ionic cocktails that promoted molecular flux were advantageous in these steps. Detergents also had unexpectedly poor efficiencies for the delipidation and decoloring of tissue samples, given their high scores in the in vitro assay (**Figures 4A, 4J, 6A** and **6E**). Tissue

delipidation and decoloring using detergents is often achieved by combining them with other tissue-permeable chemicals (Hama et al., 2015; Susaki et al., 2014) or with chemophysical assistance (Chung et al., 2013; Murray et al., 2015; Tainaka et al., 2014; Yang et al., 2014). Detergents generally show slow tissue-permeation kinetics due to large micelle formation, which could explain their poor efficiency in tissue. In contrast, amine derivatives with higher LogP values are expected to be more cell-permeable and more miscible with hydrophobic lipids. Among the current decoloring reagents, N-alkylimidazole showed the highest decoloring ability. N-alkylimidazole facilitates heme elution under basic conditions by competing with histidine for binding to the heme iron center.

Clearing chemistry of RI matching

In the RI-matching step, an external medium with a high RI value similar to that of endogenous proteins (RI ≥ 1.45) replaces the low-RI water (RI = 1.33) inside tissue. The final tissue transparency improves as the RI value of the medium increases (up to 1.52) under a given chemical composition (Kubota et al., 2017). Organic solvent-based RI media have high RI values (e.g., BABB; 1.56 and DBE; 1.56). Our chemical profiling demonstrated that aromatic groups have high RI values, due to their high electron density (**Figure 7A**). Thus, an aromatic derivative is likely to be a suitable constituent of RI media. In addition, the tissue-clearing performance in a variety of RI media demonstrated that the final transparency was determined not only by the RI value but also by the chemical nature of the components of the RI medium (**Figures 7C** and **7E**). Among the clearing protocols including intensive delipidation, sugar-based RI medium (Sca*l*eCUBIC-2) elicits moderate clearing compared with RI media consisting of contrast reagents (CLARITY, RIMS, and SWITCH). The effectiveness of antipyrine and nicotinamide in the screen indicated that the high clearing efficiency of contrast reagents is due to their aromatic amide group. Since highly delipidated tissues are regarded as protein-based biomaterials (**Figure 9**), it is plausible that hydrophilic aromatic amides contributed to RI homogenization due to their efficient solvation of protein backbone amides. A future strategy for improving RI media will be to explore chemical combinations that promote the solvation of the major proteins in tissues.

Clearing chemistry of decalcification

The solid-phase dissolution of mineralized HAp is thought to undergo complex chemical processes, because HAp [$Ca_{10}(PO_4)_6(OH)_2$] is potentially converted to a variety of calcium orthophosphate intermediates {e.g., octacalcium phosphate [$Ca_8(HPO_4)_2(PO_4)_4 \cdot 5H_2O$], dicalcium phosphate dehydrate (DCPD; $CaHPO_4 \cdot 2H_2O$)} (Wang and Nancollas, 2008). Octacalcium phosphate crystals, a possible precursor of HAp, can transform into HAp crystals as the solution pH increases from 4.4 to 6.7, via the deprotonation of HPO_4^{2-} (Tseng et al., 2006). The concentration solubility product (K_{sp}) of octacalcium phosphate [$-\log(K_{sp}) = 98.6$ at 37°C] is higher than that of HAp [$-\log(K_{sp}) = 117.2$ at 37 ℃] (Wang and Nancollas, 2008). While HAp is the most stable phase at pH values above 4.0, DCPD is more stable than HAp at pH values below 4.0 (Johnsson and Nancollas, 1992). The solubility of DCPD [$-\log(K_{sp}) = 6.73$ at 37 ℃] is also higher than that of HAp (Harries et al., 1986; Koutsoukos et al., 1980). Therefore, the protonation of phosphate ions contributed to the decalcification process observed in our experiments (**Figures 8C** and **8D**). Although the apparent stability constant of EDTA for calcium ion decreases from pH 6.0 to pH 12.0 [$\alpha_{Y-4} = 2.3 \times 10^{-5}$ at pH 6.0, and 0.98 at pH 12.0 (Harris, 2011)], decalcification by EDTA-Na was most effective at pH 6.0 (**Figure 8C**). This finding indicates that phosphate protonation is more important in this reaction than Ca^{2+} chelation. The organic base-assisted decalcification by EDTA would be caused by the increased phosphate protonation by organic bases as a proton source, and by the increased chelating ability of EDTA under more alkaline pH conditions. Thus, both the chelating ability and phosphate protonation should be taken into account to improve the decalcification efficiency of CUBIC-B.

Clearing chemistry of hyperhydration

Hyperhydration urea is known to be a relatively weak denaturant for proteins and nucleic acids by disturbing their hydrogen bonding networks (Hua et al., 2008; Priyakumar et al., 2009). The Miyawaki group serendipitously discovered the clearing properties of urea for brain tissues and the accompanying tissue expansion (Hama et al., 2011). As a result of the screening, we identified three chemical groups including 6 hydrophilic reagents with a higher swelling ability for whole brain samples compared to urea. An isoelectric point of the fixed brain protein was shifted in the acidic direction probably because basic amino groups such as lysine would be largely consumed by the crosslink reaction during PFA fixation (Tainaka et al., 2016). Thus, a basic amine group such as 2-aminoethanol (AE #0259) and diethylenetriamine (DET #0780)

would be expected to show significant swelling ability of the brain by inducing electrostatic repulsion between anionic carboxyl groups inside tissues. Interestingly, the other four chemicals except the amine group possess a five-membered backbone structure. In particular, 2-Imidazolidinone (IM-L #1040), which is composed of a cyclized structure of urea by two methylene groups, had higher swelling ability than urea. Additionally, both imidazole- and pyrazolone-based chemicals also significantly swelled brain samples compared to urea. Therefore, the denaturants with a five-membered heterocycle were characterized as the highest hyperhydration reagents among hydrophilic chemicals.

Rational design of various CUBIC tissue clearing protocols

As described above, chemical screening revealed important chemical parameters for each step of tissue clearing, which could not be obtained by modification of existing clearing protocols. There are numerous possible biological applications for tissue clearing, but demands for the clearing protocols differs depending on the sample size, labeling methods, type of organs, and degree of transparency. Based on our screening result, the researchers can design novel clearing cocktail optimized for their own purposes while skipping the process to identify new clearing chemicals. It is also possible to synthesize new clearing chemicals referring the parameters for tissue clearing. Though it is beyond the scope of this study, designing chemicals toward clearing of a whole-human organ is of potential interests. In this study, I proposed clearing protocols to demonstrate whole-body clearing including bones, large human tissue clearing compatible with antibody staining, and reproducible clearing of the transgenic mouse brains.

Furthermore, I developed an expansion microscopy protocol, termed CUBIC-X. As shown in **Figure 17E**, CUBIC-X expanded brains holding sub-cellular structure of neurons. Although the expansion ratio of CUBIC-X is smaller than previously reported expansion protocols (Chen et al., 2015; Ku et al., 2016; Treweek et al., 2015), availability of fluorescent protein without special anchoring gel matrices or complicated immunostaining procedures could simplify experimental protocols. Importantly, the expansion can be performed in whole-organ scale, therefore, researchers could avoid the possible disruption of microscale structure or cellular circuit caused by sectioning of tissues.

It is of note that the updated protocols have a few potential limitations. Since both of the delipidation cocktails are alkaline-buffered solutions, almost all of the endogenous RNA

would be degraded. To perform RNA profiling, a CU#1051-based delipidation cocktail needs to be developed. In addition, much of the presynaptic and postsynaptic fabric is reported to disappear with thorough delipidation protocols such as 3DISCO, PACT, and the original Sca*l*eCUBIC (Hama et al., 2015). Therefore, the protocols would be not suitable for the observation of these structures by electron microscopy. Furthermore, while the decoloring reagents are effective for bleaching porphyrine-related pigments such as myoglobin and cytochrome c, they are unlikely to affect melanin, which is formed by the oxidative polymerization of amino acids (Sealy et al., 1980). Another decoloring strategy is needed to bleach such polymerized pigments. I observed unexpected quenching of EGFP and YFP after application of CUBIC-R (**Figure 12A**). There seems to be compatibility between CUBIC chemicals and fluorophores. Therefore, quantitative checking of compatibilities of dyes with CUBIC reagents are highly recommended prior to tissue clearing.

Application of CUBIC chemicals in hydrogel-tissue chemistry

Though the CUBIC protocols proposed in this study assume tissue clearing with passive immersion, the screened chemicals could be applicable to tissue clearing with hydrogel-tissue chemistry (HTC) (Gradinaru et al., 2018). In clearing with HTC, SDS is most commonly used anionic detergent. Our screening suggests CU#0631 (sodium dodecylbenzenesulfonate) as a potential alternative of SDS, which also demonstrated high delipidating ability (**Figure 11B** and **11D**). One of the advantages of HTC exist in the tight scaffolding of endogenous molecules, thus allowing the aggressive clearing using electric forces or thermal energy. This characteristic of HTC could be fully harnessed when combined with the screened chemicals with high lipid solubility scores such as CU#0070. I observed CU#0070 could disrupt structure of mouse brains if incubated at 50 ℃ (data not shown). Such structural disruption could be avoided if combined with harder fixation with glutaraldehyde (Murray et al., 2015) while accelerating the speed of delipidation. Since HTC also allows observation of small molecules by covalently linking to the scaffold (Murray et al., 2015), combination of HTC with CUBIC may enable the exploration of more diverse molecules than proteins and DNA.

Development of CUBIC-Atlas with CUBIC-X expansion protocol and single-cell resolution imaging

Since whole-organ imaging technologies have been developing, CUBIC-Atlas would contribute to this field with this single-cell-resolution atlas publicly available. Therefore, I established a universal data-sharing platform of CUBIC-Atlas (http://cubic-atlas.riken.jp) via an open source web-based viewer and annotation editor, the Collaborative Annotation Toolkit for Massive Amounts of Image Data (CATMAID) (Saalfeld et al., 2009) (**Figure 38H**). In this CATMAID based CUBIC-Atlas viewer/editor, annotators could assemble novel annotations such as gene expression profiling, phenotyping of individual cells, and functional connections of individual neural circuits. I put CUBIC-Atlas data and source codes on our webpage (http://cubic-atlas.riken.jp) to perform detection of cells as well as mapping and annotation of the detected cells onto CUBIC-Atlas.

Whole-brain analysis of cells using CUBIC-Atlas

As the application of CUBIC-X pipeline and CUBIC-Atlas, I performed whole-brain cell counting. Quantification of cell numbers in the mammalian central nervous system has been one of the most fundamental and technical challenges in neuroanatomy (Herculano-Houzel et al., 2011; von Bartheld et al., 2016). For mice, the total cell numbers in brains of various strains have been reported (Herculano-Houzel et al., 2006; Herculano-Houzel et al., 2011). The reported total cell numbers range from less than 6.0×10^7 (Herculano-Houzel et al., 2015) to more than 15.0×10^7 (Seiriki et al., 2017). This large variation of the total cell numbers is assumed to be derived from genetic background, age, sex and individual differences. In my study, I reported the total cell numbers of C57BL/6N male mouse brain (8-week old) to be $(7.22 \pm 0.52) \times 10^7$. I also note that my cell detection algorithm tends to underestimate the cell number rather than overestimate especially in densely populated areas (**Figure 29F**), thus, I assume this total cell number to be a lower bound estimate. The underestimation of the cell numbers may derive from the followings. First, the algorithm tends to detect the inter-nuclei space as a centroid in the densely populated area (**Figure 29E**). This is because the first convolution step could generate artificial intensity peaks in the inter-nuclei space. Second, the automatically determined threshold of the background intensity can be overestimated in the densely populated area. The threshold was determined by referring the histogram of intensity (See also **Materials and Methods**). The mode of the histogram, which is used for the determination of the threshold, can be influenced by the density of nuclei. This shift of the mode will end in the overestimation of background intensity, dismissing the nuclei centroids as background. I also note that the

algorithm is not suitable for the detection of objects with irregular shape, such as cell bodies. Further improvement of axial resolution of LSFM will improve accuracy in the densely populated areas such as the granular cell layer of cerebellum. Since CUBIC-X pipeline allows not only counting the cell numbers but also identification of cellular locations, the application of the pipeline to the pathological analysis is intriguing. In some neurological disorders such as Parkinson's disease and depression, neuronal death or disfunction of neurogenesis in the specific part of brains are observed (Dauer and Przedborski, 2003; Sahay and Hen, 2007). Although the local estimation of the number of neurons was extensively performed, whole-brain-wide comprehensive analysis of cell numbers of these disease model mice is yet to be achieved. Such analysis is promising application of CUBIC-Atlas and will provide insight to neurological disorders.

CUBIC-Atlas also revealed a significant decrease in cell number in the layer 2/3 of visual and somatosensory area during early postnatal development (**Figure 36)**. It has been reported that neural cell death of the pre-synaptic neuron can be induced by deletion of their post-synaptic target (Cowan et al., 1984; Vanderhaeghen and Cheng, 2010). In the visual cortex, the neuronal circuit was reorganized by synaptic pruning mediated by protease from the extracellular matrix during postnatal critical periods (Hensch, 2005). Therefore, the observed cell number decrease in this study might reflect the apoptosis of neuronal cells in those areas due to post-synaptic pruning. Other possible explanations for the decrease in cell numbers are early post-natal glial apoptosis and cortical cellular migration (Rice and Barone, 2000). Since CUBIC-X protocol is compatible with cellular labelling with fluorescent protein and fluorescent molecule, profiling of cell types and tracking cellular migration during critical periods are interesting applications of CUBIC-Atlas as the future study. Regardless of these inhomogeneous cellular progression during development, it is note worth that the cellular proliferation seems to be generally constant over brain (**Figure 34D**). Another promising application of CUBIC-X protocol is imaging with super-resolution microscope. As shown in **Figure 17E** and **Figure 27H**, CUBIC-X expanded brains hold sub-cellular structure of neurons. Though the cellular-level morphological distortion is yet to be analyzed in CUBIC-X, the simple immersion-based protocol facilitates researchers to perform super-resolution imaging.

An unbiased analysis to discover the previously unknown area is one of the most attractive application of CUBIC-Atlas. In this study, I confirmed the existence of novel sub-areas in granule cell layer of DG by probabilistically mapping spatial information of

pharmacologically activated cells (**Figure 37**). This application not only demonstrates the feasibility of activity mapping with CUBIC-Atlas, but also proposes an approach to re-define anatomical areas. This bottom-up approach to build a mammalian brain atlas is synergistic with the previously reported histologically annotated atlas. In the case of my study, both information of probabilistic annotation (spatial information of Arc-dVenus expressing cells) and the prior annotation (DG-sg) lead the discovery of functionally distinct sub-area in DG-sg. The utilization of analytic tools to handle point cloud data such as point cloud library (Rusu and Cousins, 2011) will further assist cellular description of the mouse brain.

In the study, I have demonstrated the single-cell-resolution imaging of various endogenous molecules with tissue clearing (**Table 2**). These clearing protocols will allow whole-brain analysis of gene-expression status in disease model mice as well as in healthy mice. CUBIC-Atlas further assists comprehensive analysis of the changes in gene-expression pattern, leading discoveries of unreported cellular population. By combining emerging cellular perturbation techniques, optogenetics or chemogenetics, we are able to identify the function of the cells, which is not possible with tissue clearing alone. Such sub-population analysis can uncover the neuronal basis behind the pathological behavior.

Future Perspectives of Comprehensive Whole-organ/body Analysis with Cellular Resolution

The concept of single-cell-resolution is also applicable to other mouse organs. As a preliminary demonstration, the comprehensive cell detections with a partial lung and a partial liver was performed (**Figure 18**). Since the current accuracy of cell-detection is not high for these organs, further modifications in CUBIC protocols, a microscope, and cell-detection algorithm are needed. Though technically challenging, construction of atlases for large tissues such as whole-human organs is fascinating. Comparative analysis of post-mortal diseased organs and healthy organs will reveal the cellular basis of the abnormality of our health. To make whole-human organs transparent, the use of a physicochemical technique such as electrophoresis might be helpful (Chung et al., 2013).

The volumetric labelling of endogenous molecules is another challenge. Immunohistochemistry, which is a widely used histological method based on antigen-antibody interaction, has been performed with various mouse organs (Renier et al., 2014; Tainaka et al., 2014). The limitation of this technique lies in the fact that the variation of target molecules is

largely limited by the varieties of antibody. Another widely used histological method is fluorescent in situ hybridization (FISH). Three-dimensional FISH is highly demanded for the completion of the whole-organ analysis of cells because the flexible design of nucleic acid enables us to explore the expression of almost all types of genes and functional RNAs. None of the researches have reported successful labelling of RNA in whole-mouse organs or body though handful studies show volumetric FISH in small size of tissues (Long et al., 2017; Sylwestrak et al., 2016). This is supposed to be due to the fragile nature of the RNA molecules. High pH, long-term incubation in high temperature, covalent ion concentration, and RNase contamination are the representative causes of hydrolysis of RNA. In our screened chemicals, I identified RNA friendly neutral delipidating chemical such as #1051. Using these chemicals may enable clearing of organs while preserving native RNA.

Once combined with these labelling techniques, the single-cell-resolution atlas will uncover various biological questions. One of the most intriguing application is the analysis of development and evolution of mammalian brains. Detailed chronological observation of brains will disclose how single zygote generates the complex cellular network in the brain. Moreover, inter-species cellular-resolution comparison of brains will enable tracking the history of neuronal evolution. So far, a large number of research has been performed over what makes us human (Sousa et al., 2017), but the human-specific critical cellular trait is yet to be identified. A systematic study of ontogeny and phylogeny using single-cell-resolution brain atlas will provide the key to answer this fundamental question. I thus believe that the single-cell-resolution atlas will open the new research field in neuroanatomy.

TABLE AND FIGURES

Reference	Protocol	Fixation	Permeabilization	Decoloring	RI match	RI	Clearing Performance
Dodt et al., 2007; Schwarz et al., 2014	BABB	PFA	EtOH, 1-PrOH, or *t*-BuOH; dehydration CH_2Cl_2 (DCM); delipidation		Benzylalcohol/ Benzylbenzoate	1.56	High 3-4
Becker et al., 2010; Ertürk et al., 2012; Renier et al., 2014	3DISCO, iDISCO	PFA	THF; dehydration and delipidation CH_2Cl_2 (DCM); delipidation	H_2O_2; Heme and other chromophore	Dibenzylether (DBE)	1.56	Highest 5
Aoyagi et al., 2015; Costantini et al., 2015	TDE	PFA	2,2'-Thiodiethanol (TDE); dehydration		TDE	1.48-1.52	Moderate 1
Kuwajima et al., 2011	*Clear*^{T}, *Clear*^{T2}	PFA	Formamide; dehydration or formamide-induced molecular influx		Formamide/ Polyethylene glycol	1.45	Moderate 1
Hama et al., 2011	Sca*l*e	PFA	Sca*l*eA2: Urea/Glycerol/Triton X-100 Urea; hydration and molecular influx		Sca*l*eA2	1.38	Moderate 1
Hou et al., 2015	FRUIT	PFA	FRUIT: Urea/Fructose Urea; hydration and molecular influx Fructose; osmotically balanced molecular flux	Thioglycerol; Maillard Reaction	FRUIT: Urea/Fructose	1.46-1.50	Moderate 1-2
Hama et al., 2015	Sca*l*eS	PFA	Sca*l*eS: Urea/Sorbitol/DMSO Urea; hydration and molecular influx Sorbitol; osmotically balanced molecular flux		Sca*l*eS4: Urea/Sorbitol/DMSO	1.44	High 2-3
Ke et al., 2013	SeeDB	PFA	Fructose; osmotically balanced molecular flux	Thioglycerol; Maillard reaction	Fructose	1.49	Moderate 1
Susaki et al., 2014, 2015; Tainaka et al., 2014	CUBIC	PFA	Sca*l*eCUBIC-1: Urea/Aminoalcohol/Triton X-100 Urea; hydration and molecular influx Aminoalcohol/Triton X-100; delipidation	Aminoalcohol; Heme	Sca*l*eCUBIC-2: Urea/Aminoalcohol/ Sucrose	1.49	High 3-4
Susaki et al., 2016	CUBIC	PFA	Sca*l*eCUBIC-1A: Urea/Aminoalcohol/Triton X-100/ NaCl Urea/NaCl; osmotically balanced molecular flux Aminoalcohol/Triton X-100; delipidation	Aminoalcohol; Heme	Sca*l*eCUBIC-2: Urea/Aminoalcohol/ Sucrose	1.49	High 3-4
Economo et al., 2016		PFA	Sca*l*eCUBIC-1: Urea/Aminoalcohol/Triton X-100 Urea; hydration and molecular influx Aminoalcohol/Triton X-100; delipidation	Aminoalcohol; Heme	DMSO/Sorbitol	1.47	High 3-4
Chung et al., 2013; Tomer et al., 2014	CLARITY	PFA/Acrylamide /Bis-acrylamide	SDS; delipidation SDS delipidation by electrophoresis	SDS; Heme	FocusClear™, Glycerol, or RI 1.454 cat. no. 1806Y (Cargille Labs)	1.45	Passive clearing; High 3-4 ETC clearing; Highest 4-5
Yang et al., 2014; Treweek et al., 2015	PACT-PARS	1)PFA, 2)Acrylamide	SDS; delipidation SDS delipidation by transcardial perfusion (PARS) EDTA; decalcification (decalPACT)	SDS; Heme, Sudan Black B; Lipofuscin autofluorescence	RIMS: Histodenz™ or sRIMS: sorbitol	RIMS; 1.46-1.49, sRIMS; 1.44	PACT; High 3 PARS; Highest 3-5
	ePACT	1) PFA, 2) Acrylamide/ Bis-acrylamide/ Sodium acrylate	SDS; delipidation Fibers digested by collagenase		Deionized water	1.33	
Costantini et al., 2015	CLARITY-TDE	PFA/Acrylamide /Bis-acrylamide	SDS; delipidation SDS delipidation by electrophoresis	SDS; Heme	TDE	1.45	Highest 4-5
Kim et al., 2015	Stochastic Electrotransport	PFA/Acrylamide /Bis-acrylamide	SDS; delipidation SDS delipidation by stochastic electrotransport	SDS; Heme	Diatrizoic acid/ *N*-methylglucamine/ Sorbitol	1.46	Highest 5
Chen et al., 2015	Expansion Microscopy	1) PFA, 2) Acrylamide/ Bis-acrylamide/ Sodium acrylate	Fibers digested by protease		Deionized water	1.33	
Murray et al., 2015	SWITCH	Glutaraldehyde	SDS; delipidation SDS delipidation by thermal energy (80°C incubation)	Thioglycerol or sodium sulfite; Maillard reaction	Diatrizoic acid/ *N*-methylglucamine/ Sorbitol	1.47	Highest 5

Table 1. Tissue-clearing protocols for mammalian tissues (Tainaka et al., 2016)

	FP	Immunostaining	DNA staining with small molecule	in situ hybridization
CUBIC protocol I	yes	yes	yes	
CUBIC protocol II	yes		yes	
CUBIC protocol III	no	yes	yes	
CUBIC protocol IV		yes	yes	
CUBIC-X	yes		yes	

Blank means that data is not investigated in this study.

Table 2. Compatibilities of CUBIC protocols with various staining techniques.

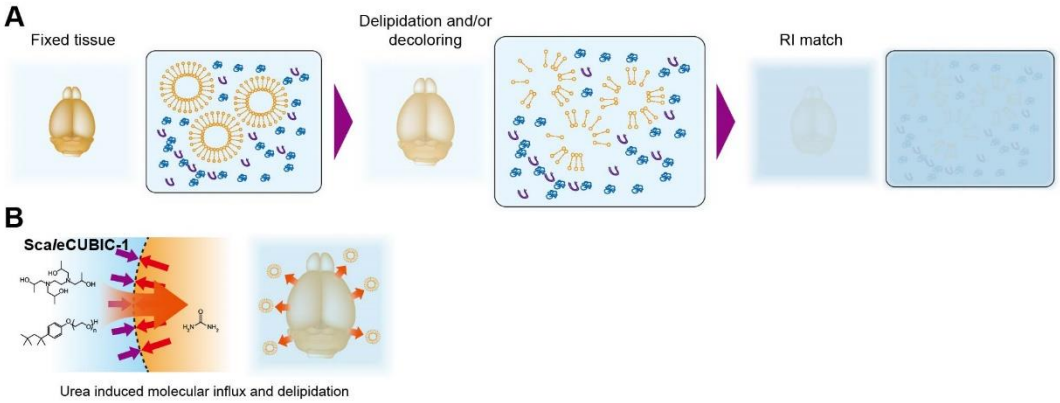

Figure 1. Physical mechanism of tissue clearing (modified from Tainaka et al., 2016).

(A) Physical mechanism of tissue clearing. (B) Urea, one of the hyperhydrating chemicals, is supposed to promote influx of delipidating chemical in the CUBIC protocol (Susaki et al., 2014).

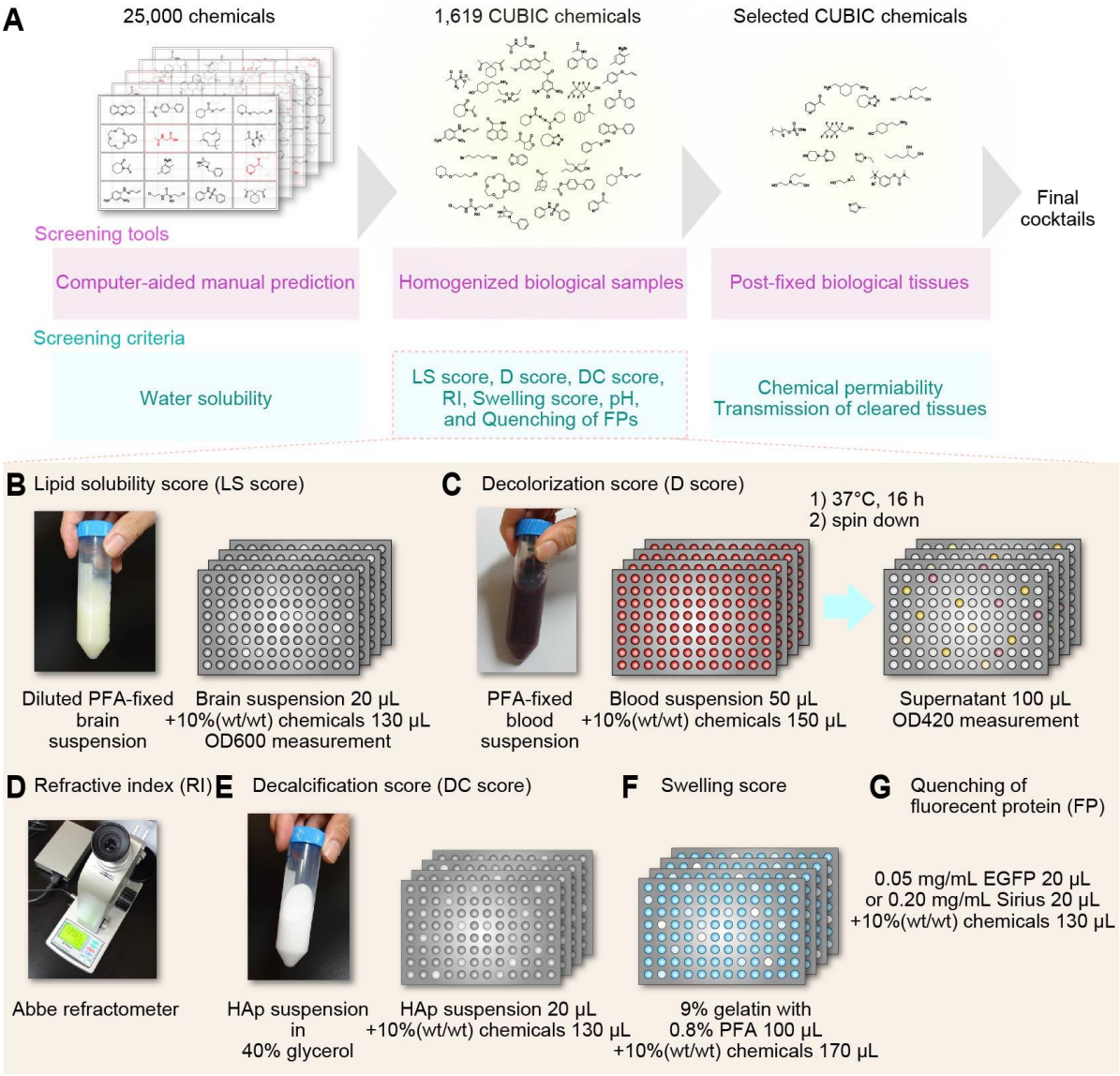

Figure 2. Strategy for screening more than 1600 CUBIC chemicals.

(A) Experimental overview of the screening of more than 1600 CUBIC chemicals. In the first in vitro screening, six chemical properties of potentially water-soluble CUBIC chemicals were quantitatively evaluated. In the second evaluation using real tissue samples, the candidate chemicals were narrowed down. (B-G) Experimental scheme for the high-throughput chemical screening of delipidation (B), decoloring (C), RI measurement (D), decalcification (E), swelling (F) and FP fluorescence measurement (G). A popular FP, EGFP, and pH-insensitive FP, Sirius, were used.

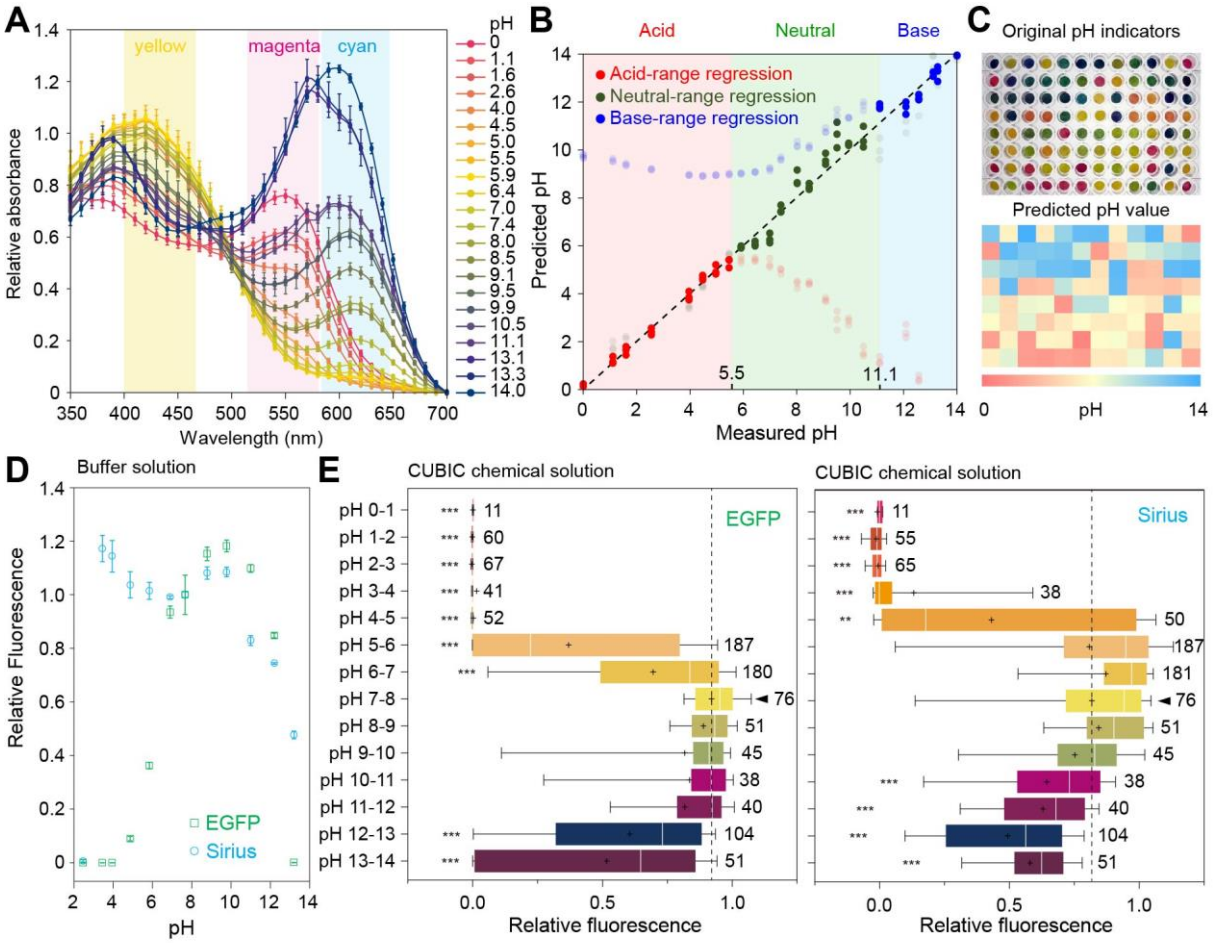

Figure 3. High-throughput pH and Fluorescent Protein (FP) Signal Quenching Estimation Assay.

(A) Absorbance spectra of pH indicator papers after their immersion in pH standard solutions. To determine the pH of the chemical solutions, I measured the absorbance at 550, 570, 610, and 660 nm of pH indicators soaked in each chemical solution. Data are mean ± SD (n = 3). (B) Relationship between predicted pH and measured pH with three regression models. The pH of chemicals was first evaluated with the neutral-range regression model, then regressed again with an acid-range or base-range regression model for more accuracy. (C) Image of the pH indicators soaked in CUBIC chemical solutions (top) and predicted pH (bottom). (D) pH dependency of the relative intensity of each FP in buffer solutions. Various pH conditions were examined. Data are mean ± SD (n = 2). (E) Dependency of the relative fluorescence intensity of EGFP (left) and Sirius (right) on the pH of CUBIC chemical solutions compared with pH 7-8. Box and whisker plots show the 25th–75th percentile (boxes), 10th–90th percentile (whiskers), median (vertical lines), and mean (cross). The numbers next to the plots are the numbers of the chemicals. **p < 0.01, and ***p < 0.001.

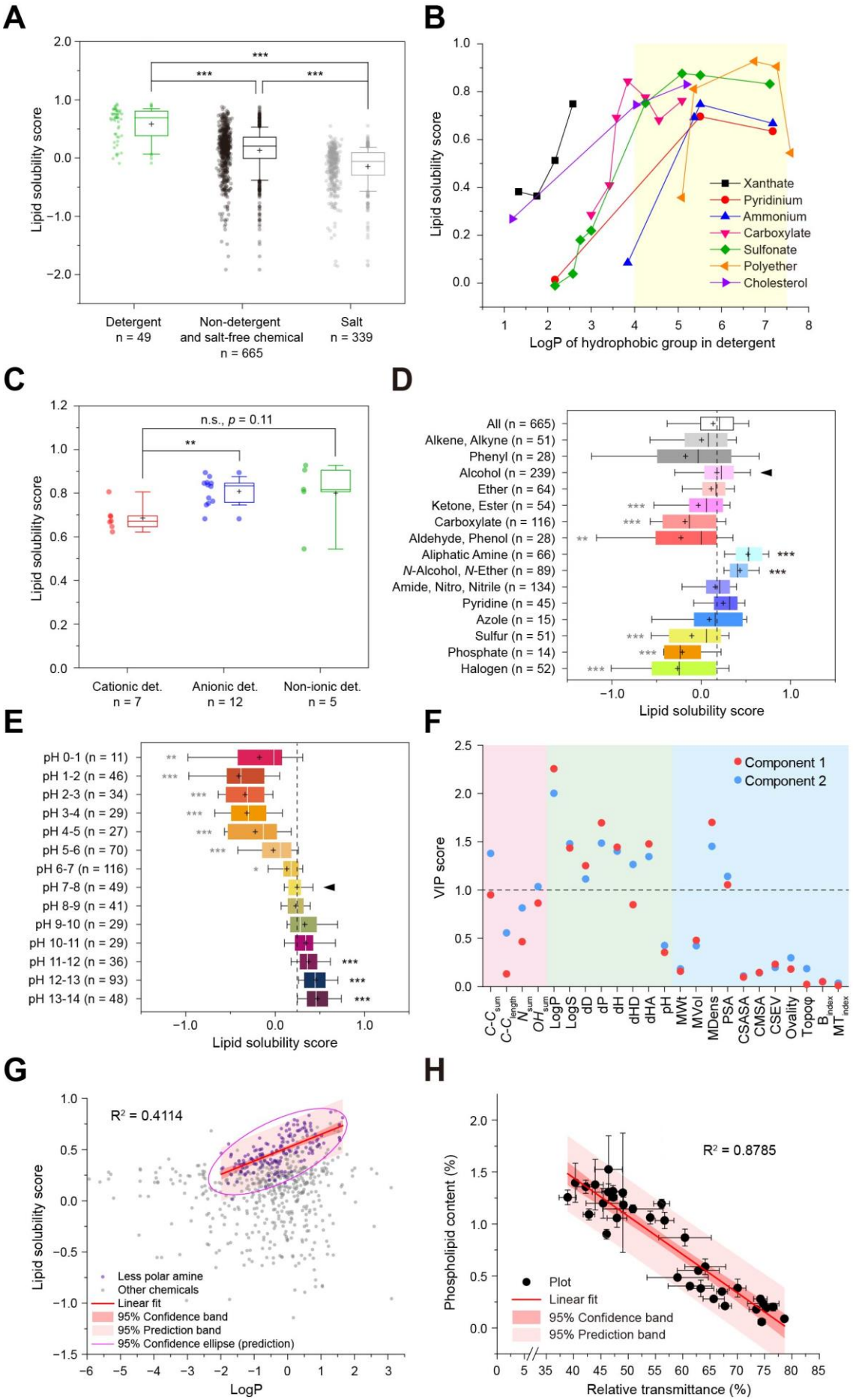
A
Lipid solubility score
***
***
***
Detergent
n = 49
Non-detergent
and salt-free chemical
n = 665
Salt
n = 339
B
Lipid solubility score
Xanthate
Pyridinium
Ammonium
Carboxylate
Sulfonate
Polyether
Cholesterol
LogP of hydrophobic group in detergent
C
Lipid solubility score
n.s., p = 0.11
**
Cationic det.
n = 7
Anionic det.
n = 12
Non-ionic det.
n = 5
D
All (n = 665)
Alkene, Alkyne (n = 51)
Phenyl (n = 28)
Alcohol (n = 239)
Ether (n = 64)
Ketone, Ester (n = 54)
Carboxylate (n = 116)
Aldehyde, Phenol (n = 28)
Aliphatic Amine (n = 66)
N-Alcohol, N-Ether (n = 89)
Amide, Nitro, Nitrile (n = 134)
Pyridine (n = 45)
Azole (n = 15)
Sulfur (n = 51)
Phosphate (n = 14)
Halogen (n = 52)
Lipid solubility score
E
pH 0-1 (n = 11)
pH 1-2 (n = 46)
pH 2-3 (n = 34)
pH 3-4 (n = 29)
pH 4-5 (n = 27)
pH 5-6 (n = 70)
pH 6-7 (n = 116)
pH 7-8 (n = 49)
pH 8-9 (n = 41)
pH 9-10 (n = 29)
pH 10-11 (n = 29)
pH 11-12 (n = 36)
pH 12-13 (n = 93)
pH 13-14 (n = 48)
Lipid solubility score
F
Component 1
Component 2
VIP score
C-C sum
C-C length
N sum
OH sum
LogP
LogS
dD
dP
dH
dHD
dHA
pH
MWt
MVol
MDens
PSA
CSASA
CMSA
CSEV
Ovality
Topoφ
B index
MT index
G
R² = 0.4114
Lipid solubility score
Less polar amine
Other chemicals
Linear fit
95% Confidence band
95% Prediction band
95% Confidence ellipse (prediction)
LogP
H
R² = 0.8785
Phospholipid content (%)
Plot
Linear fit
95% Confidence band
95% Prediction band
Relative transmittance (%)

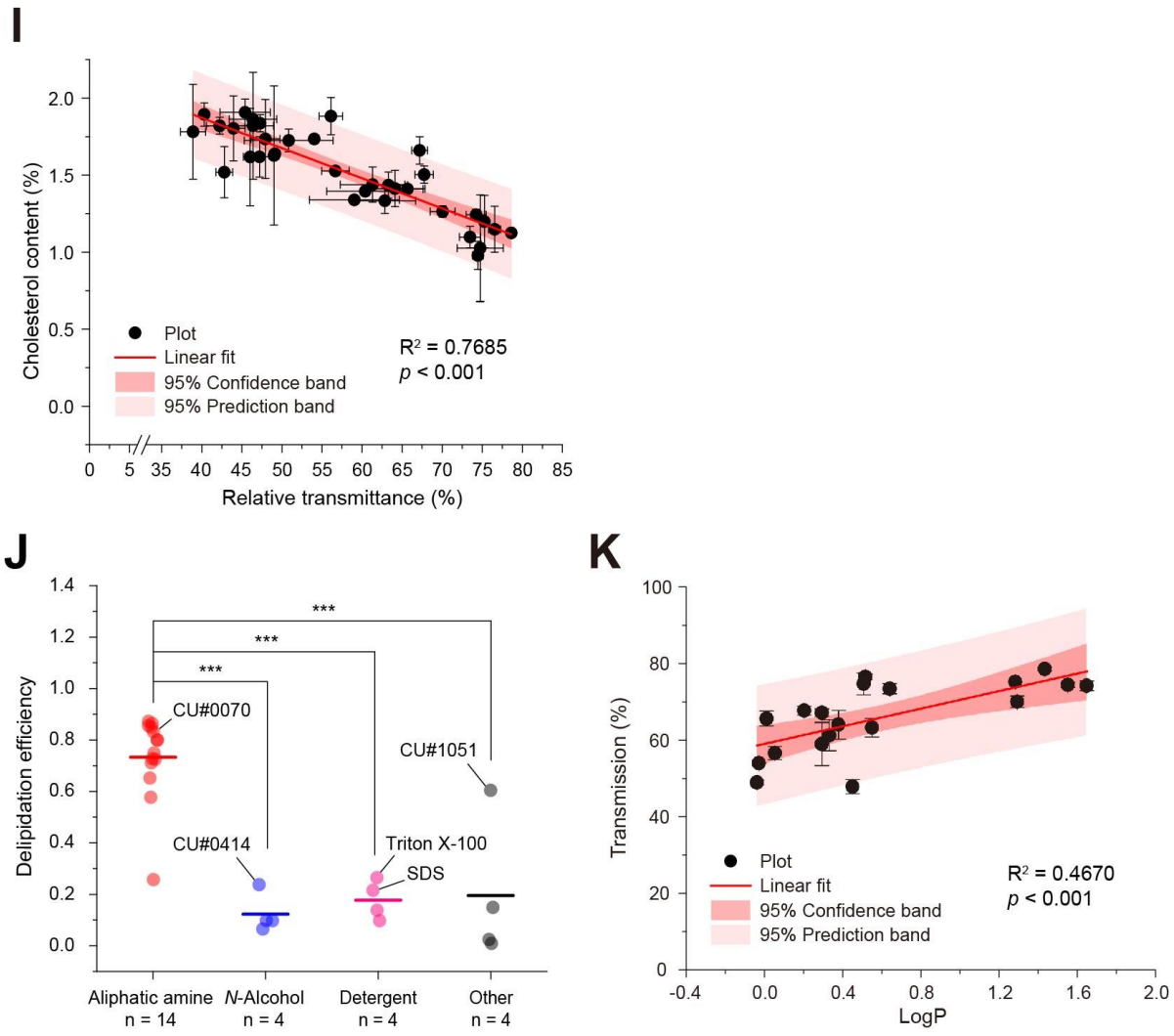

Figure 4. Comprehensive CUBIC chemical profiling of delipidation.

(A) CUBIC chemicals were divided into three groups (detergents, non-detergent and salt-free chemicals, and salts) and their lipid solubility scores were compared. (B) Relationship between the LogP of the hydrophobic group in a detergent and the lipid solubility score. A series of detergents bearing seven different kinds of polar head group (xyanthate, pyridinium, ammonium, carboxylate, sulfonate, polyether, and cholesterol) was investigated. (C) Lipid solubility scores of cationic, anionic, and non-ionic detergents. Anionic and non-ionic detergents had higher lipid solubility scores than cationic detergents. (D and E) Dependency of the lipid solubility score on the chemical functional group (D) and pH (E), compared with the alcohol group and pH 7-8, respectively. (F) The variable importance projection (VIP) scores of two major partial least squares (PLS) components for each variance. (G) Scatter plot of the LogP and lipid solubility score for water-soluble CUBIC chemicals. The LogP of less polar amines (including aliphatic amines, N-alcohols, and N-ethers with LogP ≥ −2.0) was correlated

with their lipid solubility score. (H) Scatter plot of the relative transmittance and phospholipid content of brain hemispheres of adult mice treated with highly lipid-soluble chemicals. Data are mean ± SD (n = 2). (I) Scatter plot of the relative transmittance and cholesterol content of brain hemispheres of adult mice treated with high lipid-solubilizing chemicals. Data are mean ± SD (n = 2). (J) Delipidation efficiency of the aliphatic amines, aminoalcohol (N-alcohol), detergents, and others in H. (K) Scatter plot of the relative transmittance and LogP of the amine groups. Data are mean ± SD (n = 2). Box and whisker plots show 25th–75th percentile (boxes), 10th–90th percentile (whiskers), median (horizontal lines), and mean (cross). *$p < 0.05$, **$p < 0.01$, and ***$p < 0.001$.

A

Class	Parameter	Abbreviation
Functional parameter	Alkyl chain number	$C\text{-}C_{sum}$
	Alkyl chain length between polar groups	$C\text{-}C_{length}$
	Amine group number	N_{sum}
	Hydroxyl group number	OH_{sum}
Solubility parameter	Molecular networks LogP	LogP
	Molecular networks LogS	LogS
	HSP dispersion energy	dD
	HSP polar energy	dP
	HSP hydrogen bonding energy	dH
	HSP hydrogen bonding donor energy	dHD
	HSP hydrogen bonding acceptor energy	dHA
	pH of 10 wt% solution	pH
Structural and topological parameter	Molecular weight	MWt
	Molecular volume	MVol
	Molecular density	MDens
	Polar surface area	PSA
	Connolly solvent accessible surface area (Å²)	CSASA
	Connolly molecular surface area (Å²)	CMSA
	Connolly solvent excluded volume (Å³)	CSEV
	Ovality	Ovality
	Topological diameter	Topoφ
	Balaban index	B_{index}
	Molecular topological index	MT_{index}

B

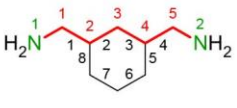

CU#0070

$C\text{-}C_{sum}$ = 8
$C\text{-}C_{length}$ = 5
N_{sum} = 2
OH_{sum} = 0

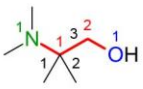

CU#0589

$C\text{-}C_{sum}$ = 3
$C\text{-}C_{length}$ = 2
N_{sum} = 1
OH_{sum} = 1

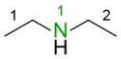

CU#0772

$C\text{-}C_{sum}$ = 2
$C\text{-}C_{length}$ = 0
N_{sum} = 1
OH_{sum} = 0

Figure 5. Parameter settings for multiple linear regression analysis.

(A) Classes and abbreviations of parameters used in the chemical analysis in this study. (B) Examples of counting functional groups.

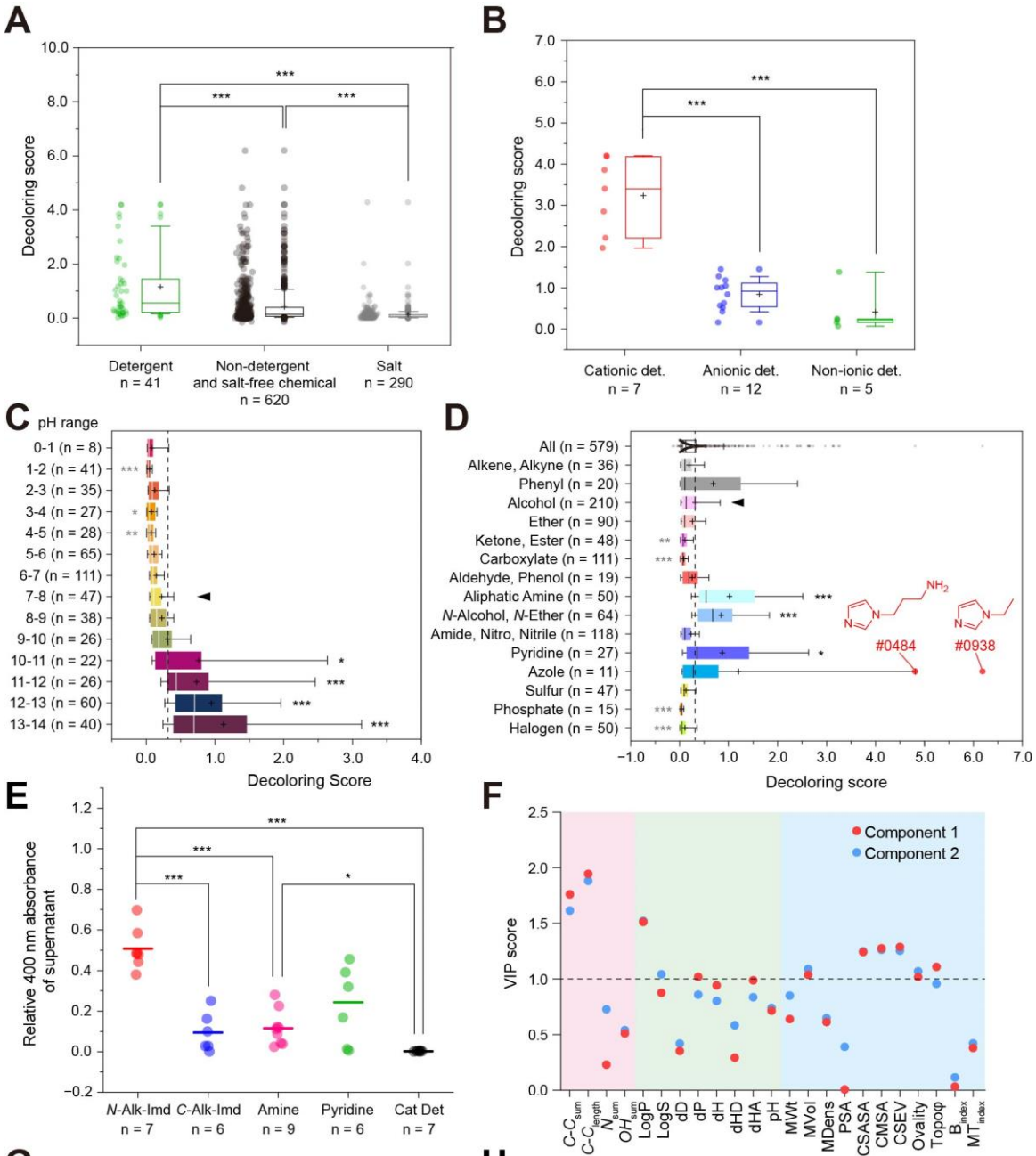
A
Decoloring score
Detergent
n = 41
Non-detergent
and salt-free chemical
n = 620
Salt
n = 290
B
Decoloring score
Cationic det.
n = 7
Anionic det.
n = 12
Non-ionic det.
n = 5
C
pH range
0-1 (n = 8)
1-2 (n = 41)
2-3 (n = 35)
3-4 (n = 27)
4-5 (n = 28)
5-6 (n = 65)
6-7 (n = 111)
7-8 (n = 47)
8-9 (n = 38)
9-10 (n = 26)
10-11 (n = 22)
11-12 (n = 26)
12-13 (n = 60)
13-14 (n = 40)
Decoloring Score
D
All (n = 579)
Alkene, Alkyne (n = 36)
Phenyl (n = 20)
Alcohol (n = 210)
Ether (n = 90)
Ketone, Ester (n = 48)
Carboxylate (n = 111)
Aldehyde, Phenol (n = 19)
Aliphatic Amine (n = 50)
N-Alcohol, N-Ether (n = 64)
Amide, Nitro, Nitrile (n = 118)
Pyridine (n = 27)
Azole (n = 11)
Sulfur (n = 47)
Phosphate (n = 15)
Halogen (n = 50)
#0484
#0938
Decoloring score
E
Relative 400 nm absorbance of supernatant
N-Alk-Imd
n = 7
C-Alk-Imd
n = 6
Amine
n = 9
Pyridine
n = 6
Cat Det
n = 7
F
Component 1
Component 2
VIP score
C-C sum
C-C length
N sum
OH sum
LogP
LogS
dD
dP
dH
dHD
dHA
pH
MWt
MVol
MDens
PSA
CSASA
CMSA
CSEV
Ovality
Topoφ
B index
MT index
G
Decoloring score
C-C length ≥ 3
n = 31
C-C length = 1-2
n = 64
C-C length = 0
n = 17
CU#0070
C-C length = 5
CU#0589
C-C length = 2
CU#0772
C-C length = 0
H
Delipidation & decolor chemical
CU#0414
N-Butyldiethanolamine
CU#0070
1,3-Bis(aminomethyl)cyclohexane
Neutral delipidation chemical
CU#1051
1,2-Hexanediol
Decolor chemical
1-Methylimidazole

Figure 6. Comprehensive CUBIC Chemical Profiling for Decoloring.

(A) CUBIC chemicals were divided into three groups (detergents, non-detergent and salt-free chemicals, and salts) and their decoloring scores were compared. (B) Decoloring scores of cationic, anionic, and non-ionic detergents. Cationic detergents showed better decoloring ability than anionic or non-ionic detergents. (C) Dependency of decoloring scores on pH compared with pH 7-8. (D) Dependency of the decoloring score on chemical functional groups compared with the alcohol group. (E) Decoloring efficiency for adult mouse spleen of N-alkylimidazole (N-Alk-Imd), C-alkylimidazole (C-Alk-Imd), amine, pyridine, and cationic detergent (Cat Det). (F) VIP scores of two major components for each variance among decoloring amines that had a high delipidation efficiency. (G) The amines were divided into three groups: multipolar amines with C-Clength ≥ 3, multipolar amines with C-Clength1-2, and single amines (C-Clength = 0). Multipolar amines with C-Clength ≥ 3 exhibited a marked decoloring ability compared to the other amines. (H) Representative chemical candidates for delipidation and/or decoloring. Box and whisker plots show 25th–75th percentile (boxes), 10th–90th percentile (whiskers), median (horizontal lines), and mean (cross). *$p < 0.05$, **$p < 0.01$, and ***$p < 0.001$.

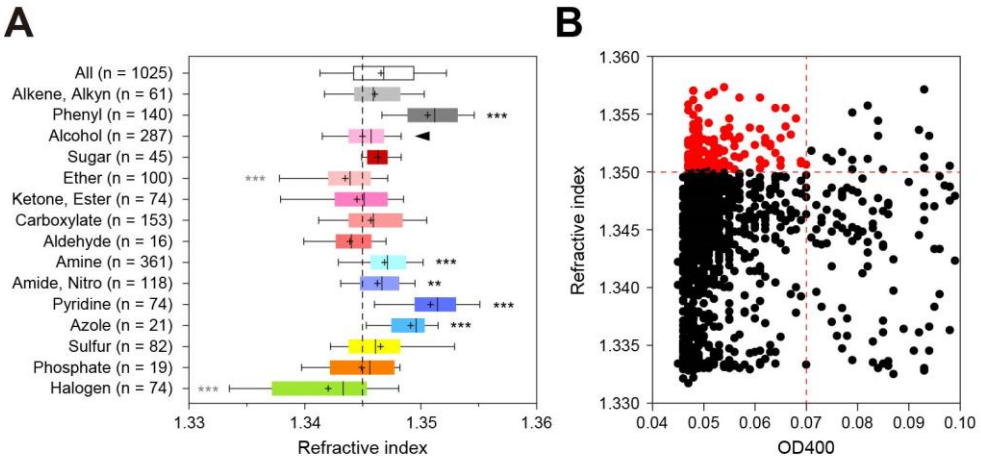
A
All (n = 1025)
Alkene, Alkyn (n = 61)
Phenyl (n = 140)
Alcohol (n = 287)
Sugar (n = 45)
Ether (n = 100)
Ketone, Ester (n = 74)
Carboxylate (n = 153)
Aldehyde (n = 16)
Amine (n = 361)
Amide, Nitro (n = 118)
Pyridine (n = 74)
Azole (n = 21)
Sulfur (n = 82)
Phosphate (n = 19)
Halogen (n = 74)
Refractive index
B
Refractive index
OD400

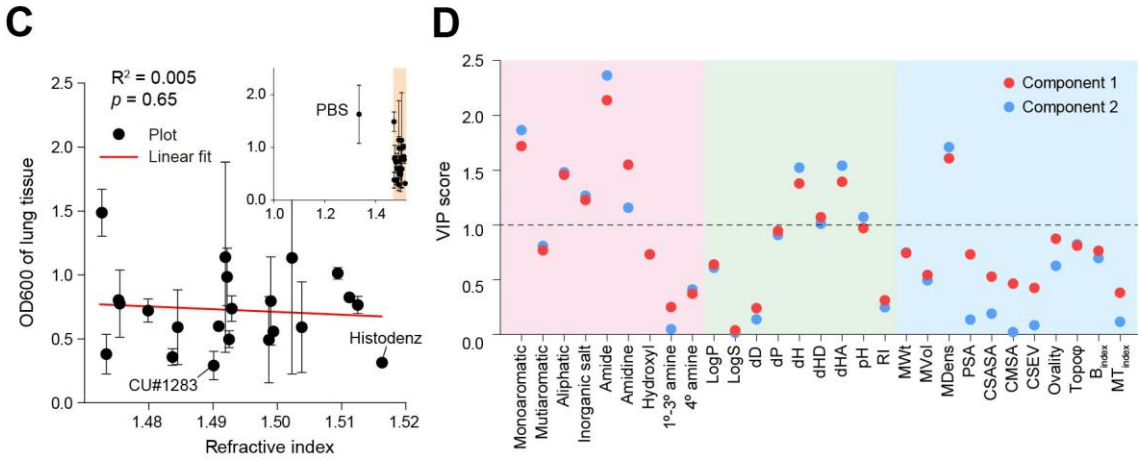
C
R² = 0.005
p = 0.65
Plot
Linear fit
PBS
OD600 of lung tissue
Refractive index
CU#1283
Histodenz
D
VIP score
Component 1
Component 2
Monoaromatic
Mutiaromatic
Aliphatic
Inorganic salt
Amide
Amidine
Hydroxyl
1°-3° amine
4° amine
LogP
LogS
dD
dP
dH
dHD
dHA
pH
RI
MWt
MVol
MDens
PSA
CSASA
CMSA
CSEV
Ovality
Topop

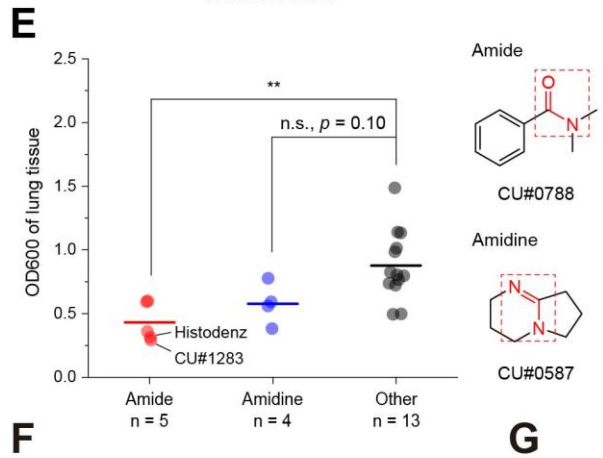
E
**
n.s., p = 0.10
OD600 of lung tissue
Histodenz
CU#1283
Amide
n = 5
Amidine
n = 4
Other
n = 13
Amide
CU#0788
Amidine
CU#0587

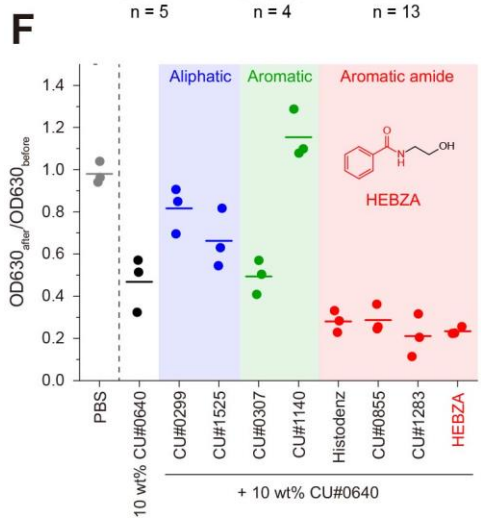
F
Aliphatic
Aromatic
Aromatic amide
HEBZA
PBS
10 wt% CU#0640
CU#0299
CU#1525
CU#0307
CU#1140
Histodenz
CU#0855
CU#1283
HEBZA
+ 10 wt% CU#0640

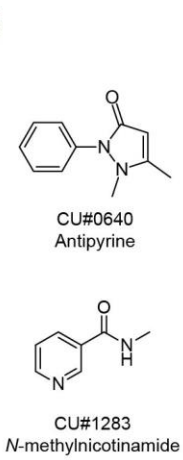
G
CU#0640
Antipyrine
CU#1283
N-methylnicotinamide

Figure 7. Comprehensive CUBIC chemical profiling of RI matching.

(A) Dependency of RI on functional groups compared with the alcohol group. (B) Scatter plot of 400-nm absorbance and RI. Less colored (OD400 < 0.07) and high RI (RI > 1.350) CUBIC chemicals were chosen for further screening. (C) Scatter plot of the RI value of concentrated solutions of 22 candidate chemicals and the OD600 of small pieces of mouse lung treated with those chemicals. Data are mean ± SD (n = 2). (D) VIP scores of two major components for each variance. (E) The 22 chemicals in C were divided into three groups: amides, amidines, and others, and the OD600 of lungs treated with these groups were compared. Amide and amidine groups are shown in red dashed boxes at right. (F) The variation in OD630 of human brain samples treated with 10/30 wt% CU#0640/RI candidates were compared. The 8 chemicals were divided into three groups: aliphatic compounds, aromatic compounds, and aromatic amides. "HEBZA" indicates N-(2-hydroxyethyl)benzamide. We used 10 wt% CU#0640-based cocktails due to the low water-solubility of HEBZA. (G) Chemical candidates for high RI matching medium. Box and whisker plots show 25th–75th percentile (boxes), 10th–90th percentile (whiskers), median (horizontal lines), and mean (cross). *$p < 0.05$, **$p < 0.01$, and ***$p < 0.001$.

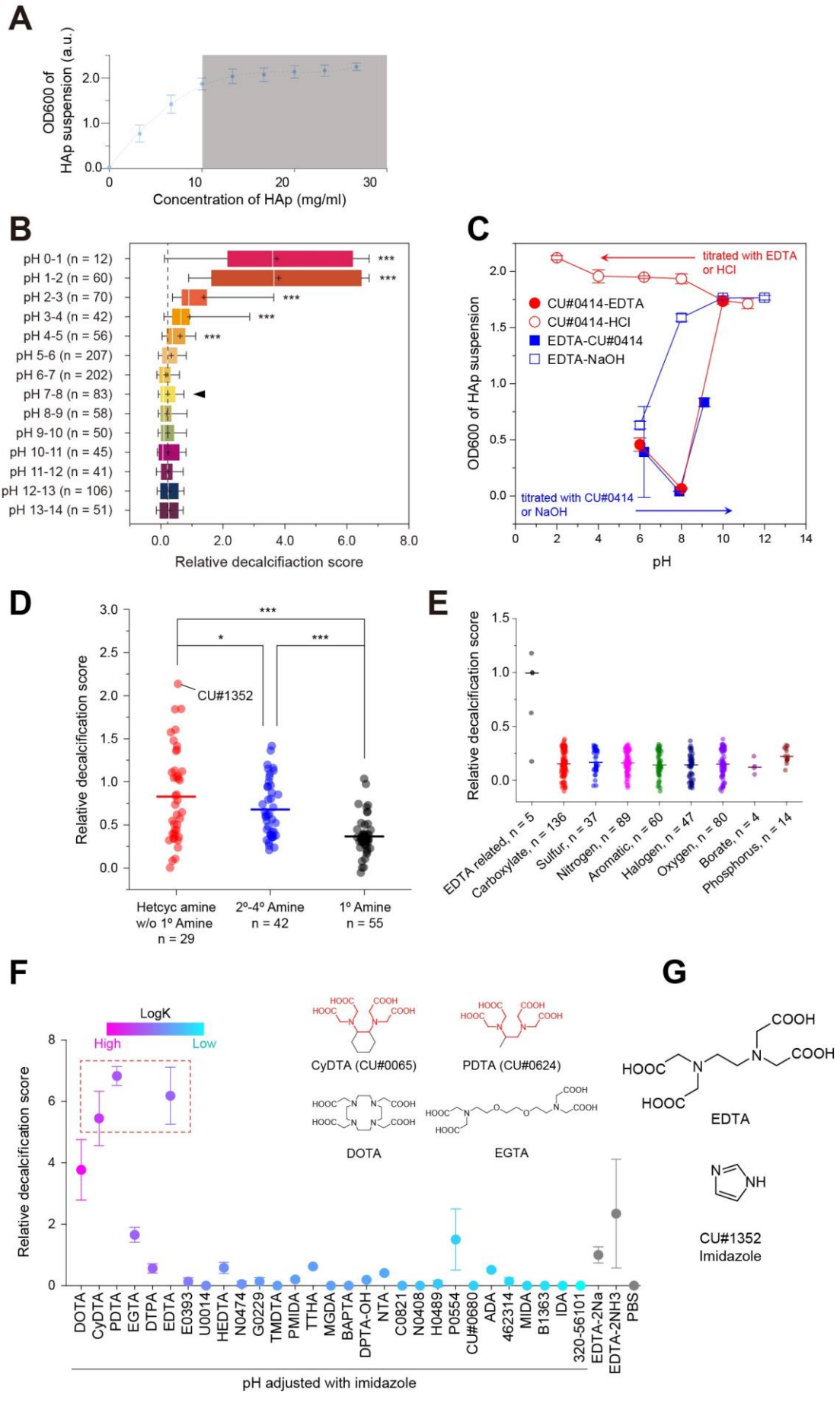
A
OD600 of HAp suspension (a.u.)
Concentration of HAp (mg/ml)
B
pH 0-1 (n = 12)
pH 1-2 (n = 60)
pH 2-3 (n = 70)
pH 3-4 (n = 42)
pH 4-5 (n = 56)
pH 5-6 (n = 207)
pH 6-7 (n = 202)
pH 7-8 (n = 83)
pH 8-9 (n = 58)
pH 9-10 (n = 50)
pH 10-11 (n = 45)
pH 11-12 (n = 41)
pH 12-13 (n = 106)
pH 13-14 (n = 51)
Relative decalcifiaction score
C
titrated with EDTA or HCl
CU#0414-EDTA
CU#0414-HCl
EDTA-CU#0414
EDTA-NaOH
titrated with CU#0414 or NaOH
OD600 of HAp suspension
pH
D
CU#1352
Relative decalcification score
Hetcyc amine w/o 1° Amine n = 29
2°-4° Amine n = 42
1° Amine n = 55
E
Relative decalcification score
EDTA related, n = 5
Carboxylate, n = 136
Sulfur, n = 37
Nitrogen, n = 89
Aromatic, n = 60
Halogen, n = 47
Oxygen, n = 80
Borate, n = 4
Phosphorus, n = 14
F
LogK
High
Low
Relative decalcification score
CyDTA (CU#0065)
PDTA (CU#0624)
DOTA
EGTA
DOTA
CyDTA
PDTA
EGTA
DTPA
EDTA
E0393
U0014
HEDTA
N0474
G0229
TMDTA
PMIDA
TTHA
MGDA
BAPTA
DPTA-OH
NTA
C0821
N0408
H0489
P0554
CU#0680
ADA
462314
MIDA
B1363
IDA
320-56101
EDTA-2Na
EDTA-2NH3
PBS
pH adjusted with imidazole
G
EDTA
CU#1352
Imidazole

Figure 8. Comprehensive CUBIC chemical profiling of decalcification.

(A) Quantitativeness of the HAp-based screening system in **Figure 2E**. OD600 of the HAp suspension increased linearly as the HAp concentration was raised from 0 to 10 mg/ml. Data are mean ± SD (n = 4). (B) Dependency of relative decalcification score on pH compared with pH 7-8. (C) pH dependence of OD600 of chemically treated HAp suspension. Data are mean ± SD (n = 3). CU#0414 10 wt% titrated with EDTA or HCl, and EDTA 10 wt% titrated with CU#0414 or NaOH were used. (D) Relative decalcification scores of EDTA-based cocktails (pH 7-8) neutralized with various counter-bases including heterocyclic amines without primary amine (Hetcyc amine w/o 1 °amine), secondary and tertiary amines and quaternary ammoniums (2 °-4 ° amine), and other amines including primary amine (1 ° amine). (E) Relative decalcification scores of chemical cocktails containing various kinds of acids listed in the CUBIC chemical library. All of the acids were neutralized with CU#0414 (pH 7-8). Over 200 acids bearing various kinds of functional groups were tested. In this analysis, we compared the tested acids except for EDTA-related chemicals according to their functional group. (F) Relative decalcification score of EDTA derivatives. Data are mean ± SD (n = 3). Chemicals are presented in descending order of LogK. Chemical ID is a typical abbreviation or vendor catalog number. The top 3 chemicals shared a common EDTA structure (red). (G) Chemical candidates for decalcification cocktails consisting of EDTA and imidazole (CU#1352). Box and whisker plots show 25th–75th percentile (boxes), 10th–90th percentile (whiskers), median (horizontal lines), and mean (cross). *$p < 0.05$, **$p < 0.01$, and ***$p < 0.001$.

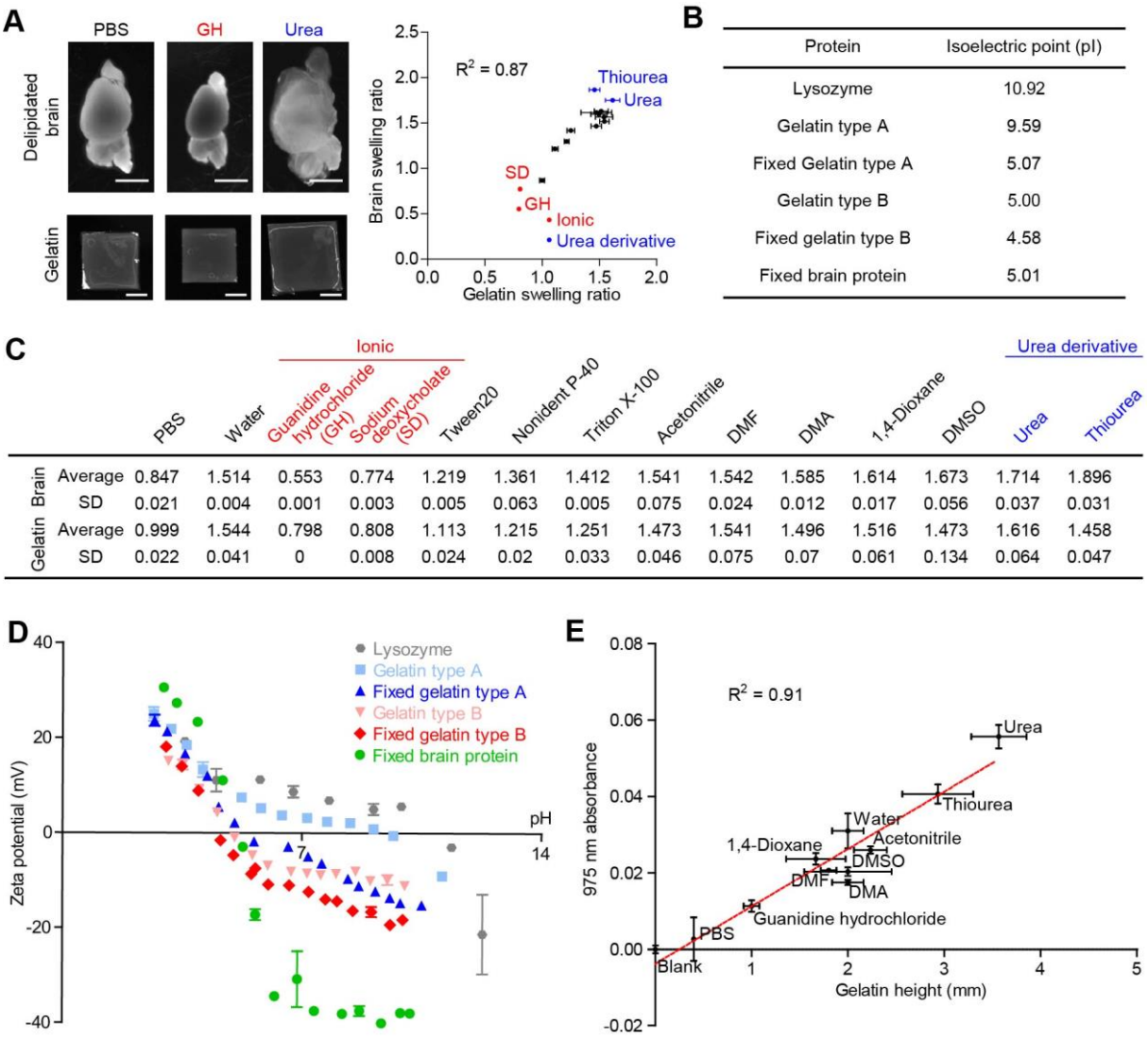

Figure 9. Development of gelatin-based high-throughput screening assay.

(A) Correlation of the swelling ratio between delipidated hemisphere brains (n = 2) and post-fixed type B gelatins (n = 3) treated with PBS, water, or 12 chemicals. 12 chemicals were chosen from our previous study (Susaki et al., 2014). GH: guanidine hydrochloride, SD: sodium deoxycholate, respectively. R-squared value was calculated with all individual data plots. Scale bars, 5 mm. (B) Isoelectric points (pIs) of lysozyme, type A gelatin, type B gelatin, and extracted brain protein. "Fixed" indicates fixation by paraformaldehyde (PFA). (C) The swelling ratio (the average and SD) of chemically treated brain samples and gelatin gel between before and after chemical treatment shown in **Figure 9A** (brain; n = 2, gelatin; n = 3). All chemicals are chosen from our previous study. Urea derivatives (blue color) remarkably swelled brain samples compared to ionic chemicals (red color). (D) The plots of zeta potential against pH for various protein samples. Each zeta potential curve was fitted to fourth-order

polynomials. The isoelectric points were determined by calculating crossing points of polynomials with the x-axis. The measurements were repeated three times at each pH point. (E) Correlation of the 975 nm absorbance and apparent height of type B gelatin (n = 3) treated with PBS, water, or 8 other chemicals indicated in the panel. The 975 nm absorbance of chemically treated gelatin gels showed a linear correlation with the apparent height of those. R-squared value was calculated with all data plots. All values are mean ± SD.

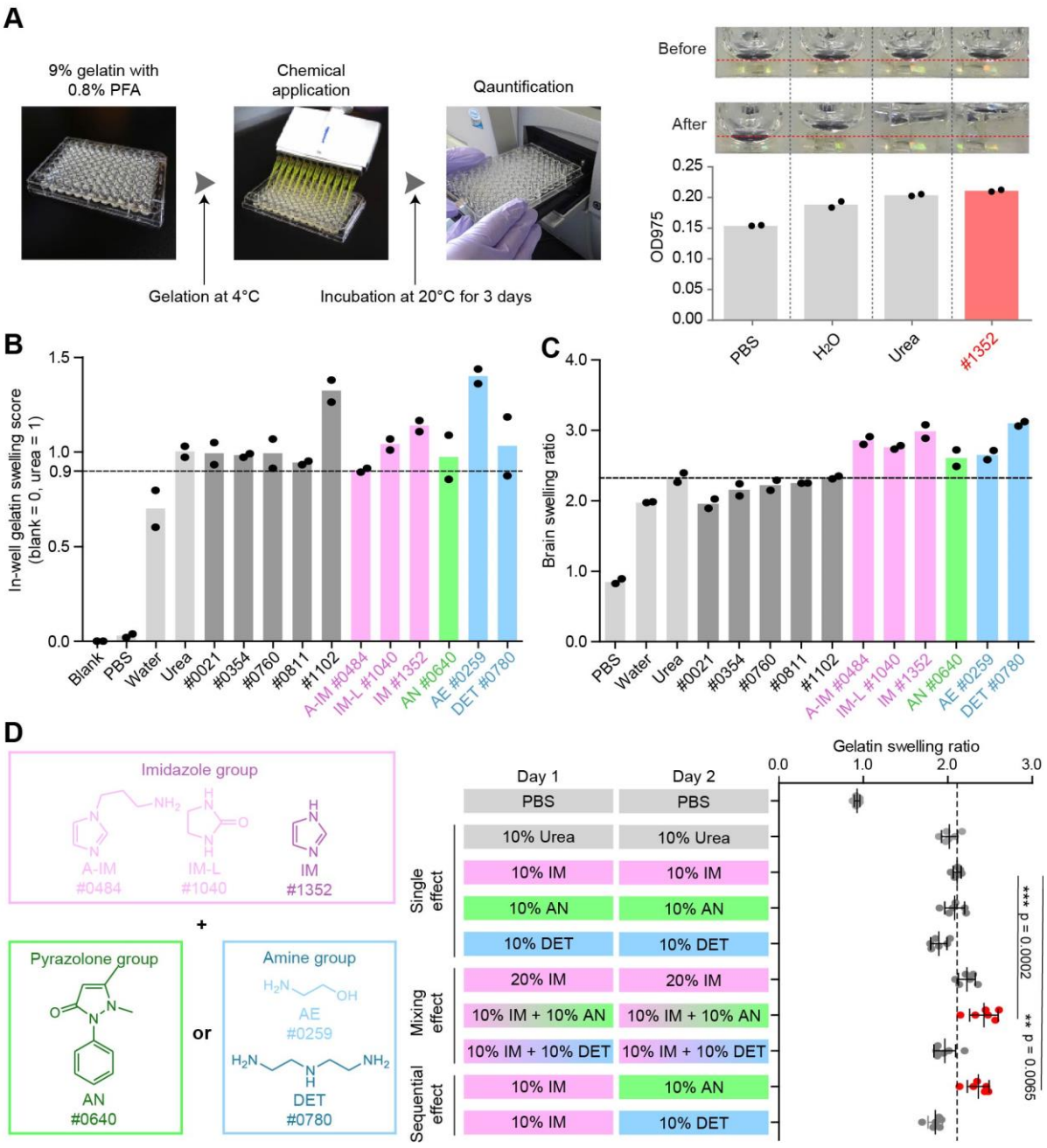

Figure 10. Identification of novel swelling reagents by comprehensive chemical screening.

(A) Procedure of the chemical screening for swelling reagents from a 1,691 chemical library. Indicated number (e.g. #1352) is each chemical ID. Each bar indicates the mean value. (B) In-well gelatin gel-based 1st chemical screening (n = 2) identified 11 chemicals which had a relative swelling score greater than 0.9 as a criterion. I highlighted several chemical groups; imidazole (pink), pyrazolone (green), amine (blue). Each bar indicates the mean value. (C) Hemisphere brain-based 2nd chemical screening (n = 2) identified final 6 chemical candidates. I highlighted several chemical groups as B. Each bar indicates the mean value. (D) I classified

6 chemical candidates into three groups based on their chemical structure; imidazole (pink), pyrazolone (green), amine (blue). I evaluated potential additive swelling effects such as solvent-mixing effect and solvent-substitution effect by gelatin gel-based assay. (***$p < 0.001$, **$p < 0.01$, one-way ANOVA, Tukey's post hoc test for multiple comparisons $n = 6$). All values are mean ± SD.

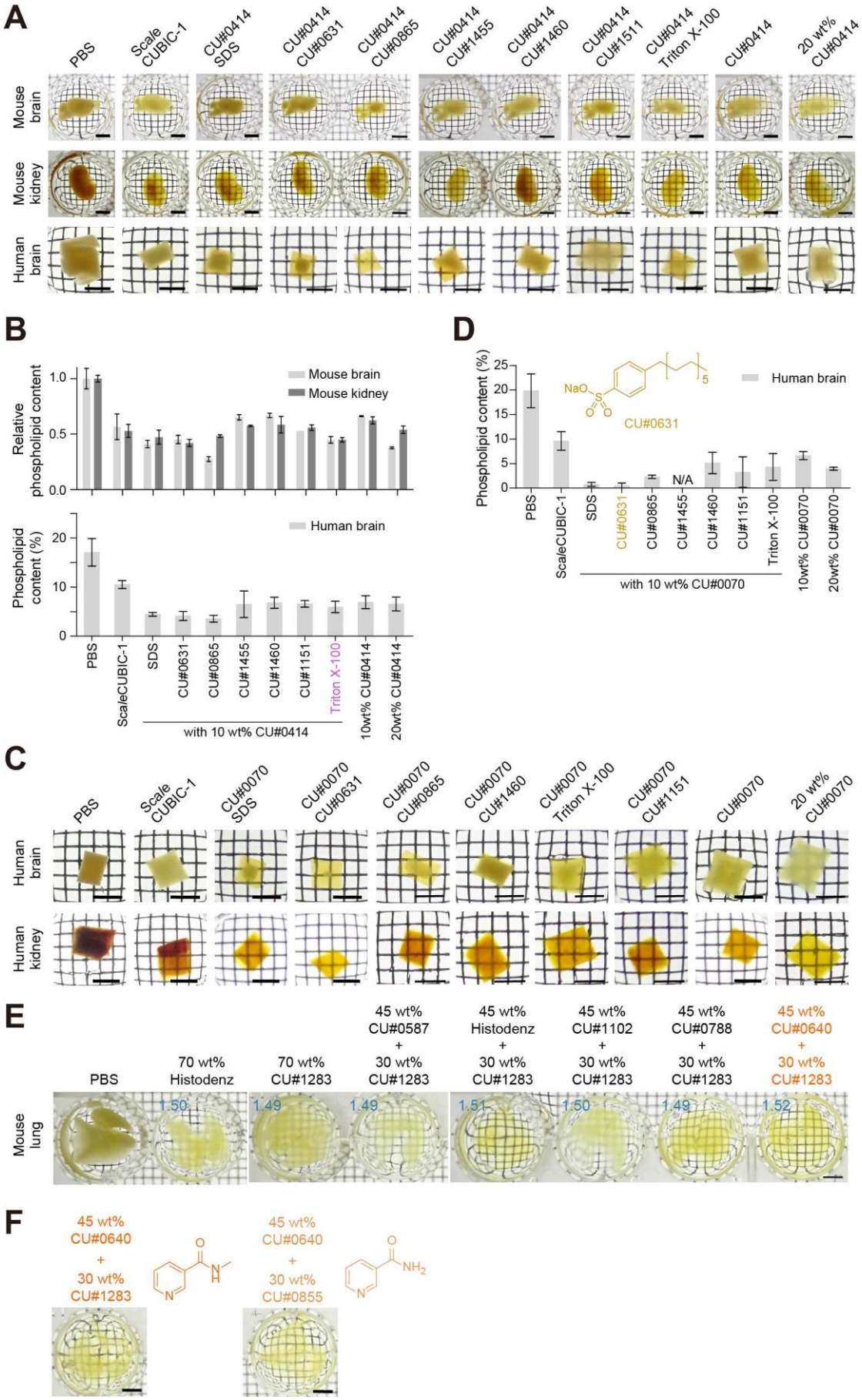
A
PBS
Scale CUBIC-1
CU#0414 SDS
CU#0414 CU#0631
CU#0414 CU#0865
CU#0414 CU#1455
CU#0414 CU#1460
CU#0414 CU#1511
CU#0414 Triton X-100
CU#0414
20 wt% CU#0414
Mouse brain
Mouse kidney
Human brain
B
Relative phospholipid content
Mouse brain
Mouse kidney
Phospholipid content (%)
Human brain
PBS
Scale/CUBIC-1
SDS
CU#0631
CU#0865
CU#1455
CU#1460
CU#1151
Triton X-100
10wt% CU#0414
20wt% CU#0414
with 10 wt% CU#0414
D
Phospholipid content (%)
Human brain
NaO
CU#0631
N/A
PBS
Scale/CUBIC-1
SDS
CU#0631
CU#0865
CU#1455
CU#1460
CU#1151
Triton X-100
10wt% CU#0070
20wt% CU#0070
with 10 wt% CU#0070
C
PBS
Scale CUBIC-1
CU#0070 SDS
CU#0070 CU#0631
CU#0070 CU#0865
CU#0070 CU#1460
CU#0070 Triton X-100
CU#0070 CU#1151
CU#0070
20 wt% CU#0070
Human brain
Human kidney
E
PBS
70 wt% Histodenz
70 wt% CU#1283
45 wt% CU#0587 + 30 wt% CU#1283
45 wt% Histodenz + 30 wt% CU#1283
45 wt% CU#1102 + 30 wt% CU#1283
45 wt% CU#0788 + 30 wt% CU#1283
45 wt% CU#0640 + 30 wt% CU#1283
Mouse lung
1.50
1.49
1.49
1.51
1.50
1.49
1.52
F
45 wt% CU#0640 + 30 wt% CU#1283
45 wt% CU#0640 + 30 wt% CU#0855

Figure 11. Combinatorial screening of CUBIC chemicals.

(A) Combinatorial screening of delipidation chemicals compatible with FP. CU#0414 was mixed with various detergents. Mouse brain hemispheres, kidneys, and human brain blocks were delipidated with individual chemical cocktails, and then immersed in CUBIC-R. (B) Phospholipid content of the tested biological tissues treated with CU#0414-based delipidation cocktails (n = 3). (C) Combinatorial screening of delipidation chemicals for human brain and kidney blocks. CU#0070 was mixed with various detergents. (D) Phospholipid content of human brain blocks treated with CU#0070-based delipidation cocktails. The CU#0070-CU#1455 cocktail precipitated (n = 3). (E) Combinatorial screening of RI matching reagents. Delipidated adult (8-week-old) mouse lungs were immersed in highly concentrated chemical cocktails. RI of the mixtures is shown in blue. (F) RI matching performance of the CUBIC-RA cocktail of CU#0640 and CU#1283, and the CUBIC-R cocktail of CU#0640 and CU#0855. Adult (8-week-old) mouse lungs were delipidated and then treated with CUBIC-RA or CUBIC-R. Similar clearing performances were observed. Scale bars indicate 4 mm. Data are mean ± SD.

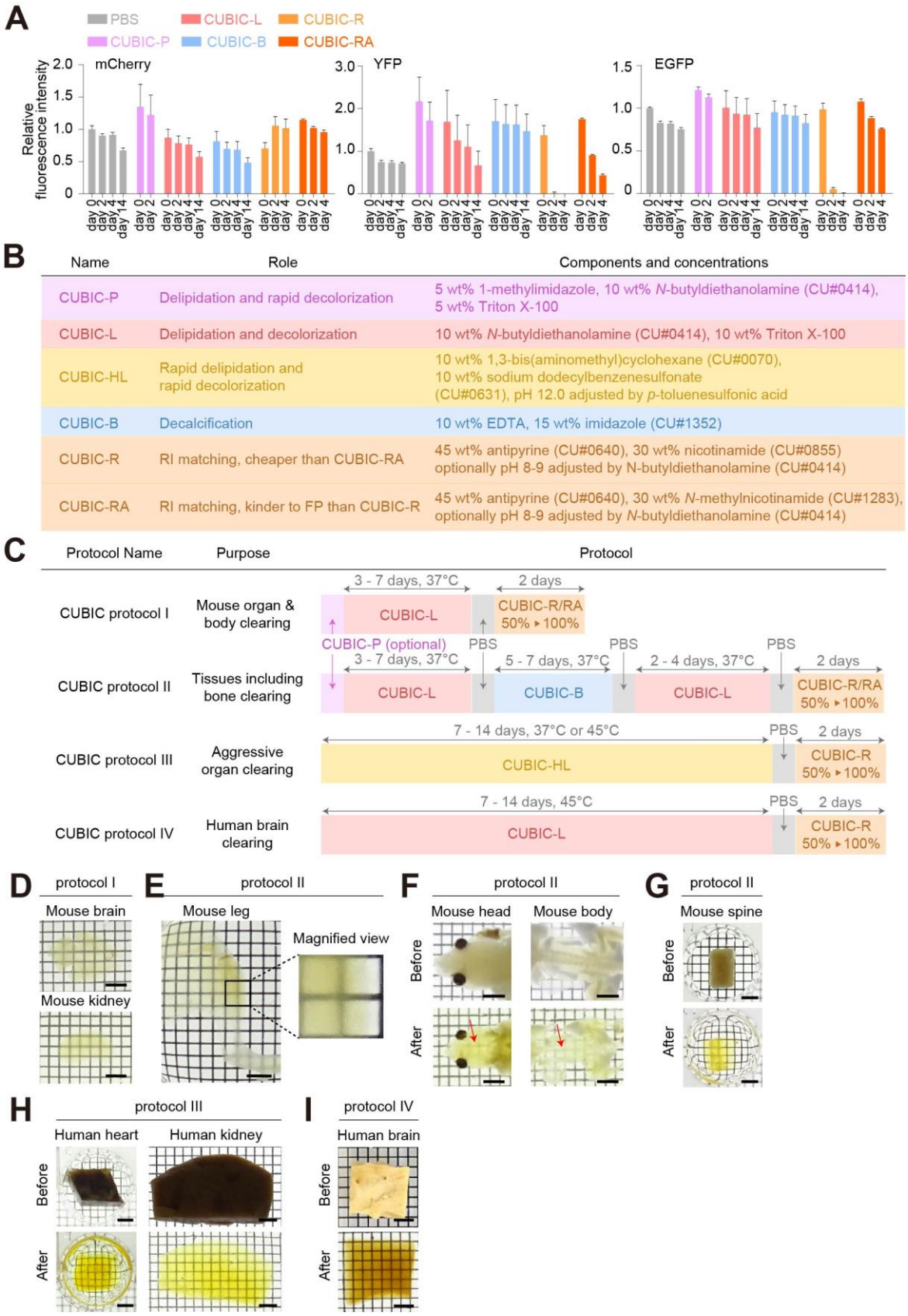

Figure 12. Rapid and scalable tissue-clearing CUBIC protocols.

(A) Time course of fluorescent signals from fluorescent proteins with each CUBIC cocktail (n = 3). (B and C) Chemical components in CUBIC cocktails (B), and CUBIC protocols using serial treatments with CUBIC cocktails (C). (D) Clearing performance of CUBIC protocol I for adult (6-week-old) mouse brain and kidney. (E-G) Clearing performance of CUBIC protocol II for adult (8-week-old) mouse leg (E), P7 mouse head and body (F), and adult (8-week-old) mouse spinal cord (L4-6) (G). Grids were visible through hard bone tissue (red arrows). (H) Clearing performance of CUBIC protocol III for human heart and kidney blocks. (I) Clearing performance of CUBIC protocol IV for human brain block. Scale bars indicate 4 mm. Data are mean ± SD.

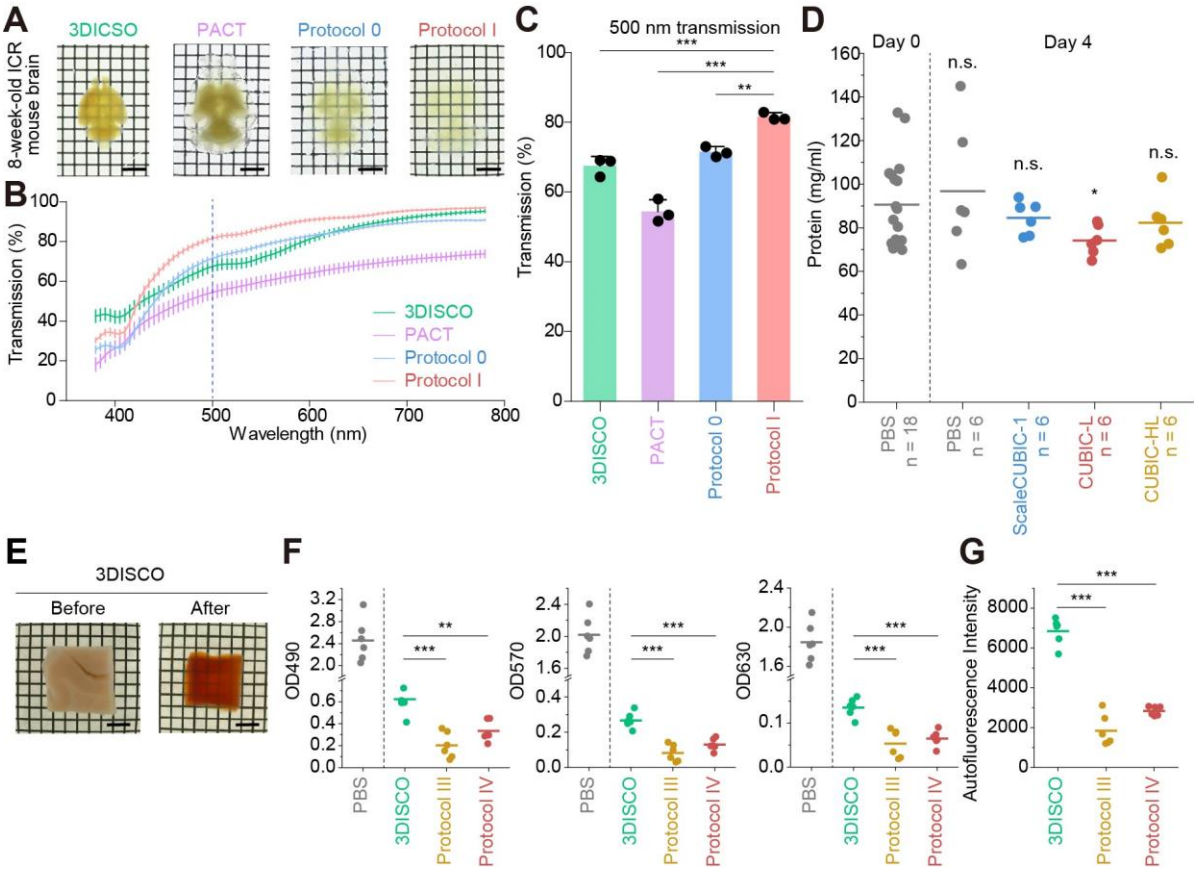

Figure 13. Comparison among tissue clearing protocols.

(A-C) Comparison of clearing protocols. 3DISCO, PACT, CUBIC protocol 0, and CUBIC protocol I were compared. Adult (8-week-old) mice were used. White-background transmission images (A) and quantified transmission (B and C) are shown. Data are mean ± SD (n = 3). Transmission spectrum (B) and transmission of the 500-nm wavelength in B (C) are shown. (D) Quantification of the protein content of human brain tissue after delipidation. Mean are shown. (E) Clearing performance of 3DISCO for human brain block. Scale bars indicate 4 mm. (F) Absorbance at 490 nm, 570 nm, and 630 nm after the clearing protocols for human brain samples (n = 6). (G) Autofluorescence intensity of human brain samples after the clearing protocols (n = 6). Mean are shown. Scale bars indicate 4 mm. **p < 0.01 and ***p < 0.001.

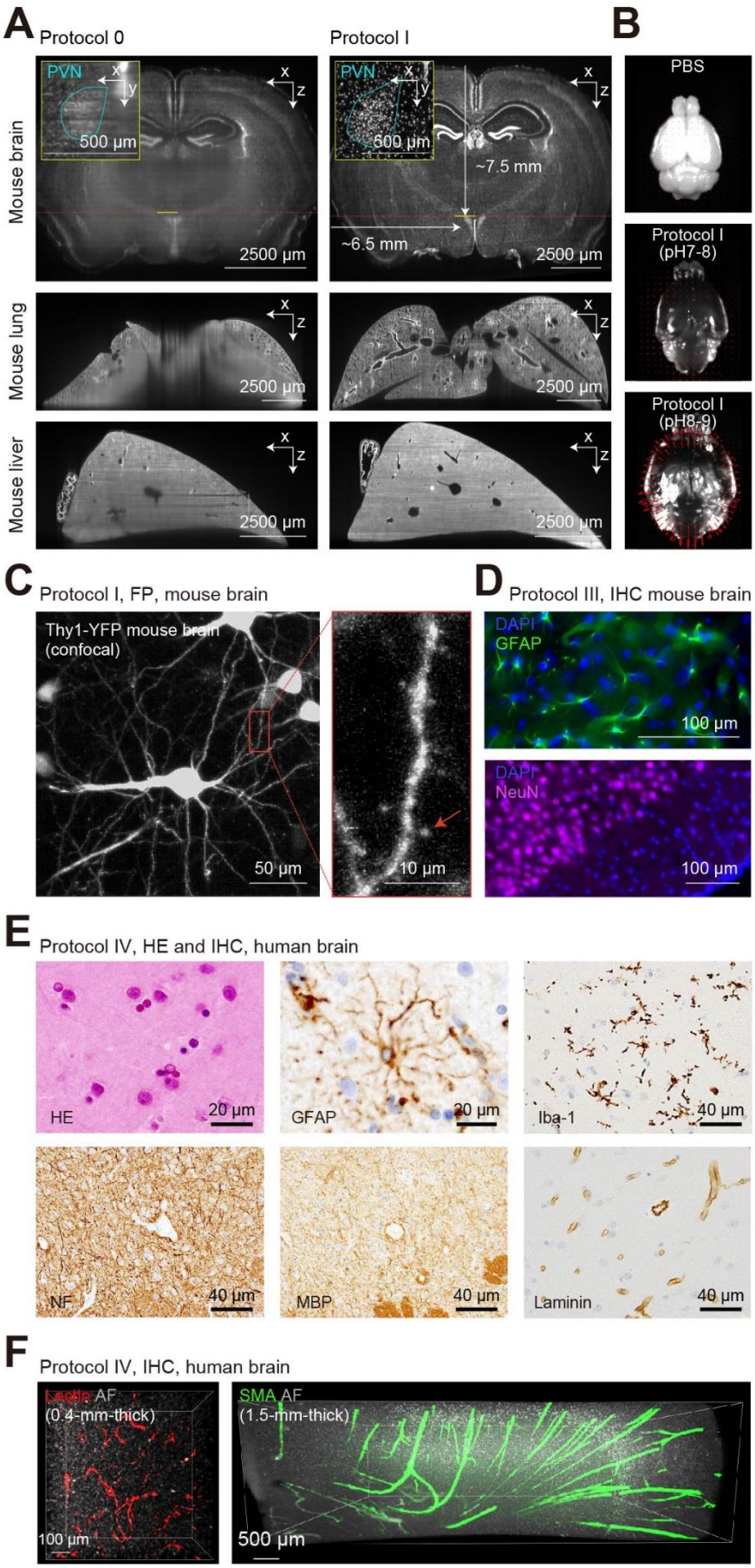
A
Protocol 0
Protocol I
B
PBS
Protocol I (pH7-8)
Protocol I (pH8-9)
Mouse brain
Mouse lung
Mouse liver
PVN
500 μm
2500 μm
~7.5 mm
~6.5 mm
C
Protocol I, FP, mouse brain
Thy1-YFP mouse brain (confocal)
50 μm
10 μm
D
Protocol III, IHC mouse brain
DAPI
GFAP
100 μm
DAPI
NeuN
100 μm
E
Protocol IV, HE and IHC, human brain
HE
20 μm
GFAP
20 μm
Iba-1
40 μm
NF
40 μm
MBP
40 μm
Laminin
40 μm
F
Protocol IV, IHC, human brain
Lectin AF
(0.4-mm-thick)
100 μm
SMA AF
(1.5-mm-thick)
500 μm

Figure 14. Tissue integrity of CUBIC-treated organs.

(A) LSFM images of nucleus-stained 8-week-old brain, lung, and left medial lobe of the liver after CUBIC protocol 0 and CUBIC protocol I. To compare the image qualities fairly, imaging was performed only from one side of the tissue. x indicates the illumination direction and z indicates the detection direction of the LSFM. For brain, the hypothalamic nuclei of paraventricular nuclei (PVN) are visualized in the insets. The scales for CUBIC protocols 0 and I were slightly adjusted to correct for shrinkage caused by CUBIC protocol 0. (B) Deformation analysis of cleared 8-week-old mouse brains using CUBIC protocol I. The cleared brains were registered to a standard brain, and then the deformation fields were visualized on the projection images of the brains. In the RI-matching step, neutral CUBIC-R (without #0414; middle) and basic CUBIC-R (pH 8-9 adjusted with CU#0414; bottom) were applied. (C) Subcellular imaging of a 6-month-old Thy1-YFP mouse brain after CUBIC protocol I. A cellular view (left) and magnified view (right) are shown. A representative spine is indicated by a red arrow (right). (D) Immunohistochemistry of an 8-week-old mouse brain after a 4-day CUBIC-HL treatment. Anti-GFAP (top) and anti-NeuN (bottom) antibodies were used. (E) Hematoxylin-Eosin (HE) staining (left top) and immunohistochemistry of human brain after protocol IV. Antibodies for glial fibrillary acidic protein (GFAP), ionized calcium-binding adapter molecule 1 (Iba-1), neurofilament (NF), myelin basic protein (MBP), and laminin were examined. (F) Visualization of vascular structures in thick slices of a human brain. Lectin (for 0.4-mm-thick brain slice; left) and anti-α-SMA antibody (for 1.5-mm-thick slice; right) were applied. The 3D volumetric images were obtained with LSFM.

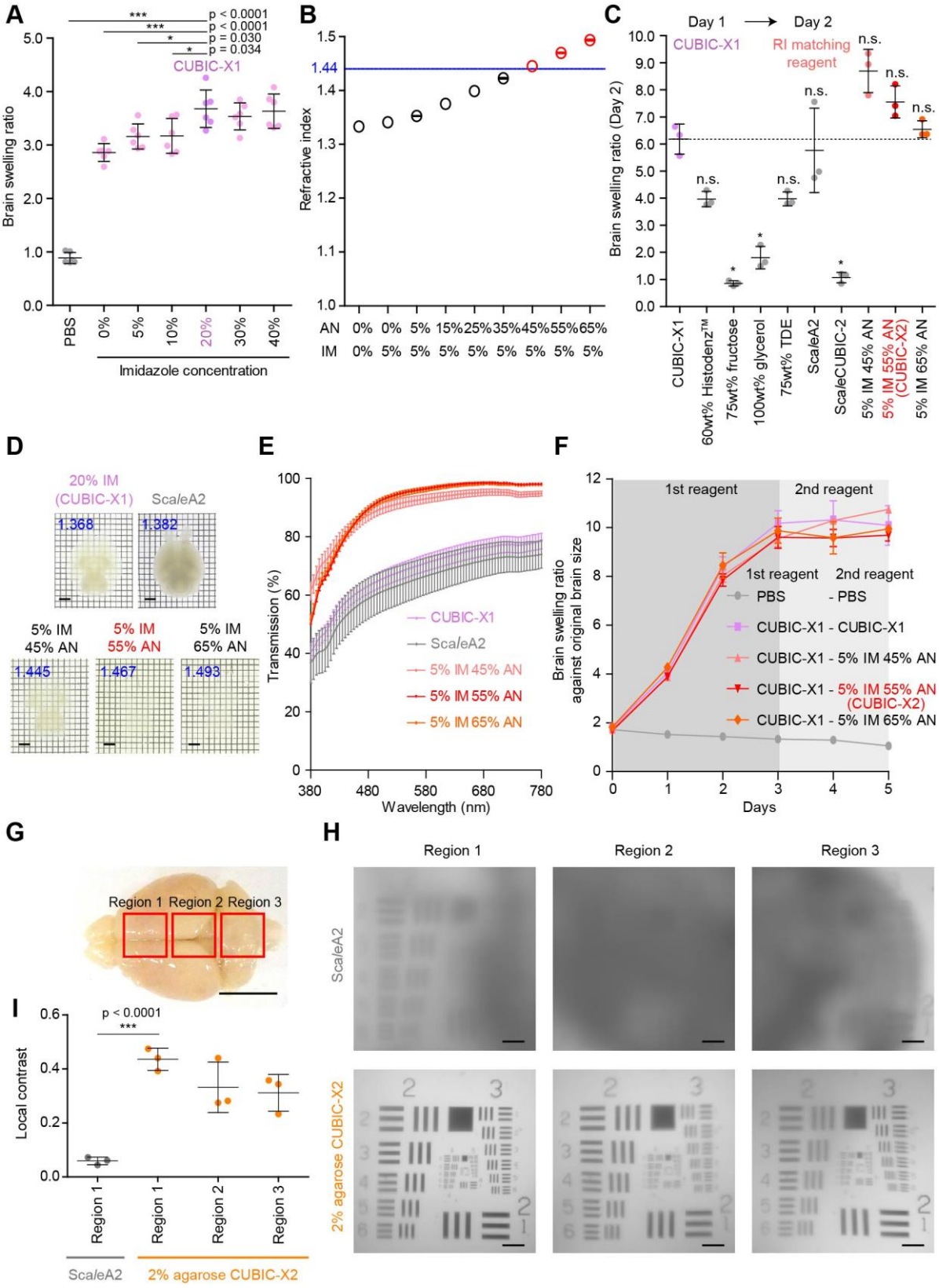

Figure 15. CUBIC-X1 and CUBIC-X2 for whole-brain expansion and hyperhydrative RI matching.

(A) Swelling ratios of delipidated hemisphere brains treated by imidazole aqueous solutions for 1 day. Delipidated hemisphere brains were immersed in various concentration of imidazole aqueous solutions (n = 6). The 20% imidazole solution, termed CUBIC-X1, was the minimal concentration to achieve the largest expansion volume (***$p < 0.001$, *$p < 0.05$, one-way ANOVA, Tukey's post hoc test for multiple comparisons). (B) Refractive indices of cocktails of imidazole and antipyrine (n = 3). I note that the standard error of several points cannot be shown because those measured values rounded at third decimal place resulted in the identical values. (C) Swelling ratios of hemisphere brains by RI matching media. Delipidated hemisphere brains were treated with CUBIC-X1 for 1 day, and then immersed in various kinds of RI media for 1 day (n = 3, *$p < 0.05$, Dunnett's Modified Tukey-Kramer pairwise multiple comparison test). (D) Transmission images of CUBIC-X1-treated whole brains after additional treatment with CUBIC-X1, Sca*l*eA2, and imidazole/antipyrine cocktails. Chemical cocktails of 5% imidazole and 45-65% antipyrine provided almost full transparent brains without shrinkage. RIs of each chemical are shown in blue. Scale bars indicate 2 mm. (E) Transmission curves of whole brain samples shown in D. Light transmittance around the visible region (380-780 nm) was measured (n = 3). (F) Time course of brain swelling ratio of delipidated whole brains after chemical treatment (n = 3). Brain swelling ratio was evaluated against original brain size. In view of handling, I chose 5%/55% imidazole/antipyrine cocktail (termed as CUBIC-X2). (G) Three regions of the brain quantified in H. (H) Sca*l*eA2 and CUBIC-X2 treated CUBIC-X1 expanded brains were placed on USAF chart for quantitative analysis of scattering. The CUBIC-X2 brains were embedded in 2% agarose. (I) Comparison of the local contrasts of the Sca*l*eA2 and CUBIC-X2 treated CUBIC-X1 expanded brains. The local contrasts were quantified by referring local intensity profiles over element 2, group 2 of USAF chart (n = 3, ***$p < 0.001$, independent two-tailed t-test). All values are mean ± SD. Scale bars indicate 4 mm (D) 5 mm (G) and 500 μm (H).

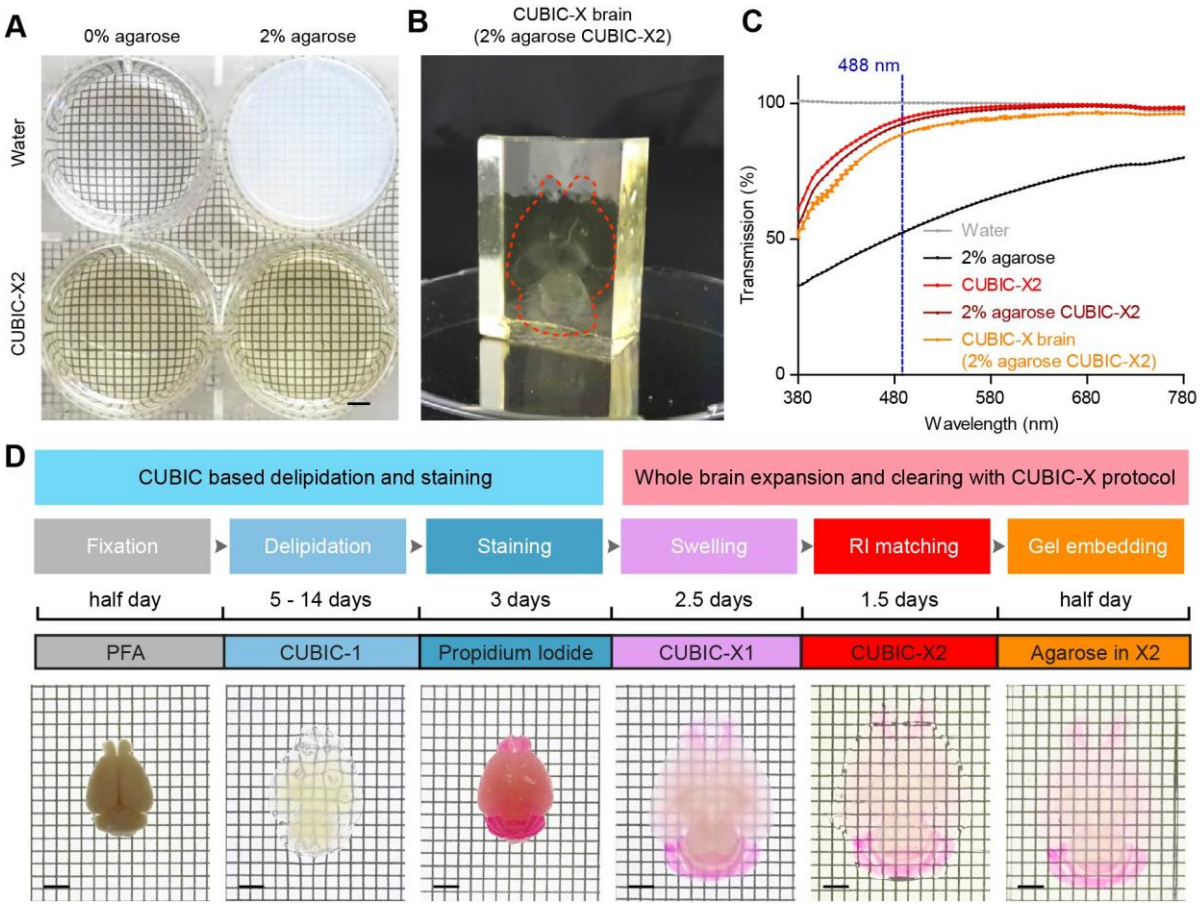

Figure 16. CUBIC-X for whole-brain expansion and hyperhydrative RI matching.

(A) Transmission images of water, CUBIC-X2, 2% agarose, and 2% agarose CUBIC-X2. 2% agarose CUBIC-X2 showed high transparency while 2% agarose showed white turbidity. (B) Image of a CUBIC-X brain (2% agarose CUBIC-X2). The gel embedded expanded brain was highly transparent and solid enough to mount on the LSFM. (C) Transmission curves of water, CUBIC-X2, 2% agarose, 2% agarose CUBIC-X2, and CUBIC-X brain (2% agarose CUBIC-X2). Light transmittance around the visible region (380-780 nm) was measured (n = 3). (D) Overview of a whole-brain expansion and hyperhydrative RI matching protocol (a CUBIC-X protocol) with staining of nuclei. The duration of CUBIC-1 delipidation could be modified depending on the purpose. Scale bars indicate 2 mm

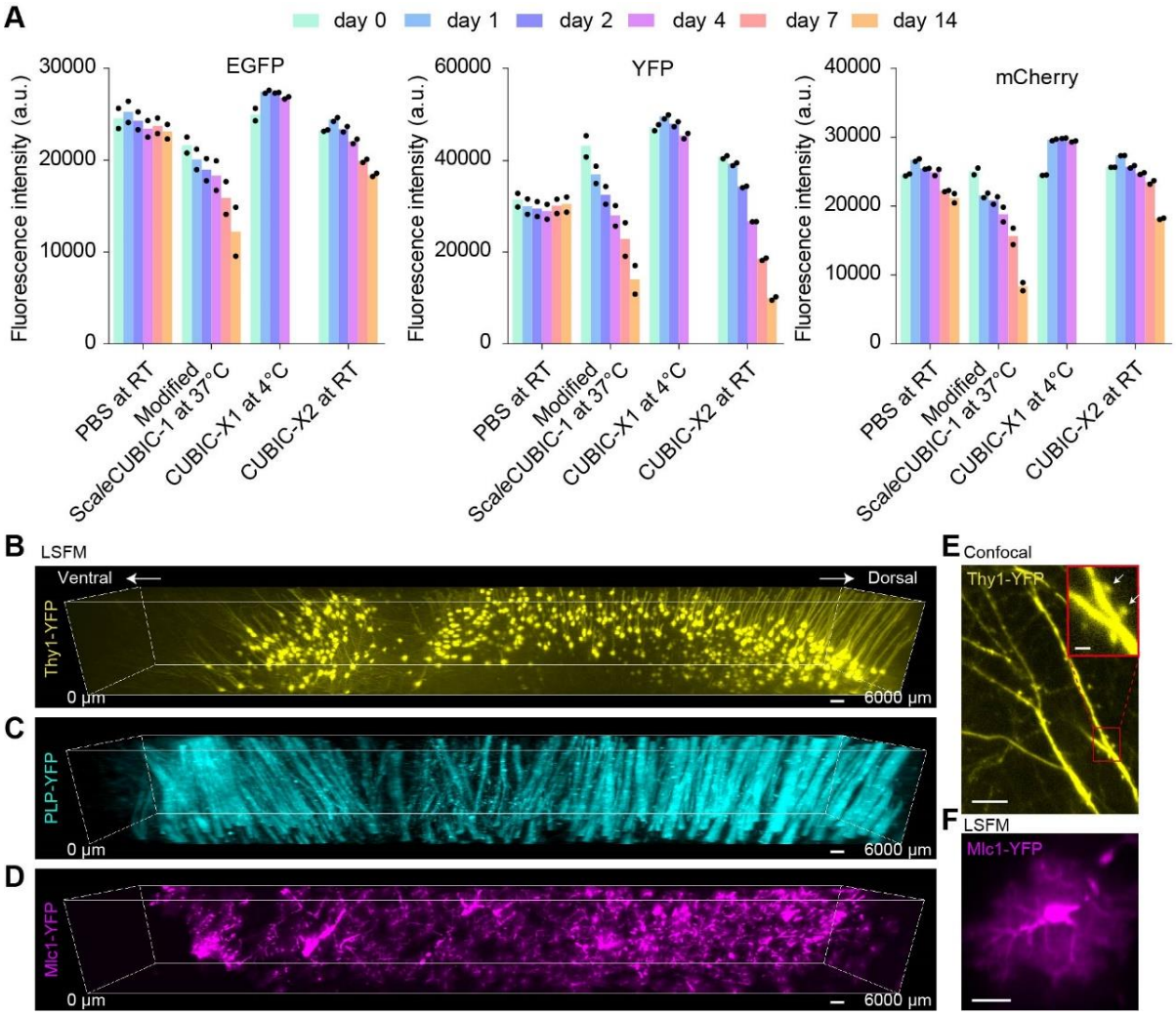

Figure 17. Fluorescent proteins in CUBIC-X.

(A) Quenching test of fluorescent proteins by several CUBIC reagents. The indicated recombinant fluorescent proteins were incubated in each reagent or PBS for up to two weeks. The bars indicate the averages (n = 2). (B-D) CUBIC-X was compatible with fluorescent protein imaging of various reporter mouse brains. Thy1-YFP, PLP-YFP and Mlc1-YFP mouse brains were cleared and expanded with CUBIC-X protocol, and imaged with LSFM (10×, NA = 0.6). The volume rendered images are visualized. Scale bars indicate 100 µm. (E) Confocal image (25×, NA =1.0) of Thy1-YFP mouse brain. Inset: Magnified view showing spines (indicated by arrows). Scale bars indicate 30 µm (main) and 5 µm (inset). (F) A LSFM image of astrocyte of Mlc1-YFP taken in D. The maximum intensity projection over 30-µm-thick volume was applied. Scale bar indicates 40 µm. Experiments were repeated twice (B), once (C), twice (D, F) three times (E) with independent brains. The representative images are shown. For B-F, the scale of "after-CUBIC-X" brain was used.

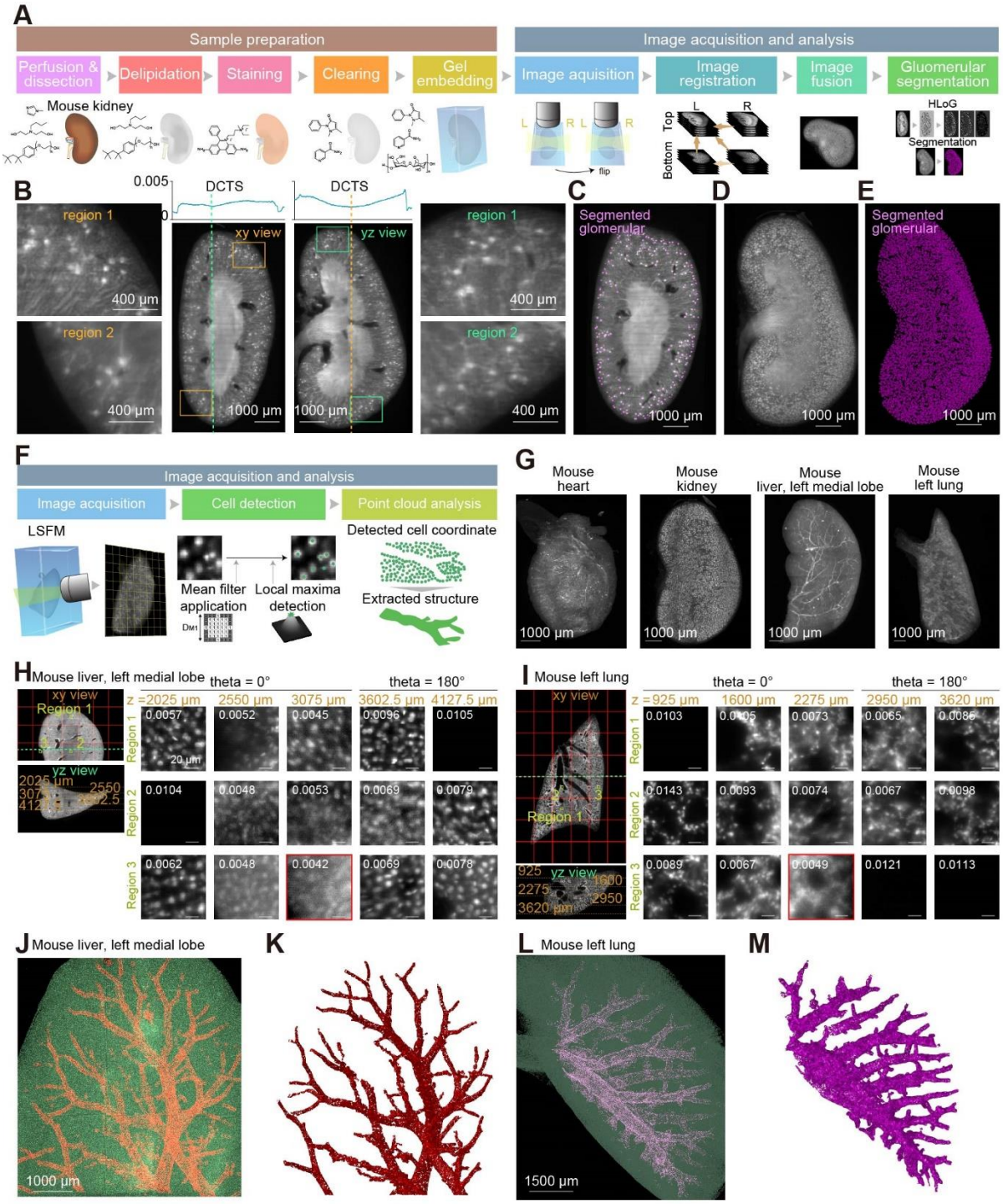

Figure 18. Comprehensive cell detection in highly cleared mouse organs by high-resolution imaging.

(A) Scheme of CUBIC-based protocol for kidney glomerular segmentation. Samples were prepared using CUBIC protocol I. (B) Sectional images of multi-directionally fused images of kidney. The discrete cosine transformation Shannon entropy (DCTS) (Royer et al., 2016) is shown above the sectional images as an indicator or image quality. (C) Sectional image of

segmented glomeruli of the kidney. Segmented renal glomeruli are shown in magenta. The renal glomeruli in the kidney were comprehensively analyzed by a Hessian-based difference of Gaussian (Zhang et al., 2015). (D,E) Three-dimensional reconstitution of fused images of kidney (D), and segmented renal glomeruli (E). (F) Scheme of the CUBIC-based protocol for whole-organ cell analysis. (G) Volume-rendered mouse organ images obtained with high-resolution light sheet microscopy. Organs were stained with nuclear-staining dye. (H,I) Representative images of nuclear-stained liver (H) and lung (I). Images with the lowest DCTS are framed in red. DCTS value is shown in the upper-left corner of each image. (J,K) Partial liver is represented as an ensemble of detected cellular nuclei ("point cloud"). Tubular structures were extracted from the point clouds. (L,M) Point cloud representation of the left lung. Tracheas were extracted from the point clouds.

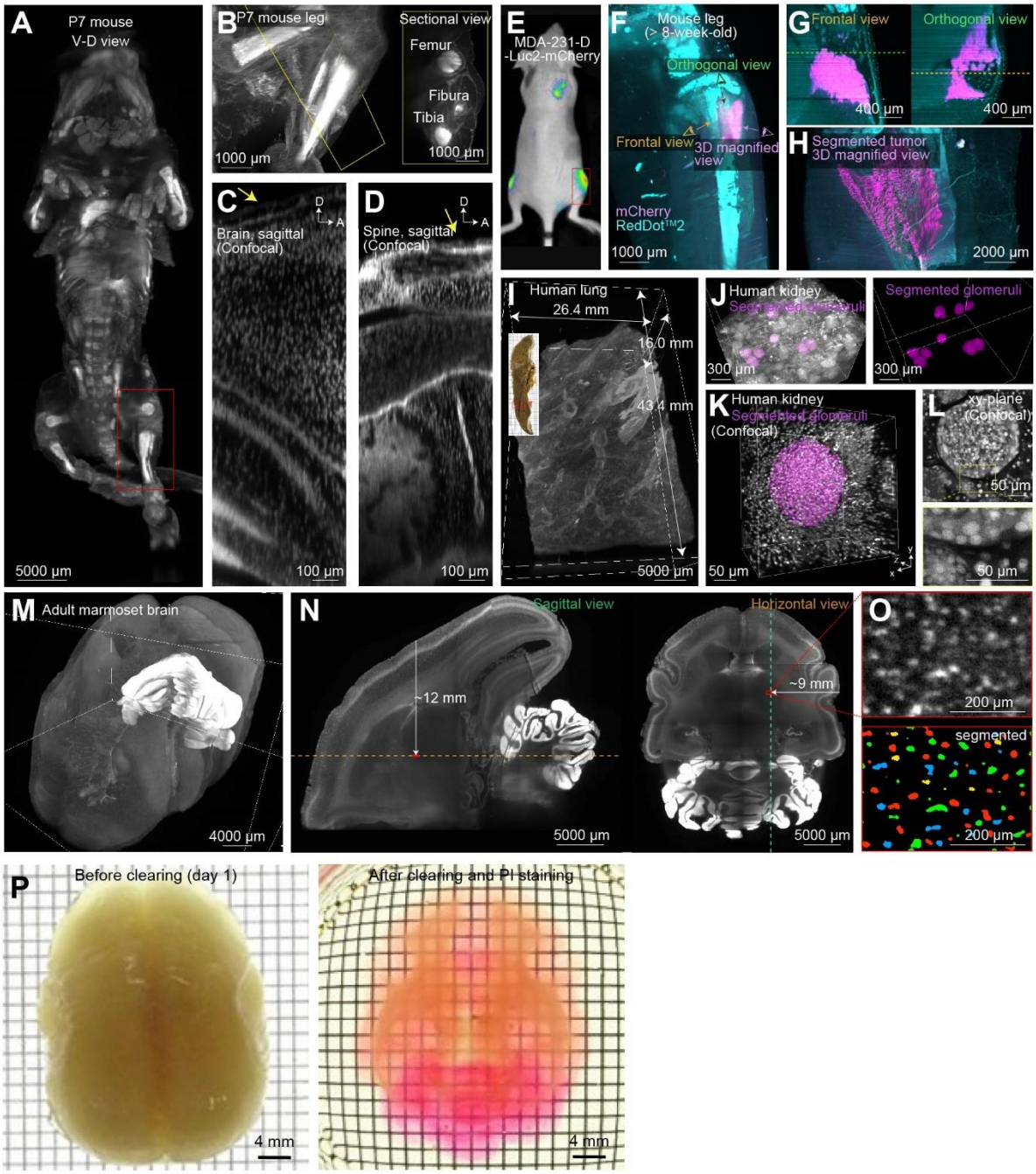

Figure 19. Scalable imaging of mouse whole body including bone and of large human tissue blocks with single-cell resolution.

(A and B) Volume-rendered images of whole mouse body (P7) stained with nuclear-staining dye. Ventral-dorsal whole-body view (A) and magnified view of left leg (B). Inset of B, sectional view of the leg. CUBIC protocol II was applied. (C,D) Confocal images of the brain inside the skull in a sagittal plane, and of the spine in a sagittal plane. Yellow arrows indicate bone tissues. (E) Bioluminescence image of an MDA-231-D-injected immunodeficient

BALB/c-nu/nu mouse. (F) Volume-rendered image of the right leg of the mouse in (E). Magenta and cyan indicate metastasized cancer cells (mCherry) and nuclei (Reddot^{TM}2), respectively. (G and H) Frontal (G, left), orthogonal (G, right), and magnified (H) views of F. For H, the segmented metastatic colony was visualized. For F-H, CUBIC protocol II was applied. (I) Volume-rendered image of the autofluorescence in a dissected human lung. CUBIC protocol III was applied. (J) Volume-rendered image of nuclear stained human kidney. Several glomeruli were segmented and are shown at right. CUBIC protocol III was applied. (K and L) Confocal imaging of a single glomerulus in the human kidney. Volume-rendered image (K), sectional image (L, upper) and magnified single-cell-resolution view of the sectional image (L, lower). (M-O) Adult marmoset brain stained for nuclei. Volume-rendered image of whole brain (M), sectional views (N), and highly resolved images (O). All images acquired with LSFM. Modified CUBIC protocol I was applied. (P) Adult marmoset brain was cleared by a modified CUBIC protocol I. Bright field images of the adult marmoset brain just after starting clearing (Day 1) and after complete clearing and staining are shown.

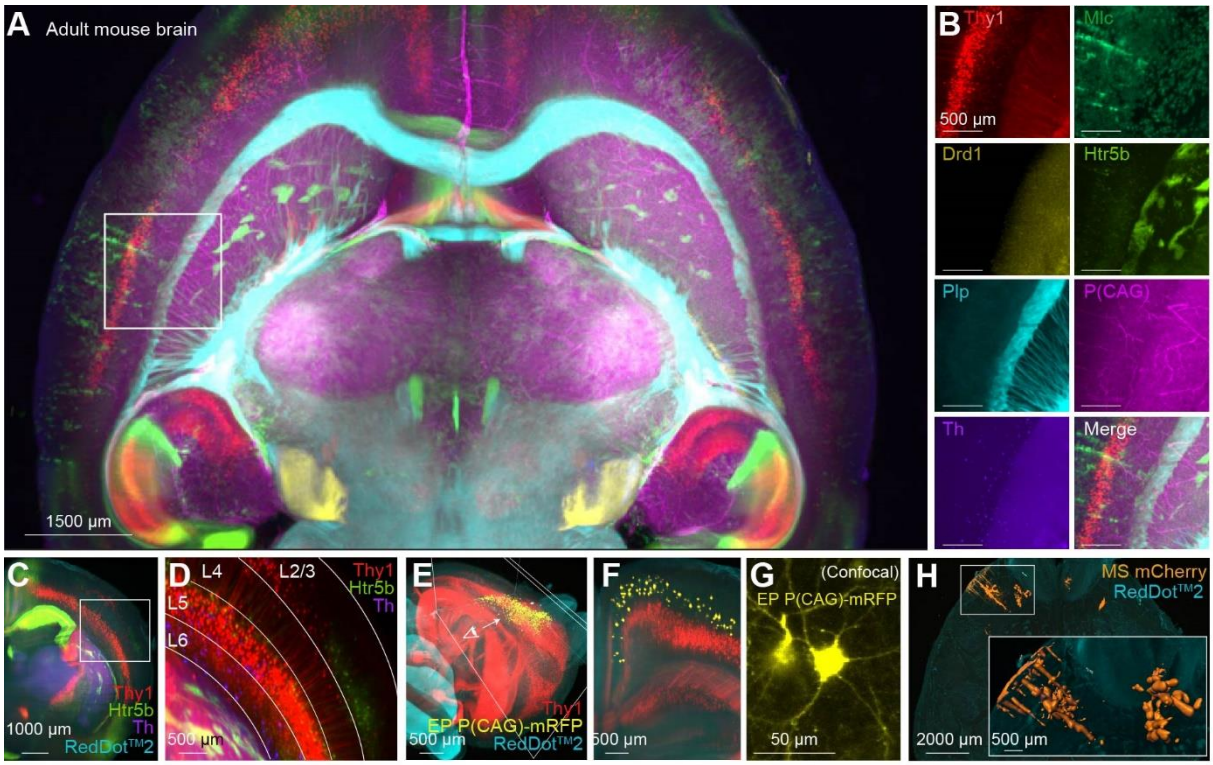

Figure 20. Multiple visualization of transgenically labeled FPs in mammalian brains and scalable imaging of brains with single-cell resolution.

(A-D) Virtual multiplex images of FP-expressing mouse brains registered to a standard brain. (A) Overlaid images of seven different FPs (horizontal view; 300-μm-thick projection). (B) Individual expression patterns and merged images in magnified views of the indicated region of A. Overlaid images of three different FPs (coronal view; 300-μm-thick projection) (C) and magnified view of the indicated region of C (D). Cortical layer structures are indicated in D. (E and F) Multiplex images of mouse brain labeled with EP-induced mRFP overlaid with Thy1 and nuclear images. Volumetric image (E) and coronal view of the 300-μm-thick projection in E (F). (G) Subcellular resolution imaging of mRFP-expressing cells by confocal microscopy. (H) Metastasized colonies of MDA-231-D cells expressing mCherry (MS mCherry) in mouse brain; volumetric image overlaid with nuclear image. Inset shows segmented volumes of cancer metastasis. For A-H, CUBIC protocol I was applied.

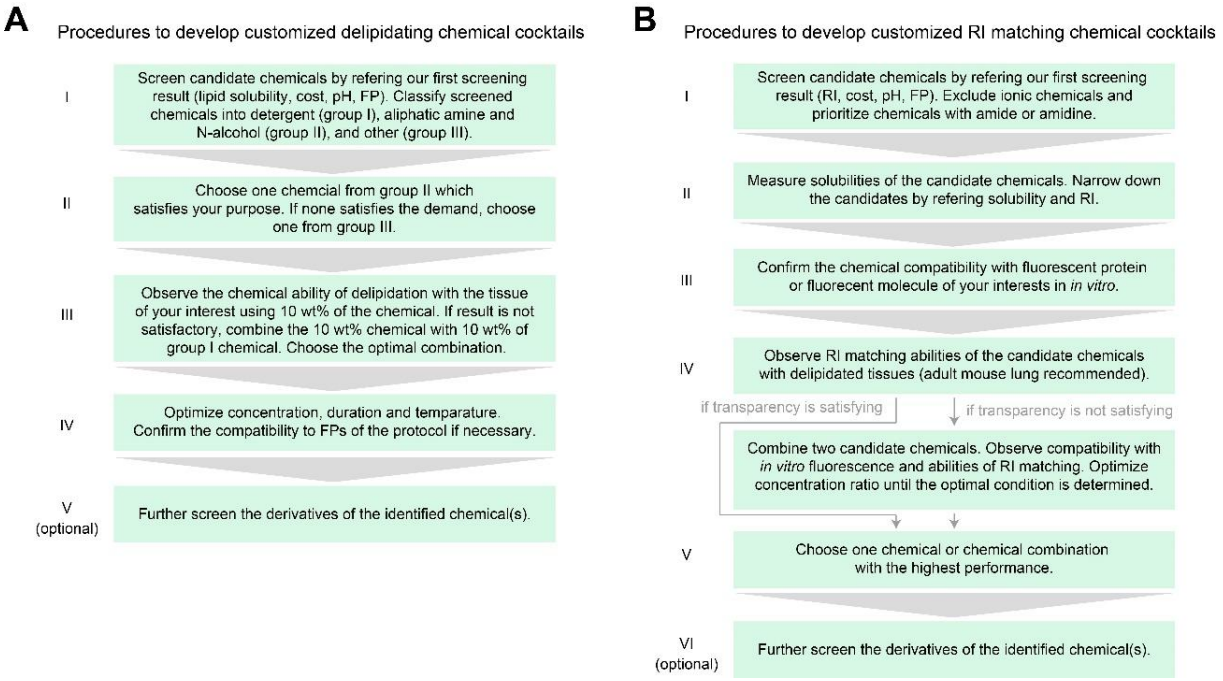

Figure 21. Flowcharts for developing customized tissue-clearing cocktails.

(A) Procedure for developing customized delipidating chemical cocktails. (B) Procedure for developing customized RI-matching chemical cocktails.

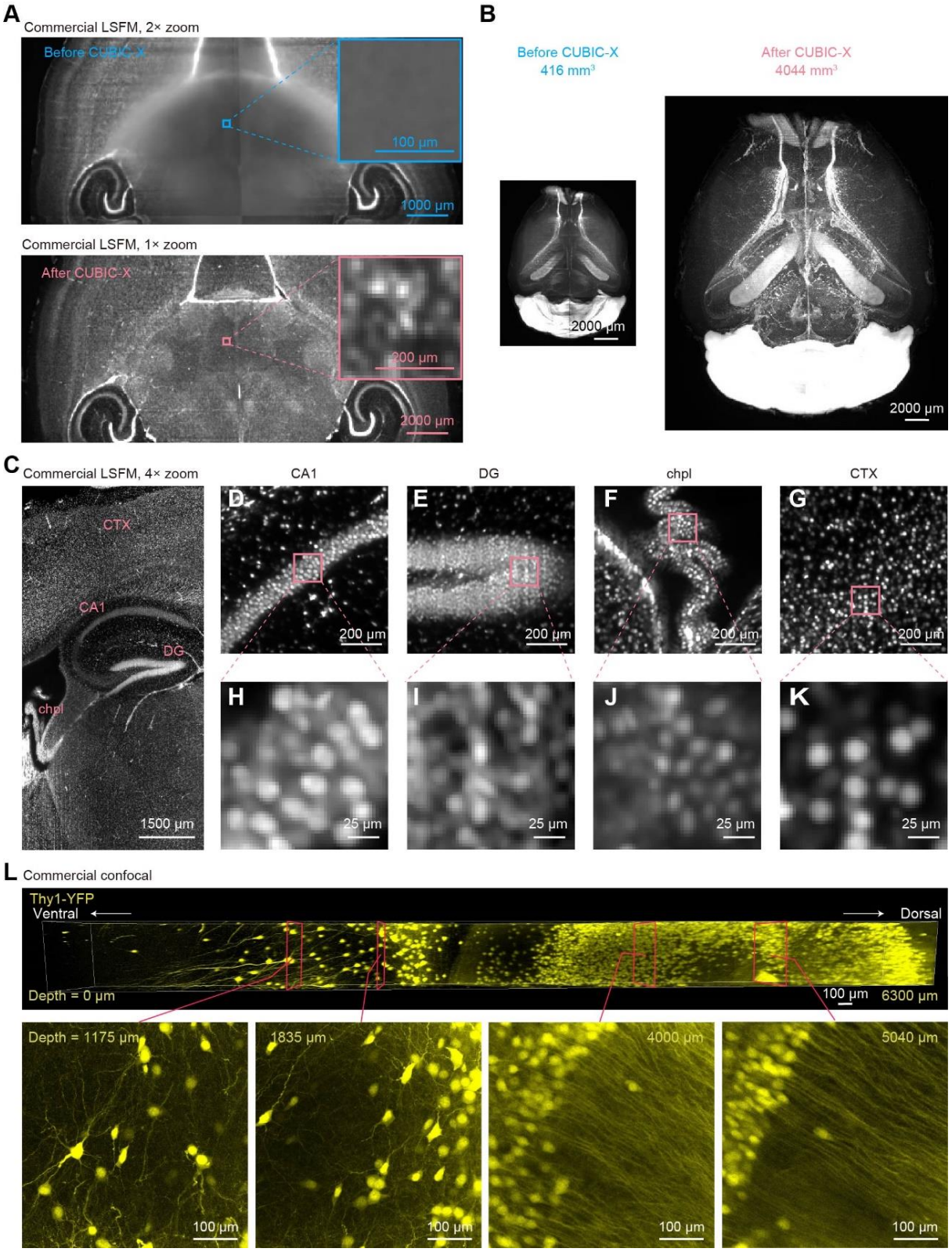

Figure 22. CUBIC-X brain images acquired by commercial LSFM and commercial confocal microscopy.

(A) Using a commercial LSFM, a low-magnification images of a PI-stained brain before (upper) and after (lower) CUBIC-X were obtained with 2× and 1× zoom lens, respectively. Insets: magnified views of the brains. (B) Volume-rendered images of a PI-stained brain before (left) and after (right) CUBIC-X in the same scale. Volumes were quantified by segmenting the brains. (C) PI-stained brain after CUBIC-X treatment was imaged with commercial LSFM with 4× magnification. To generate a virtual thin light sheet, four images with different light sheet focus positions were tiled together. DG: dentate gyrus, chpl: Choroid plexus, CTX: Cerebral cortex. (D-G) Magnified views of representative regions in brain. (H-K) Magnified views of D,E,F,G, respectively. (L) Fluorescent protein imaging of a Thy1-YFP-H mouse brain with a commercial confocal microscope. A Thy1-YFP-H mouse brain was cleared and expanded with CUBIC-X protocol, and imaged with confocal microscopy (25×, NA = 1.0). The volume rendered image (an upper panel; a volume size of 0.5 mm × 0.5 mm × 6.3 mm) and images of maximum-intensity projections (lower panels; 225 μm, 225 μm, 10 μm, 10 μm in thickness from left) are visualized. For all panels, experiments were repeated three times with independent brains. The representative images are shown.

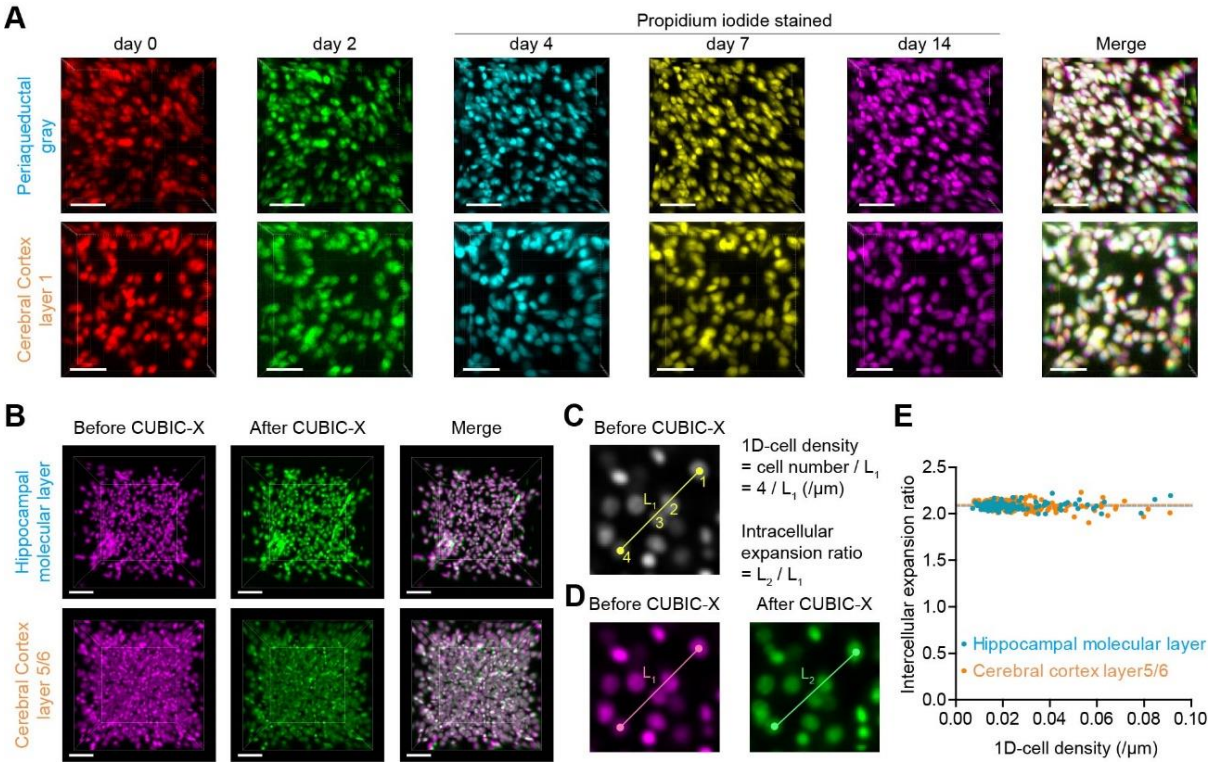

Figure 23. Multi-cellular scale evaluation of distortion and cellular loss during delipidation and expansion procedures.

(A) Sequential observation of nuclei during the delipidation process. The sliced brains of R26-H2B-EGFP mice were observed prior to the delipidation process (day 0). The slices were repeatedly observed during the delipidation process (day 2, 4, 7 and 14). Because repeated observation with fluorescence microscopy bleaches EGFP signal, propidium iodide was added at day 3 to enhance the signal of nuclei. Two regions of the brains (periaqueductal gray and cerebral cortex layer 5/6) are shown. Scale bars indicate 25 μm in the scale of a "before-CUBIC-X" brain. (B) Multi-cellular scale comparison of "before-CUBIC-X" brain and "after-CUBIC-X" brain. Two regions (hippocampal molecular layer and cerebral cortex layer 5/6) are shown. The corresponding images of "after-CUBIC-X" brain, which were linearly registered to "before-CUBIC-X" brain images by affine transformation, are also shown. It was confirmed that none of the nuclei were lost in the investigated area. The merged images after registration are shown on the right. Scale bars indicate 50 μm in the scale of a "before-CUBIC-X" brain. In (A) and (B), a perspective 3D rendering was used by Imaris software for visualization. Experiments were repeated three times with independent brain slices or brains. The representative images are shown. (C,D) Schematic procedures of the measurement of 1D-cell density (C) and intercellular expansion ratio (D). 1D-cell density was measured for every pair

of cells by counting the number of nuclei between the pair. Intercellular expansion ratio was calculated for every pair of cells as L2/L1. For the analysis, images of “after-CUBIC-X” were registered to images of “before-CUBIC-X” by similarity transformation. (E) The relation between 1D-cell density and Intercellular expansion ratio. Blue and orange dashed lines indicate overall expansion ratios in hippocampal molecular layer and cerebral cortex layer 5/6, respectively.

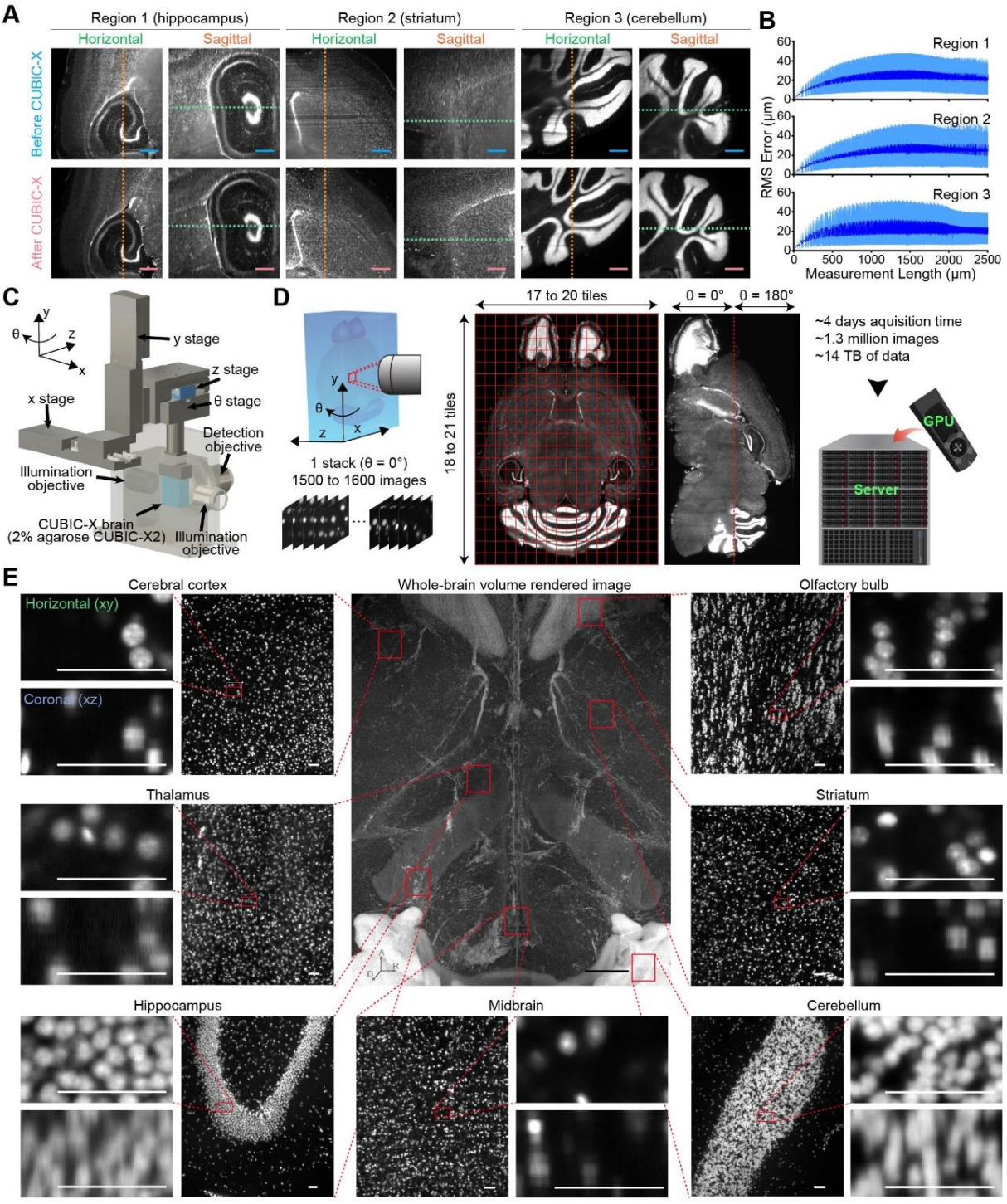

Figure 24. Whole-brain imaging of a CUBIC-X expanded brain with customized LSFM.

(A) Comparison of a PI-stained brain cleared by the modified ScaleCUBIC-2 ("before-CUBIC-X") and an expanded brain by the CUBIC-X treatment ("after-CUBIC-X"). Three regions (2.5 mm × 2.5 mm × 2.5 mm) of a "before-CUBIC-X" brain are shown in the upper row from both horizontal and sagittal views. The corresponding images of an "after-CUBIC-X" brain, which

were linearly registered to the “before-CUBIC-X” brain images, are also shown in the lower row. Scale bars indicate 500 μm in the scale of a “before-CUBIC-X” brain. (B) The quantification of the non-linear distortion caused by CUBIC-X treatment. The root-mean-square (RMS) errors were quantified. Its average (blue) and standard deviation (light blue) are plotted against the measurement length. Sparsely sampled pairs of voxels were used. I note all lengths are represented in the scale of a “before-CUBIC-X” brain. (C) Computer-aided design (CAD) image of a sample mounting in the customized light-sheet fluorescence microscope (LSFM). A CUBIC-X brain embedded in 2% agarose CUBIC-X2 is suspended in oil (RI = 1.467). (D) Overview of whole-brain imaging procedures. (E) A volume rendered and single-plane images of a PI-stained CUBIC-X brain. A volume rendered image of a whole brain is shown in the center. An original single-plane and its magnified (10×) images are shown for cortex, thalamus, hippocampus, midbrain, olfactory bulb, corpus callosum and cerebellum, respectively. Both horizontal (xy) and coronal (xz) views are shown. Experiments were repeated more than ten times with independent brains. Scale bars indicate 1000 μm for whole-brain image and 50 μm for others in the scale of “before-CUBIC-X” brain.

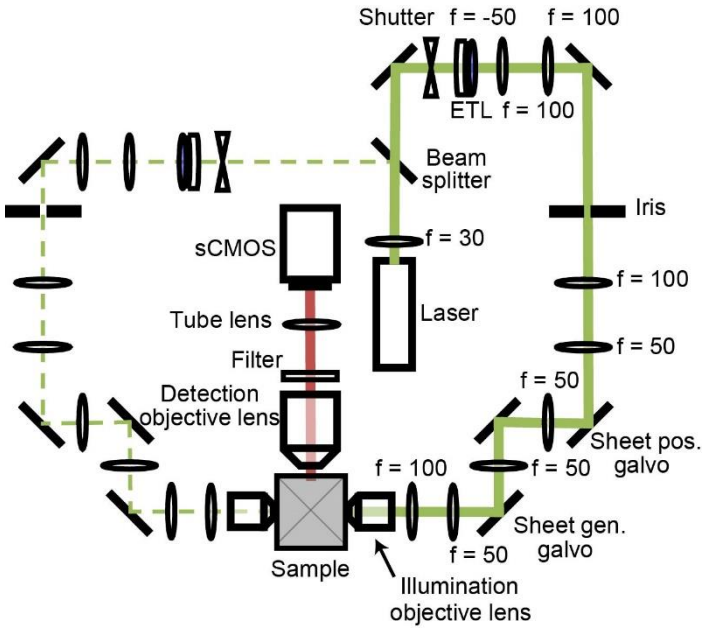

Figure 25. Optical layout of the customized light sheet microscope.

Electrically tunable lenses (ETL) were put for the adjustment of the light-sheet focus position along the x-direction. Galvanometer scanners were introduced for adjusting a light-sheet position along z-direction (shown as “sheet pos. galvo”). Autofocus (i.e. adjustment of the light-sheet z-position) by these galvanometer scanners was performed every 1 mm.

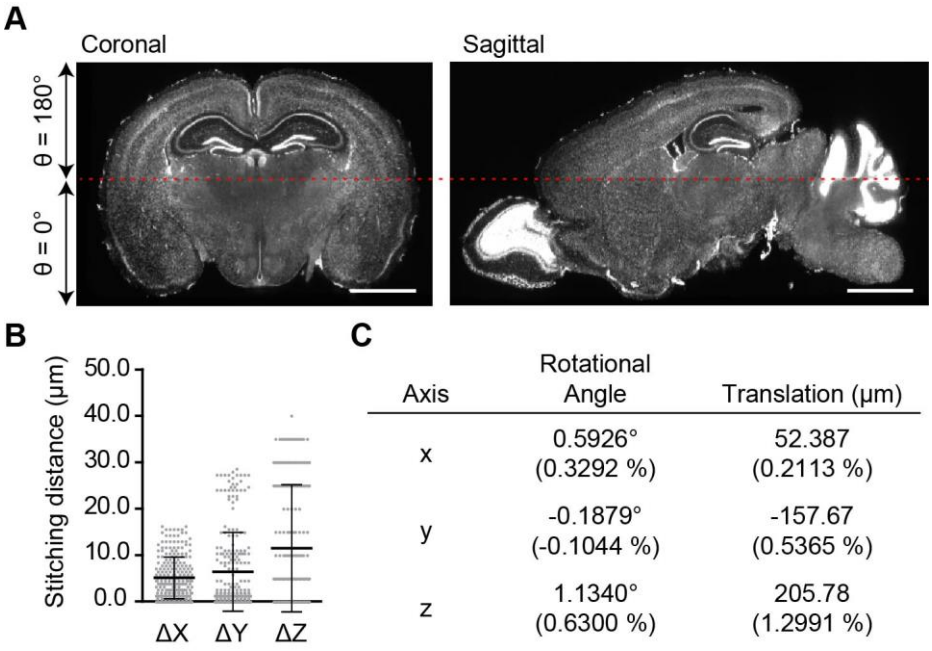

Figure 26. Quantitative measurements of the displacements during the imaging sequence.

(A) Coronal and sagittal image merged by θ-rotation with dorsal (θ = 0°) and ventral (θ = 180°) sides of the CUBIC-X brain. Red dashed line is the merged position. Scale bars indicate 2000 μm in the scale of a "before-CUBIC-X" brain. (B) Quantitative evaluation of stitching displacement errors in x, y, and z-axes in the xy-direction tiling. I prepared 10 × 10 tiles of 600 images for each stack with 10% overlap in both x- and y-direction. Stitching distance was calculated with the stitching software, TeraStitcher. The displacement errors of all possible combinations of the stacks are shown. The average ± SD are shown. (C) Quantitative evaluation of theta tile displacement around x, y, and z-axes. I prepared two sets [ventral (θ = 0°) and dorsal view (θ = 180°)] of 10 × 10 tiles of 600 images for each stack with 10% overlap in both x- and y-direction. These images were stitched with TeraStitcher, and the resulting stitched images were downsampled. The downsampled ventral images were registered to the downsampled dorsal images by ANTs. Then Euler angle around x, y, and z-axes, and translation were calculated.

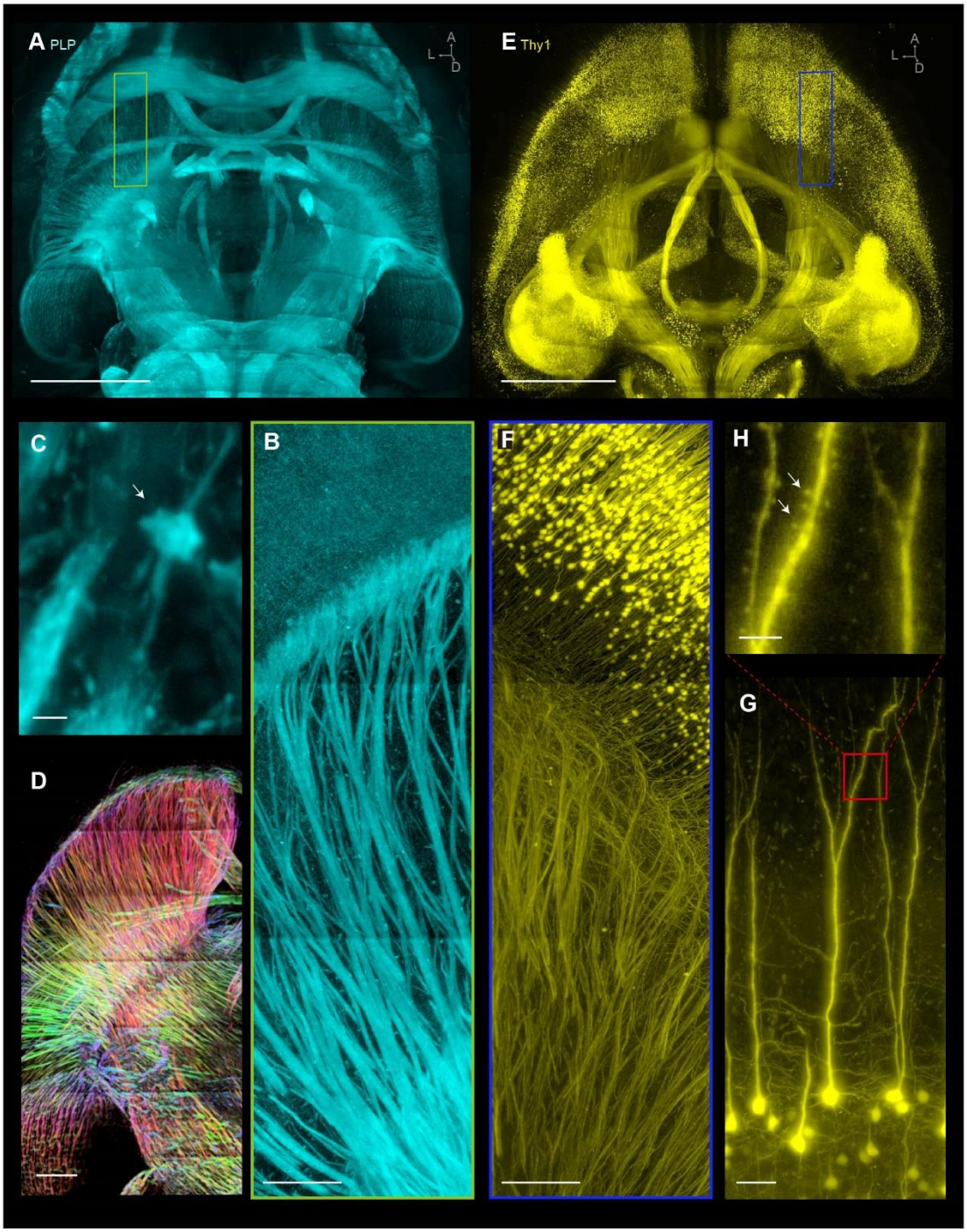

Figure 27. Whole-brain imaging of a CUBIC-X expanded brain with customized LSFM resolves multiscale cellular structures.

(A) Volume rendered image of PLP-tTA::tetO-ChR2EYFP mouse brain, imaged by customized LSFM. (B) Magnified view of A in the region enclosed in the green box. The maximum intensity projection along V-D axis spanning 500 μm was applied to generate the image. (C) Detailed view of A from the striatum region. Because CUBIC-X highly retains the fluorescent

proteins, subcellular structures of a single oligodendrocyte cell (indicated by a white arrow) can be clearly imaged by LSFM. (D) From the images shown in A, the fiber orientations were color-coded by their orientations, which were determined by applying fiber enhancement filter. (E) Volume rendered image of Thy1-YFP-H mouse brain, imaged by customized LSFM. (F) Magnified view of E in the region enclosed in the blue box. The maximum intensity projection along V-D axis spanning 1000 μm was applied to generate the image. (G) Detailed view of E from the cerebral cortex. (H) A magnified view of G in the region enclosed in the red box. Branching of axons as well as single spines (indicated by white arrows) can be clearly resolved by expanding the sample and using the high-resolution LSFM. In B, C, F, G and H, the image intensity was adjusted by taking the logarithms of raw intensity for better visual contrast. For B and F, three image tiles were stitched together by blending the overlapping regions with linear weight using "Pairwise Stitching" plugin in ImageJ. Scale bars indicate 5 mm (A), 500 μm (B), 20 μm (C), 1 mm (D), 5 mm (E), 500 μm (F), 100 μm (G), and 20 μm (H) in the scale of "after-CUBIC-X" brain.

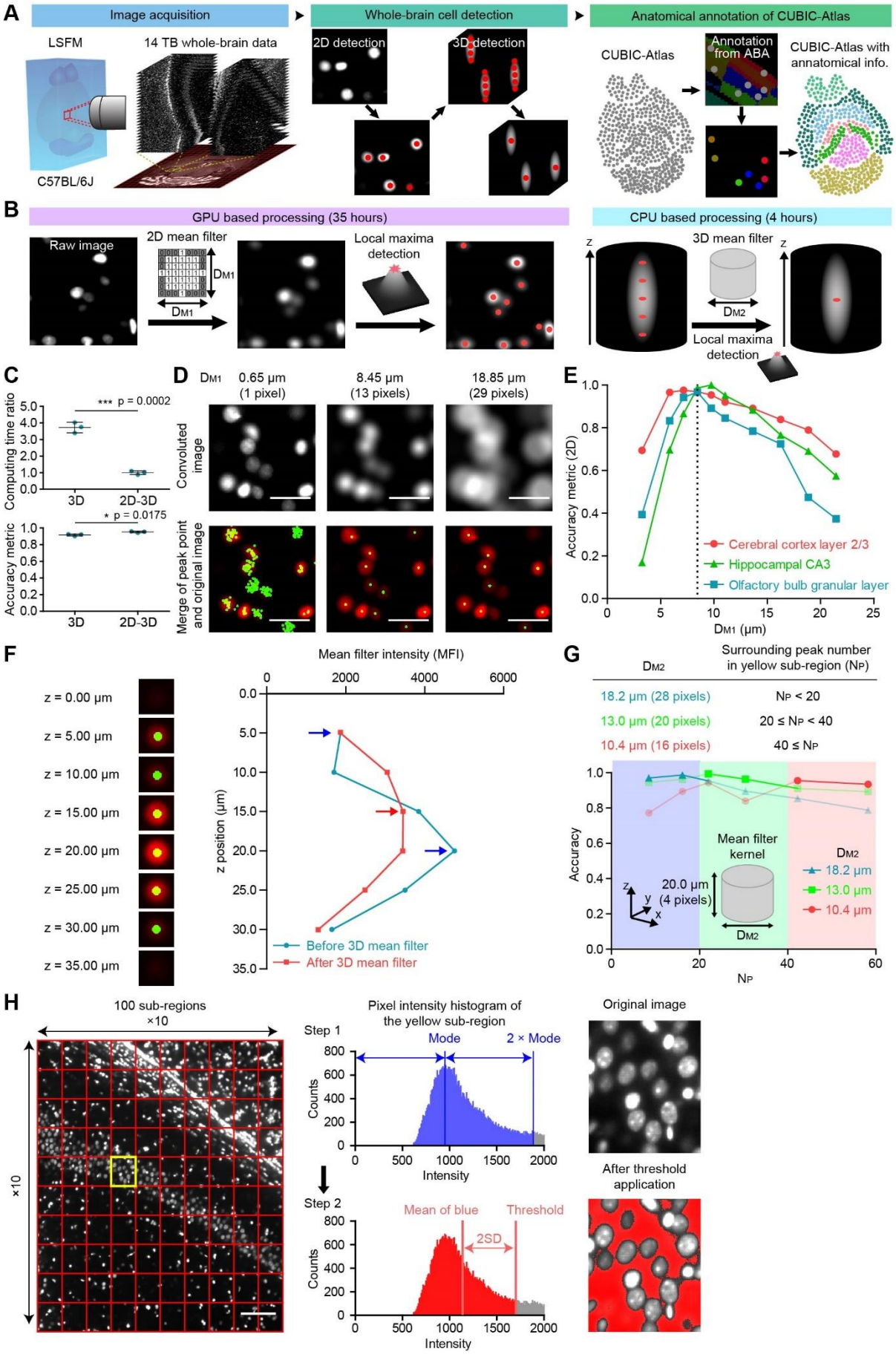
A
Image acquisition
Whole-brain cell detection
Anatomical annotation of CUBIC-Atlas
LSFM
14 TB whole-brain data
C57BL/6J
2D detection
3D detection
CUBIC-Atlas
Annotation from ABA
CUBIC-Atlas with annatomical info.
B
GPU based processing (35 hours)
CPU based processing (4 hours)
Raw image
2D mean filter
DM1
Local maxima detection
3D mean filter
DM2
Local maxima detection
C
Computing time ratio
*** p = 0.0002
3D
2D-3D
Accuracy metric
* p = 0.0175
D
DM1
0.65 μm (1 pixel)
8.45 μm (13 pixels)
18.85 μm (29 pixels)
Convoluted image
Merge of peak point and original image
E
Accuracy metric (2D)
Cerebral cortex layer 2/3
Hippocampal CA3
Olfactory bulb granular layer
DM1 (μm)
F
z = 0.00 μm
z = 5.00 μm
z = 10.00 μm
z = 15.00 μm
z = 20.00 μm
z = 25.00 μm
z = 30.00 μm
z = 35.00 μm
Mean filter intensity (MFI)
z position (μm)
Before 3D mean filter
After 3D mean filter
G
DM2
Surrounding peak number in yellow sub-region (NP)
18.2 μm (28 pixels)
NP < 20
13.0 μm (20 pixels)
20 ≤ NP < 40
10.4 μm (16 pixels)
40 ≤ NP
Accuracy
Mean filter kernel
20.0 μm (4 pixels)
DM2
18.2 μm
13.0 μm
10.4 μm
NP
H
100 sub-regions
×10
×10
Pixel intensity histogram of the yellow sub-region
Step 1
Mode
2 × Mode
Counts
Intensity
Step 2
Mean of blue
Threshold
2SD
Original image
After threshold application

Figure 28. A two-step convolution algorithm for the detection of cell nuclei in a whole brain.

Construction of a single-cell-resolution mouse brain atlas (CUBIC-Atlas).

(A) Overview of construction of the CUBIC-Atlas. First, I acquired the images of highly resolved cellular nuclei throughout the C57BL/6J male mouse brain ("Image acquisition"). Second, I developed an algorithm to comprehensively detect individual nuclei without omission and overlap ("Whole-brain cell detection") to construct the CUBIC-Atlas. I annotated the individual points of CUBIC-Atlas by using anatomical annotations of ABA ("Anatomical annotation of CUBIC-Atlas"). (B) Schematic of cell detection of nuclear-stained CUBIC-X brain images. To establish two-step cell-detection algorithm, I first detected individual cells in a 2D xy-plane, and then unified the multiply-detected cells in 3D volume. In each step of this algorithm, I detected local maxima after applying a different mean filter. I used a 2D mean filter kernel with a diameter DM1 in the first GPU-based 2D cell-detection step, and 3D mean filter kernel with a diameter DM2 in the second CPU-based 3D cell-unifying step, respectively. (C) Comparison of calculation speed and accuracy metric in cell detection between 3D-based one-step convolution algorithm and the two-step algorithm (***$p < 0.001$, *$p < 0.05$, independent two-tailed t-test). The average ± SD were evaluated in the independent three regions. (D) The effect of the first 2D mean filter in cell detection. While no filters [DM1 = 0.65 μm (1 pixel)] to the raw data resulted in multiple detections of a single cell, large diameter [DM1 = 18.85 μm (29 pixels)] led to the failure in detecting all cells within the image. The accuracy metric of cell detection depends on mean filter diameter (DM1). Scale bars indicate 50 μm in the scale of an "after-CUBIC-X" brain. (E) The plots of the accuracy metric of 2D cell-detection against DM1 in cerebral cortex layer 2/3, hippocampal CA3, and olfactory bulb granular layer, respectively. I found DM1 of 8.45 μm was the optimal value over the three regions. (F) The effect of the second 3D mean filter in cell detection. After 2D cell detection, a single cell was multiply detected over the several stacked images (left). Then, I attempted to unify the multiply-detected points by detecting local maxima of these points in the z-direction. I succeeded in the convergence of the multiply detected points (red arrow; local maxima of after 3D mean filter) after 3D mean filtering while failing to unify these points before 3D mean filtering blue arrow; local maxima of before 3D mean filter. (G) The plots of the accuracy metric of 3D cell-unification against surrounding peak number (NP) in the three different DM2 value. I note that optimal values for DM2 were highly dependent on the density of cells. 13.0 μm for DM2 was

the most accurate parameter value for the brain region with an intermediated cell density whereas 18.2 μm and 10.4 μm for DM2 were the more accurate for those with lower and higher cell density, respectively. (H) Background threshold was determined by the histogram of pixel intensity in each sub-region (1/100 of the original image) in the 2D cell-detection step. We determined the intensity less than 2 × mode as background intensity, and then extracted background signals (blue). Next, we calculated mean intensity and SD from the resulting histogram, and then determined the intensity less than 2 SD above the mean intensity as an image threshold (red). Scale bars indicate 200 μm in the scale of an "after-CUBIC-X" brain.

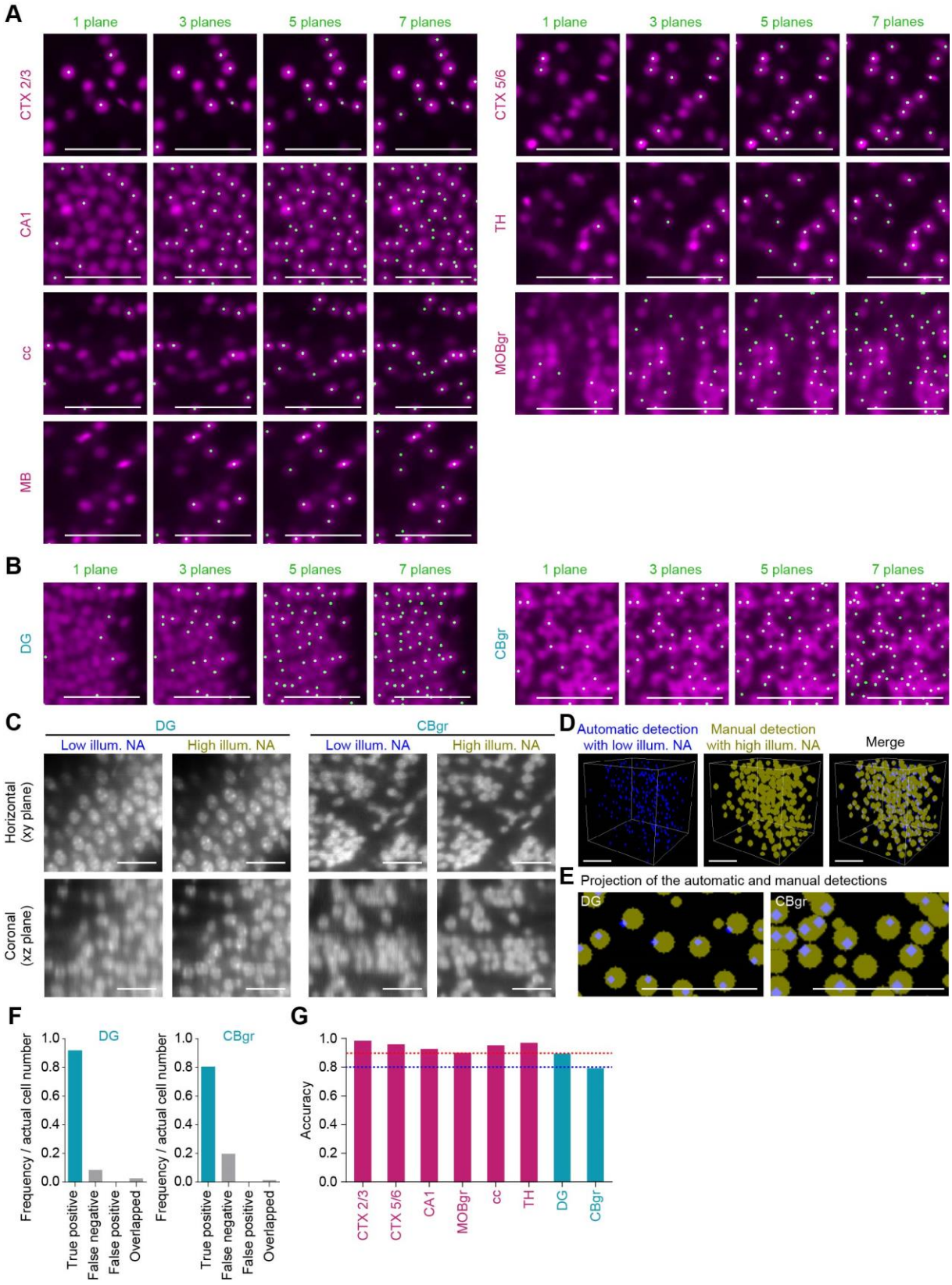

Figure 29. The evaluation of accuracy metric for the automated detection of cell nuclei in a whole brain.

(A) The representative images of cell detection in sparsely populated areas. Because cell detection was performed in a three-dimensional manner, the cellular nuclei shown in single planes (magenta) were repeatedly detected in different axial positions. The lateral positions of detected cellular nuclei (green) in surrounding z-planes (1, 3, 5, or 7) were shown in each image. CTX, cerebral cortex; TH, thalamus; cc, corpus callosum; MOBgr, main olfactory bulb granular layer; MB, midbrain. Scale bars indicate 100 μm in the scale of an "after-CUBIC-X" brain. (B) The representative images of cell detection in densely populated areas. DG, dentate gyrus; CBgr, cerebellum granular layer. For A and B, experiments were repeated more than ten times with independent brains. The representative images are shown. (C) Image comparison of low-illumination-NA condition (measured FWHM = 11.0 μm, scanning step size= 5.0 μm) and high-illumination-NA condition (measured FWHM = 5.2 μm, scanning step size= 2.0 μm). Horizontal and coronal sectional images of DG and CBgr are shown. Scale bars indicate 50 μm in the scale of "after-CUBIC-X" brain. Experiments were repeated three times with different brain areas. The representative images are shown. (D) Comparison of the manually annotated nuclei with the automatically detected nuclei. Two people independently annotated the nuclei for manual annotation. Scale bars indicate 50 μm in the scale of "after-CUBIC-X" brain. (E) Projected image of manually annotated nuclei and automatically detected nuclei in DG and CBgr. The projection of 25 μm are shown. Scale bars indicate 50 μm in the scale of "after-CUBIC-X" brain. (F) Details of the accuracy of the automated two-step cell-detection algorithm in DG and CBgr. (G) The accuracy metric of the cell detection in various brain areas. Red and blue lines indicate 0.9 and 0.8, respectively. For F and G, one and three volumetric images were used for each to evaluate accuracy.

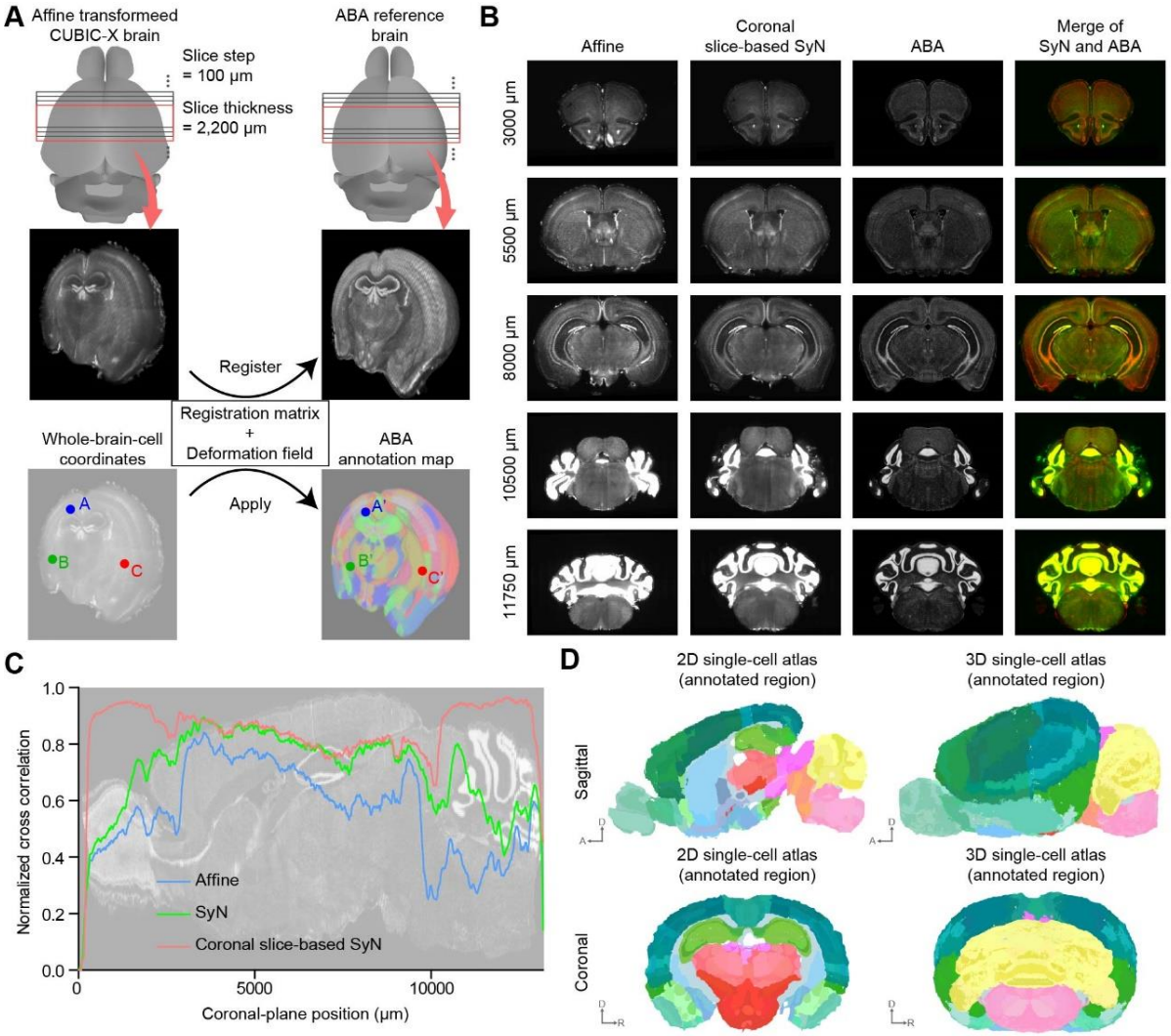

Figure 30. Non-linear registration of coronal slices in a CUBIC-X brain to Allen Brain Atlas.

(A) A schematic diagram for the registration of a CUBIC-X brain to an Allen Brian Atlas (ABA) brain based on the virtual coronal slices. After registration of the CUBIC-X brain images by affine transformation, I generated about a hundred overlapping 3D coronal slices with a 2.2-mm thickness at a 100-µm step both from the CUBIC-X and ABA brains. I then registered each coronal-slice image of the CUBIC-X brain onto the coronal-slice images of the ABA brain by non-linear transformation. (B) Coronal single-plane images of a CUBIC-X brain with affine transformation ("Affine"), a CUBIC-X brain with non-linear transformation based on coronal slices ("Coronal slice-based SyN"), an ABA brain ("ABA"), and merged coronal single-plane images of non-linearly transformed CUBIC-X (green) and ABA brains (red). (C) Normalized cross-correlations of a CUBIC-X brain against an ABA brain over entire coronal single-plane

positions by straightforward affine transformation (“Affine”, blue), straightforward non-linear transformation (“SyN”, green), and non-linear transformation based on coronal slices (“Coronal slice-based SyN”, red). (D) Sagittal and coronal images of a 2D and 3D single-cell-resolution mouse brain atlas (CUBIC-Atlas) based on an 8-week-old C57BL/6J mouse brain. For non-linear transformation, symmetric normalization (SyN) in ANTs software was used.

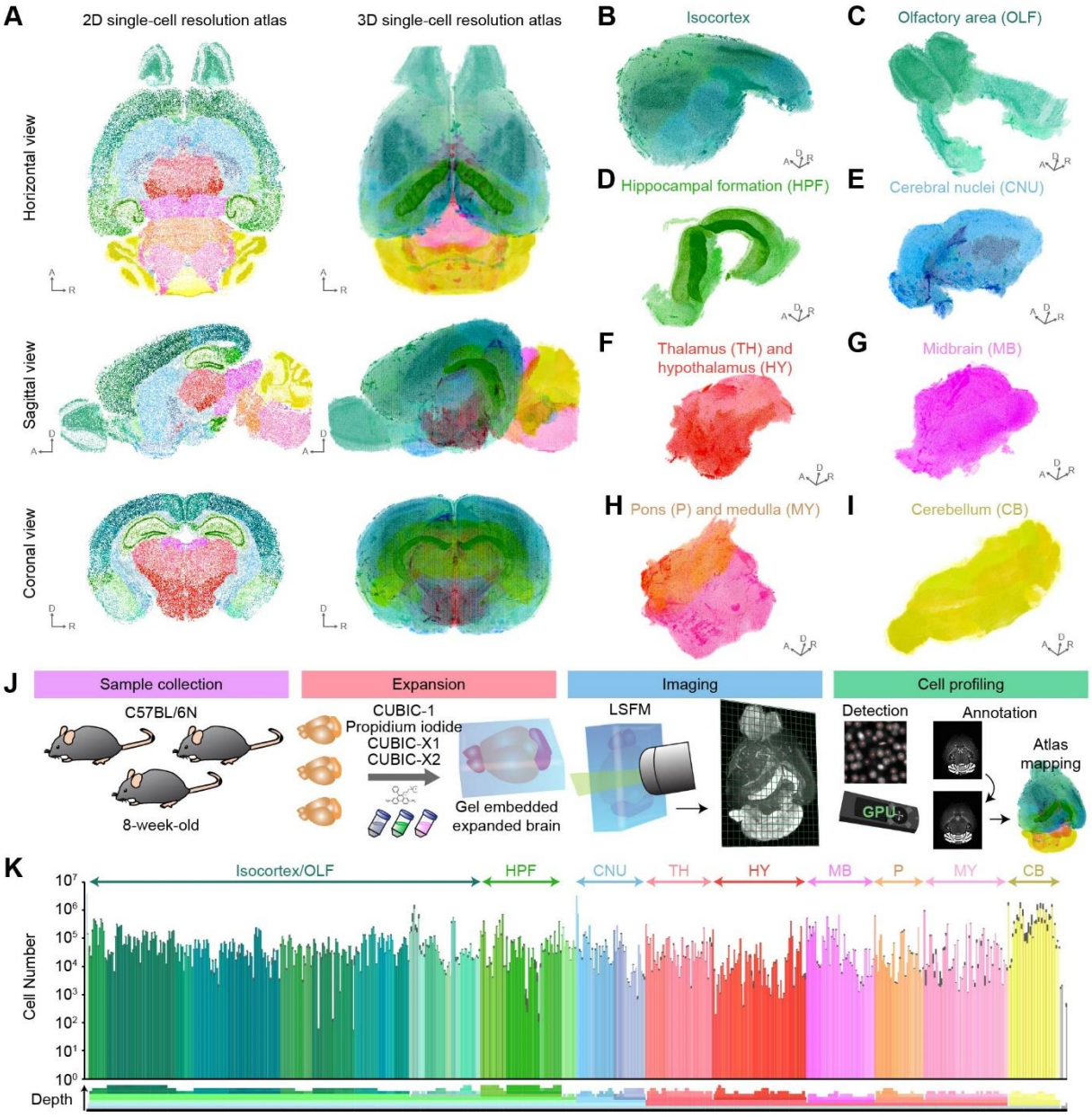

Figure 31. Construction of a single-cell-resolution mouse brain atlas (CUBIC-Atlas).

(A) The CUBIC-Atlas. Horizontal, sagittal and coronal view of single-plane images (left) and volume rendered images (right) of the CUBIC-Atlas. (B-I) Major anatomical areas in the CUBIC-Atlas. For B-J, experiments and annotations were repeated more than ten times with independent brains. (J) Overview of whole-brain cell counting of C57BL/6N 8-week-old male mice. (K) Cell number in each brain area. The average ± SD are indicated for each brain area (n = 3). The color represents an anatomical area. The color hue of each brain area indicates its parental anatomical structure whereas the color chroma of each brain area indicates a hierarchical depth in its parental anatomical structure. OLF, olfactory areas; HPF, hippocampal

formation; CNU, cerebral nuclei; TH, thalamus; HY, hypothalamus; MB, midbrain; P, pons; MY, medulla; CB, cerebellum.

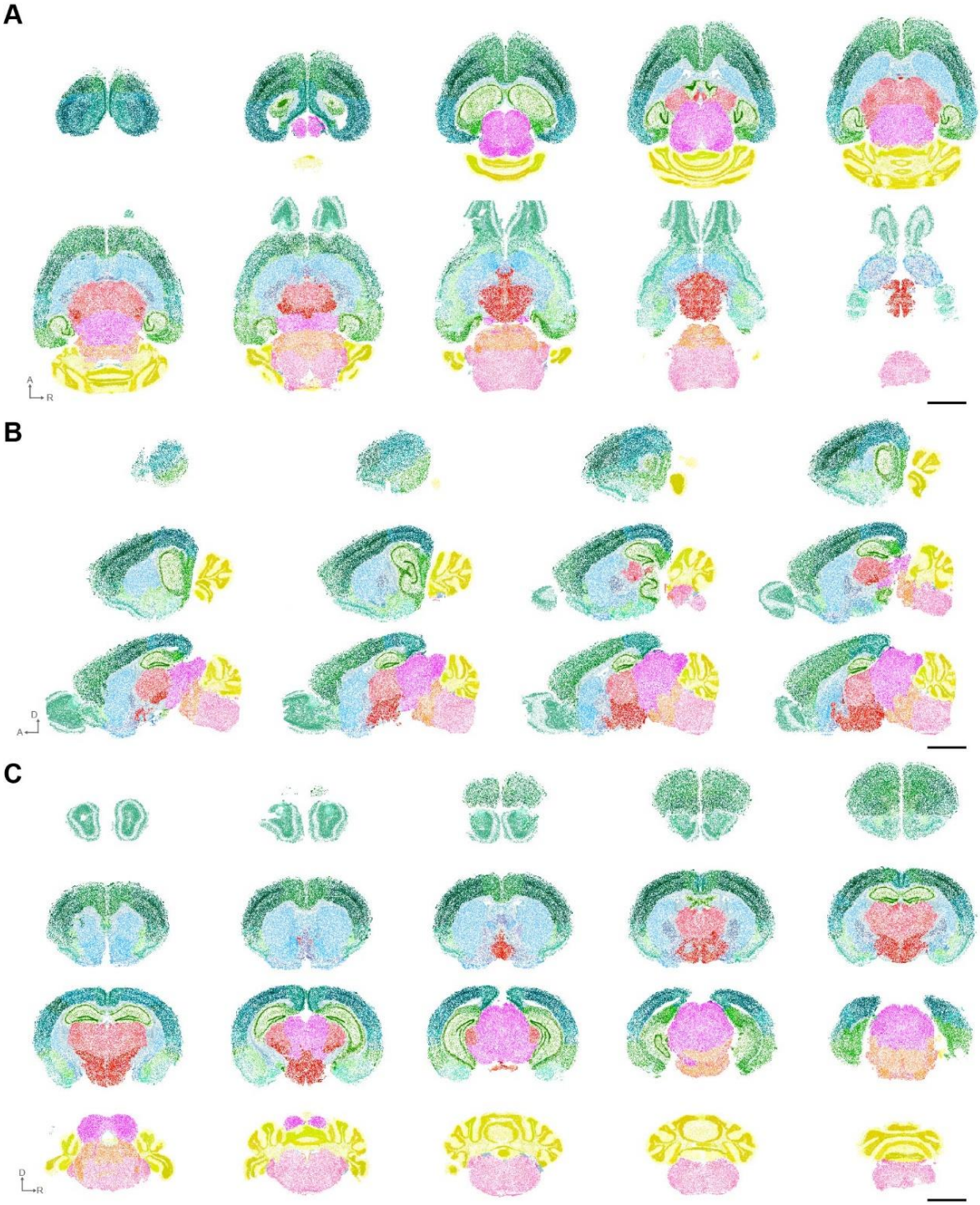

Figure 32. A single-cell-resolution mouse brain atlas (CUBIC-Atlas).

(A-C) Horizontal (A), sagittal (B) and coronal (C) single-plane images of CUBIC-Atlas. Each color indicates a corresponding anatomical area. Scale bars indicate 5 mm in the scale of "after-CUBIC-X" brain. Each slice is shown at 1.495 mm (A), 0.845 mm (B) and 0.585 mm (C) step.

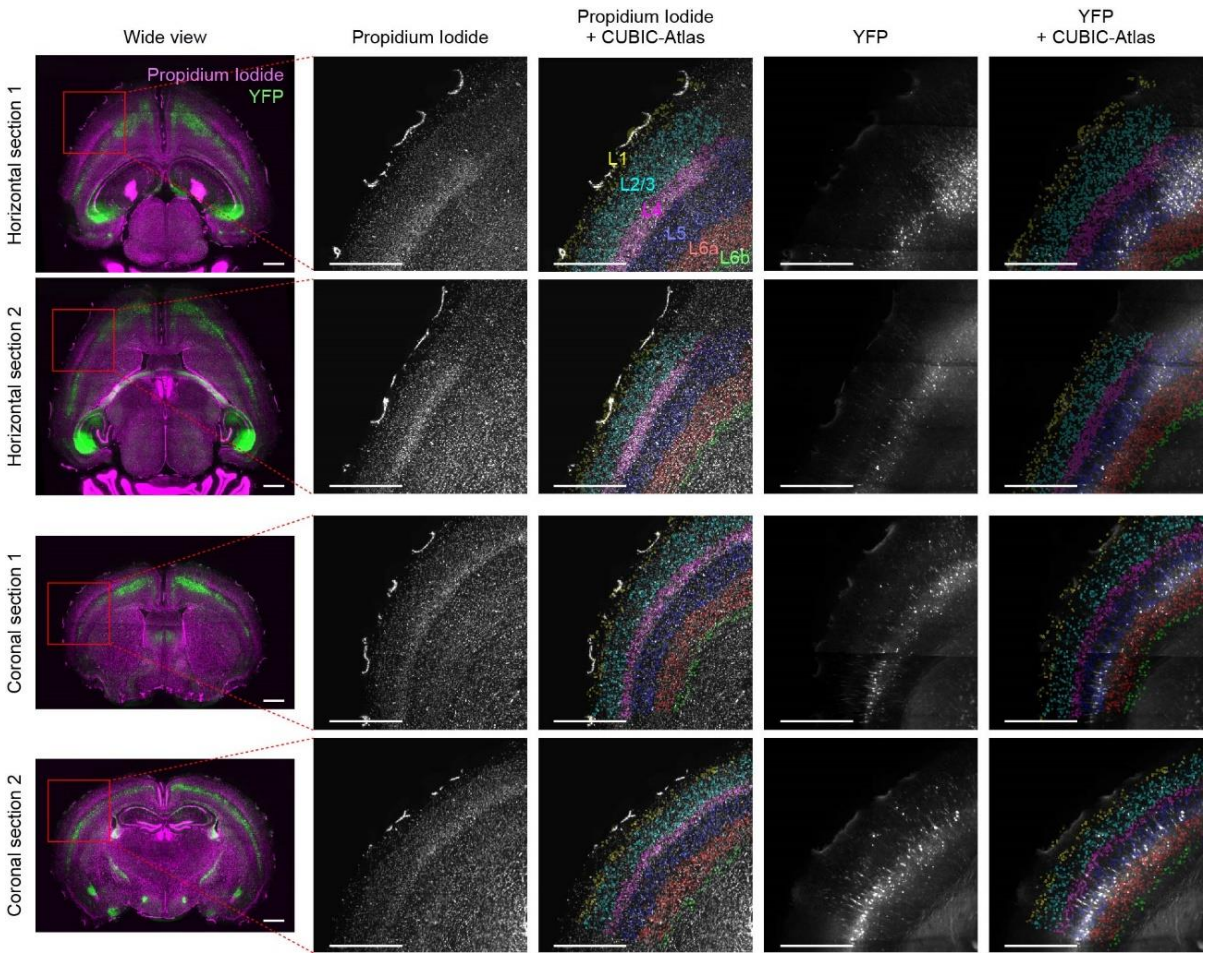

Figure 33. Layers of Cerebral cortex in a CUBIC-Atlas overlaid with a PI-stained Thy1-YFP-H mouse brain.

A PI stained Thy1-YFP-H mouse brain was expanded by CUBIC-X and imaged with the customized LSFM. The acquired volumetric images were downsampled, then non-linearly registered to a CUBIC-Atlas. The layer structures of CUBIC-Atlas were overlaid with the images of PI and YFP, respectively. Cerebral cortical layers of somatosensory areas, posterior parietal association areas, and visual areas of a CUBIC-Atlas were visualized with pseudo-color codes. L1, layer 1; L2/3, layer 2/3; L4, layer 4; L5, layer 5; L6a, layer 6a; L6b, layer 6b. Experiments were repeated twice with independent brains and the representative images are shown. Scale bars indicate 2000 μm in the scale of an “after-CUBIC-X” brain.

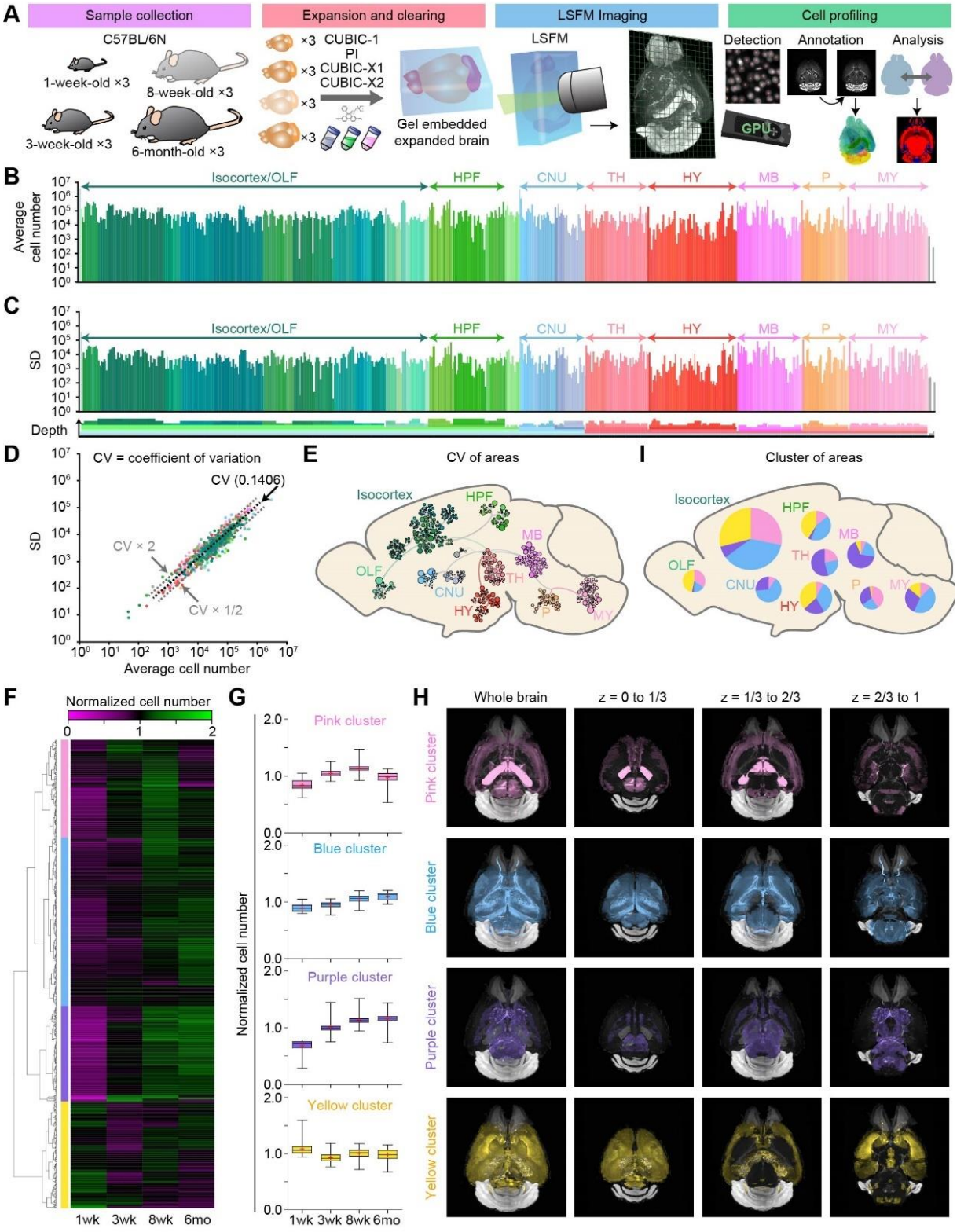

Figure 34. CUBIC-Atlas is applicable to whole-brain cell profiling over different aged mice.

(A) Overview of whole-brain cell profiling over different aged mice. In addition to the 8-week-old mice brains described in **Figure 28L**, the brain samples of 1-, 3-week-old and 6-month-old C57BL/6N male mice were collected, expanded by a CUBIC-X protocol, imaged by the customized LSFM and analysed with the CUBIC-Atlas. (B,C) The average cell number and the standard deviation (SD) over 1-, 3- , 8-week-old, and 6-month-old mice in each brain area (n = 3). The color represents an anatomical area. The parental hierarchical structure is shown as in **Figure 28L**. (D) The correlation between the average cell number and SD. (E) The coefficient of variance (CV) for cell numbers in each area. (F) Heatmap for hierarchical clustering of normalized cell number in each brain area. Mean values of three brains are shown. Four major clusters (pink, blue, purple and yellow clusters) were identified. (G) The normalized cell number in each cluster. Box plots indicate median and interquartile ranges. The plots were generated with normalized cell numbers of all individual areas of three brains for each age. Whiskers cover full ranges of distributions, along with a box showing 25−75% interquartile range, a dot showing the average and center line showing the median. (H) 3D distribution of each cluster in the mouse brain. (I) The ratio of clusters in each area. The size of circle indicates the number of anatomical areas. OLF, olfactory areas; HPF, hippocampal formation; CNU, cerebral nuclei; TH, thalamus; HY, hypothalamus; MB, midbrain; P, pons; MY, medulla. The normalized cell numbers of all individual areas of twelve brains were subjected to clustering analysis.

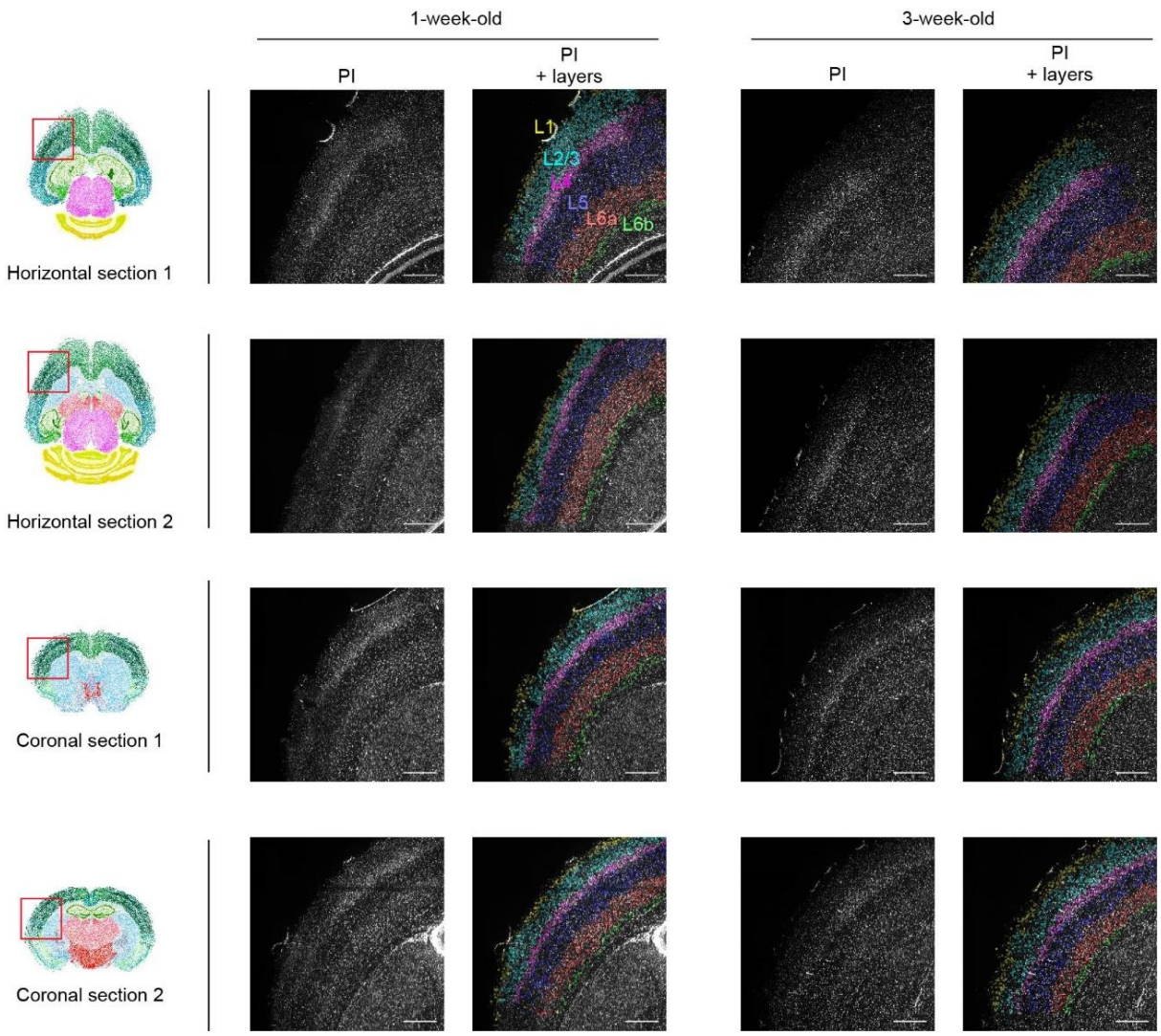

Figure 35. Mapping of 1-week-old and 3-week-old mice brains onto a CUBIC-Atlas.

PI-stained 1-week-old and 3-week-old mice brains were mapped onto and annotated with a CUBIC-Atlas based on an 8-week-old mouse brain. Cerebral cortical layers of somatosensory areas, posterior parietal association areas, and visual areas with annotations are visualized with pseudo colors. On the left, red squares indicate the approximate positions of the magnified brain regions shown in the right. Experiments were repeated three times with independent brains. The representative images are shown. L1, layer 1; L2/3, layer 2/3; L4, layer 4; L5, layer 5; L6a, layer 6a; L6b, layer 6b. Scale bars indicate 1000 μm in the scale of an “after-CUBIC-X” brain.

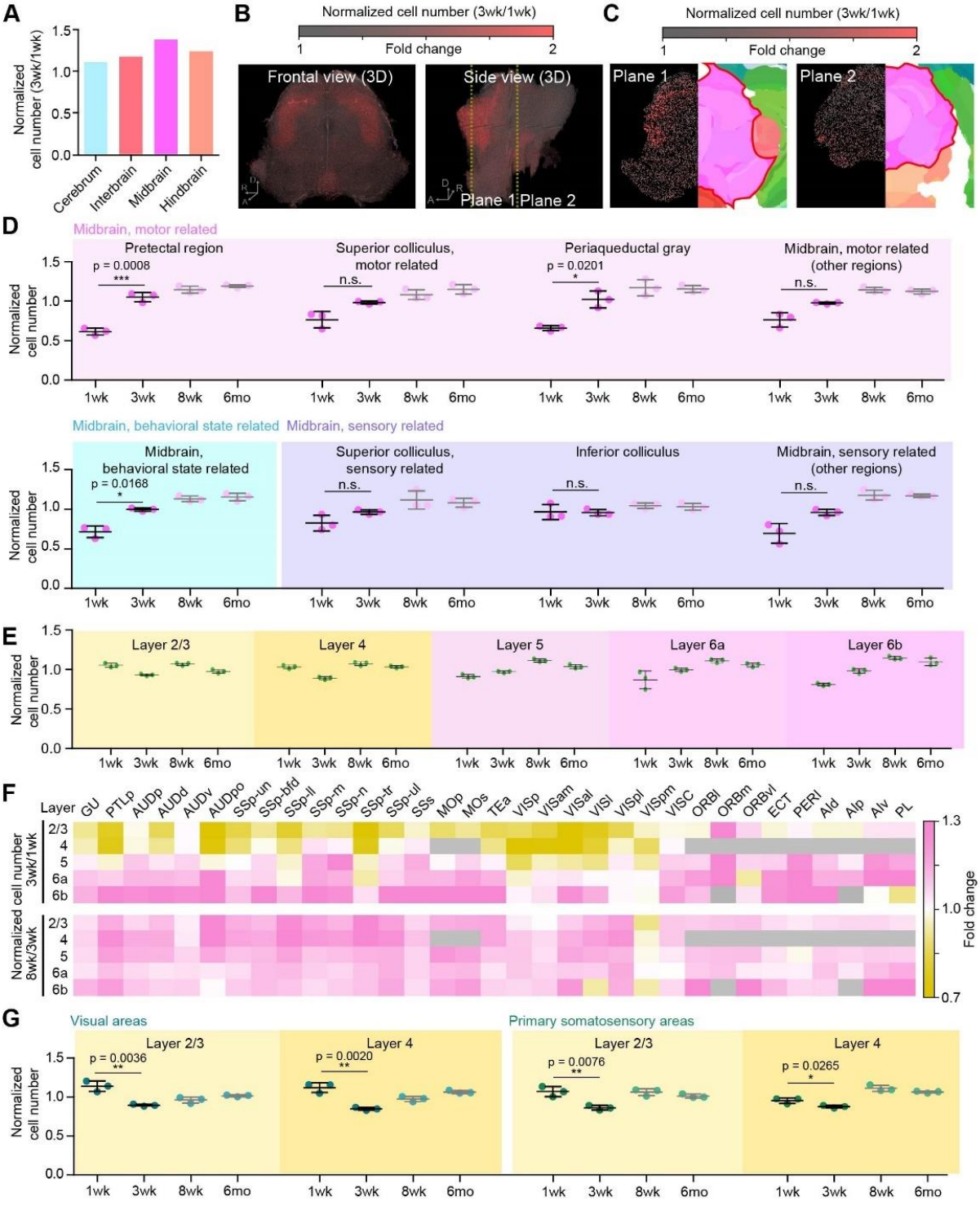

Figure 36. CUBIC-Atlas revealed a cell number increase in midbrain, and decrease in visual area and primary somatosensory area of cerebral cortex during early postnatal development.

(A) The normalized cell number in large brain areas. (B,C) The fold change of the normalized cell number in the midbrain during early postnatal development (1- to 3-week-old). The fold changes of the normalized cell number are shown in a volume rendered image (B), and single-plane images with the corresponding anatomical areas (C) of the midbrain. (D) The significant increase of the normalized cell number in the midbrain ($n = 3$, $^{***}p < 0.001$, $^{*}p < 0.05$, independent two-tailed t-test). Background color represents each classification of the midbrain (Pink for motor-related areas, blue for behavioral-state-related areas and purple for sensory-related areas, respectively). (E) The normalized cell number in each layer of the cerebral cortex ($n = 3$). (F) The fold change of the normalized cell number in the cerebral cortex during early postnatal period from 1- to 3-week old (upper) or during maturation period from 3- to 8-week old (lower). To calculate fold changes, mean values of normalized cell number of each age ($n = 3$) were used. (G) The significant decreases of the normalized cell number in visual area and primary somatosensory area of the cerebral cortical areas ($n = 3$, $^{**}p < 0.01$, $^{*}p < 0.05$, independent two-tailed t-test). All values are mean $\pm$ SD.

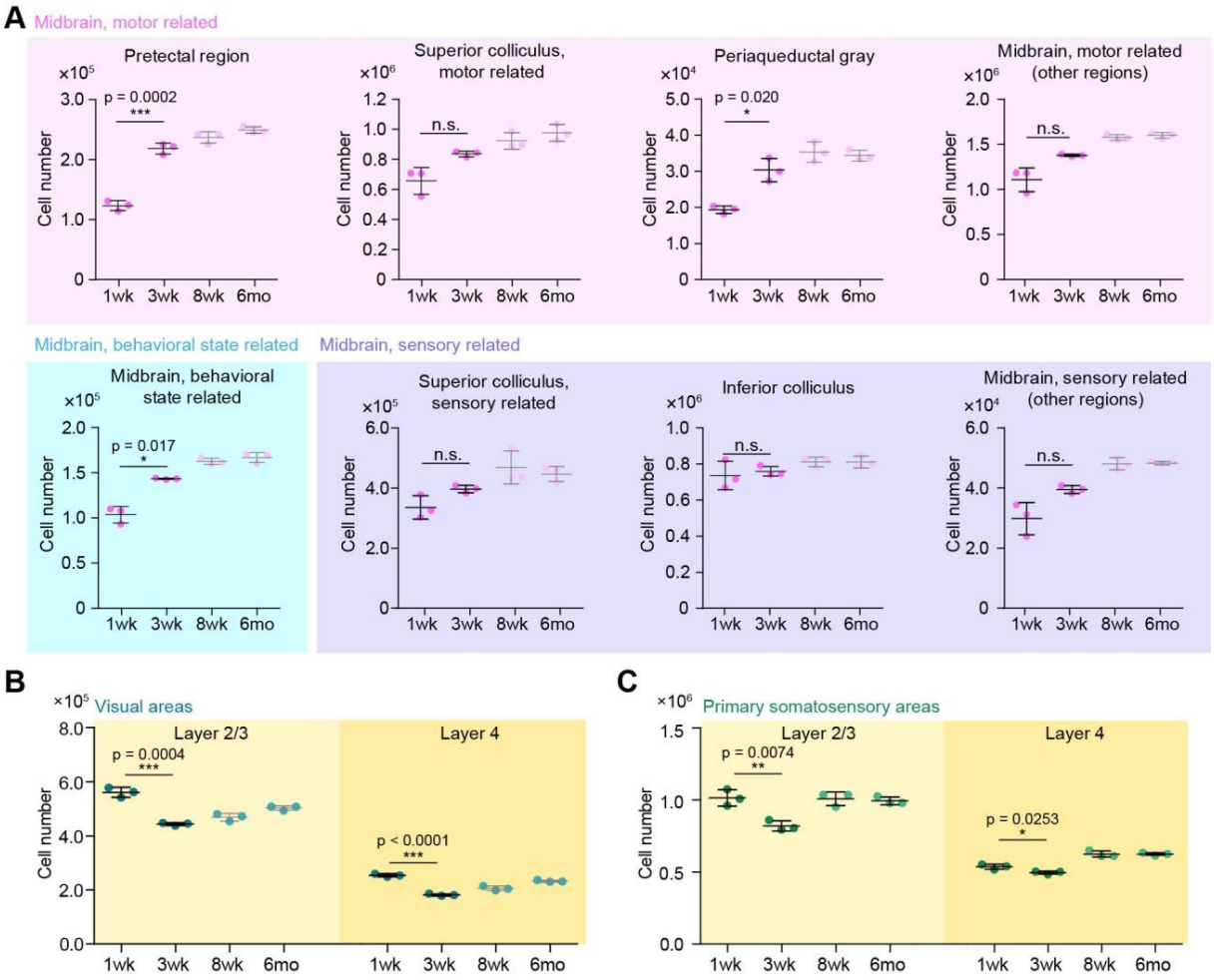

Figure 37. Whole-brain cell profiling over different developmental stages.

(A) The significant increase of the total cell number in the midbrain (n = 3, ***p < 0.001, *p < 0.05, independent two-tailed t-test). Background color represents each classification of the midbrain (Pink for motor-related areas, blue for behavioral-state-related areas and purple for sensory-related areas, respectively). (B,C) The significant decrease in the total cell number in visual areas (B) and primary somatosensory areas (C) of the cerebral cortex areas (n = 3, *** p < 0.001, **p < 0.01, *p < 0.05, independent two-tailed t-test). The average ± SD are shown.

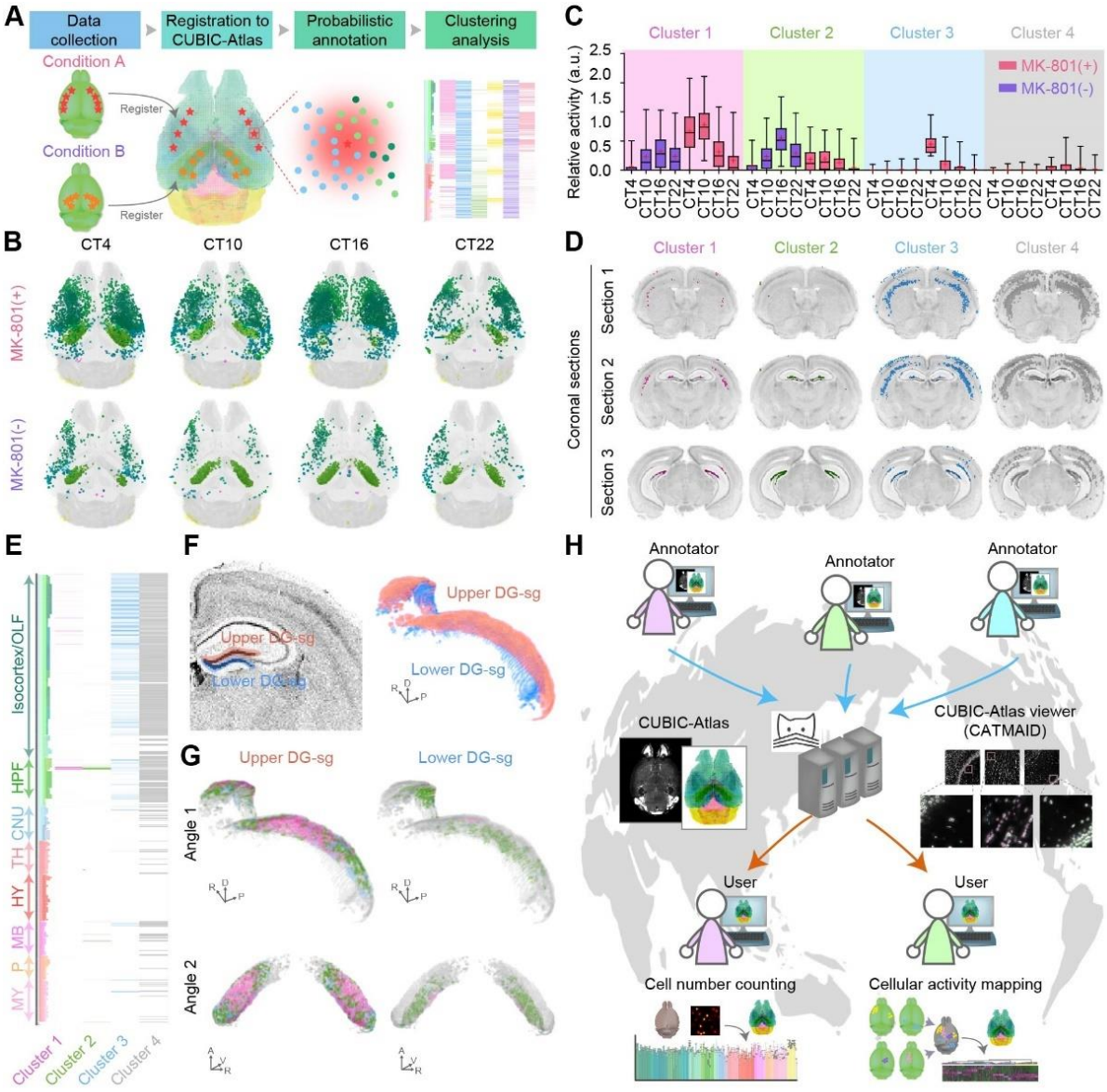

Figure 38. Probabilistic annotation of CUBIC-Atlas revealed a functionally distinct structure in granule cell layer of hippocampal dentate gyrus.

(A) Strategic schema of area discovery with probabilistically annotated CUBIC-Atlas. (B) Temporal variation of distribution of hyper-activated cells in the whole brain. Original image data were obtained in our previous study (Tatsuki et al., 2016), and re-analyzed in this study. Arc-dVenus expressing cells in mice with or without the chronic administration of MK-801 are shown. The color represents an anatomical area of the detected cells. The representative eight brains are shown. (C) Temporal variation of relative cellular activity in each cluster with or without administration of MK-801. Box plots indicate median and interquartile ranges. Whiskers of the box plot indicate the 2% and 98% percentile, along with a box showing

25−75% interquartile range, a dot showing the average and center line showing the median. (D,E) Spatial distribution of each cluster. (D) Each cluster was mapped onto the virtual coronal section of the mouse brain. (E) Heat-map view of the distribution of cluster with parental hierarchical structure is shown. (F) Overview of upper or lower of the granule cell layer of DG (DG-sg). Coronal slice view (left) and 3D reconstructed view (right) are shown. (G) 3D view of spatial distribution of four clusters on DG-sg. Images are shown from two different angles after volume rendering. When clusters on upper DG-sg are shown, lower DG-sg is shown as grey (left). When clusters on lower DG-sg are shown, upper DG-sg is shown as grey (right). For C-E and G, clustering analysis was performed with the twenty brains (MK-801(+); n = 3, MK-801(-); n = 2, four time points). (H) Concept of the data-sharing platform of CUBIC-Atlas via an open source web-based viewer and editor, the Collaborative Annotation Toolkit for Massive Amounts of Image Data (CATMAID).

BIBLIOGRAPHY

Abe, T., Kiyonari, H., Shioi, G., Inoue, K.I., Nakao, K., Aizawa, S., and Fujimori, T. (2011). Establishment of conditional reporter mouse lines at ROSA26 locus for live cell imaging. Genesis *49*, 579–590.

Amat, F., Hockendorf, B., Wan, Y., Lemon, W.C., McDole, K., and Keller, P.J. (2015). Efficient processing and analysis of large-scale light-sheet microscopy data. Nat Protoc *10*, 1679-1696.

Amat, F., Lemon, W., Mossing, D.P., McDole, K., Wan, Y., Branson, K., Myers, E.W., and Keller, P.J. (2014). Fast, accurate reconstruction of cell lineages from large-scale fluorescence microscopy data. Nat Methods *11*, 951-958.

Amato, S.P., Pan, F., Schwartz, J., and Ragan, T.M. (2016). Whole Brain Imaging with Serial Two-Photon Tomography. Front Neuroanat *10*, 31.

Amunts, K., Lepage, C., Borgeat, L., Mohlberg, H., Dickscheid, T., Rousseau, M.E., Bludau, S., Bazin, P.L., Lewis, L.B., Oros-Peusquens, A.M., *et al.* (2013). BigBrain: an ultrahigh-resolution 3D human brain model. Science *340*, 1472-1475.

Aoyagi, Y., Kawakami, R., Osanai, H., Hibi, T., and Nemoto, T. (2015). A rapid optical clearing protocol using 2,2'-thiodiethanol for microscopic observation of fixed mouse brain. PLoS ONE *10*, e0116280.

Avants, B.B., Tustison, N.J., Song, G., Cook, P.A., Klein, A., and Gee, J.C. (2011). A reproducible evaluation of ANTs similarity metric performance in brain image registration. Neuroimage *54*, 2033–2044.

Bakutkin, V.V., Maksimova, I.L., Semyonova, T.N., Tuchin, V.V., and Kon, I.L. (1995). Controlling of Optical Properties of Sclera. P Soc Photo-Opt Ins *2393*, 137-141.

Bashkatov, A.N., Tuchin, V.V., Genina, E.A., Sinichkin, Y.P., Lakodina, N.A., and Kochubey, V.I. (1999). The human sclera dynamic spectra: in vitro and in vivo measurements. Ophthalmic Technologies Ix, Proceedings Of *3591*, 311-319.

Bastian, M., Heymann, S., and Jacomy, M. (2009). Gephi: an open source software for exploring and manipulating networks. Paper presented at: International AAAI Conference on Weblogs and Social Media.

Becker, K., Jährling, N., Saghafi, S., Weiler, R., and Dodt, H.U. (2012). Chemical clearing and dehydration of GFP expressing mouse brains. PLoS ONE *7*, e33916.

Bianconi, E., Piovesan, A., Facchin, F., Beraudi, A., Casadei, R., Frabetti, F., Vitale, L., Pelleri, M.C., Tassani, S., Piva, F., *et al.* (2013). An estimation of the number of cells in the human body. Annals of human biology *40*, 463-471.

Bria, A., and Iannello, G. (2012). TeraStitcher - a tool for fast automatic 3D-stitching of teravoxel-sized microscopy images. BMC bioinformatics *13*, 316.

Cai, R., Pan, C., Ghasemigharagoz, A., Todorov, M.I., Forstera, B., Zhao, S., Bhatia, H.S., Parra-Damas, A., Mrowka, L., Theodorou, D., *et al.* (2019). Panoptic imaging of transparent mice reveals whole-body neuronal projections and skull-meninges connections. Nat Neurosci *22*, 317-327.

Calabrese, E., Badea, A., Coe, C.L., Lubach, G.R., Shi, Y., Styner, M.A., and Johnson, G.A. (2015). A diffusion tensor MRI atlas of the postmortem rhesus macaque brain. Neuroimage *117*, 408-416.

Chance, B., Liu, H.L., Kitai, T., and Zhang, Y.T. (1995). Effects of Solutes on Optical-Properties of Biological-Materials - Models, Cells, and Tissues. Anal Biochem *227*, 351-362.

Chechik, G., Meilijson, I., and Ruppin, E. (1998). Synaptic pruning in development: A computational account. Neural Comput *10*, 1759-1777.

Chen, F., Tillberg, P.W., and Boyden, E.S. (2015). Expansion microscopy. Science *347*, 543-548.

Chhetri, R.K., Amat, F., Wan, Y., Hockendorf, B., Lemon, W.C., and Keller, P.J. (2015). Whole-animal functional and developmental imaging with isotropic spatial resolution. Nat Methods *12*, 1171-1178.

Chiang, A.S., Liu, Y.C., Chiu, S.L., Hu, S.H., Huang, C.Y., and Hsieh, C.H. (2001). Three-dimensional mapping of brain neuropils in the cockroach, Diploptera punctata. J Comp Neurol *440*, 1-11.

Choi, B., Tsu, L., Chen, E., Ishak, T.S., Iskandar, S.M., Chess, S., and Nelson, J.S. (2005). Determination of chemical agent optical clearing potential using in vitro human skin. Lasers Surg Med *36*, 72-75.

Chung, K., Wallace, J., Kim, S.Y., Kalyanasundaram, S., Andalman, A.S., Davidson, T.J., Mirzabekov, J.J., Zalocusky, K.A., Mattis, J., Denisin, A.K., *et al.* (2013). Structural and molecular interrogation of intact biological systems. Nature *497*, 332–337.

Cope, M., Delpy, D.T., Wray, S., Wyatt, J.S., and Reynolds, E.O. (1989). A CCD spectrophotometer to quantitate the concentration of chromophores in living tissue utilising the absorption peak of water at 975 nm. Advances in experimental medicine and biology *248*, 33-40.

Costantini, I., Ghobril, J.P., Di Giovanna, A.P., Mascaro, A.L., Silvestri, L., Mullenbroich, M.C., Onofri, L., Conti, V., Vanzi, F., Sacconi, L., *et al.* (2015). A versatile clearing agent for multi-modal brain imaging. Sci Rep *5*, 9808.

Cowan, W.M., Fawcett, J.W., O'Leary, D.D., and Stanfield, B.B. (1984). Regressive events in neurogenesis. Science *225*, 1258-1265.

Cullen-McEwen, L.A., Kett, M.M., Dowling, J., Anderson, W.P., and Bertram, J.F. (2003). Nephron number, renal function, and arterial pressure in aged GDNF heterozygous mice. Hypertension *41*, 335-340.

Dauer, W., and Przedborski, S. (2003). Parkinson's disease: mechanisms and models. Neuron *39*, 889-909.

Dodt, H.U., Leischner, U., Schierloh, A., Jährling, N., Mauch, C.P., Deininger, K., Deussing, J.M., Eder, M., Zieglgänsberger, W., and Becker, K. (2007). Ultramicroscopy: Three-dimensional visualization of neuronal networks in the whole mouse brain. Nat Methods *4*, 331–336.

Dong, H.W. (2008). Allen Reference Atlas. A Digital Color Brain Atlas of the C57BL/6J Male Mouse (John Wiley & Sons).

Ehata, S., Hanyu, A., Fujime, M., Katsuno, Y., Fukunaga, E., Goto, K., Ishikawa, Y., Nomura, K., Yokoo, H., and Shimizu, T. (2007). Ki26894, a novel transforming growth factor-β type I receptor kinase inhibitor, inhibits in vitro invasion and in vivo bone metastasis of a human breast cancer cell line. Cancer Sci *98*, 127-133.

Ertürk, A., Becker, K., Jährling, N., Mauch, C.P., Hojer, C.D., Egen, J.G., Hellal, F., Bradke, F., Sheng, M., and Dodt, H.U. (2012). Three-dimensional imaging of solvent-cleared organs using 3DISCO. Nat Protoc *7*, 1983–1995.

Fanselow, M.S., and Dong, H.W. (2010). Are the dorsal and ventral hippocampus functionally distinct structures? Neuron *65*, 7-19.

Feng, G.P., Mellor, R.H., Bernstein, M., Keller-Peck, C., Nguyen, Q.T., Wallace, M., Nerbonne, J.M., Lichtman, J.W., and Sanes, J.R. (2000). Imaging neuronal subsets in transgenic mice expressing multiple spectral variants of GFP. Neuron *28*, 41–51.

Frangi, A.F., Niessen, W.J., Vincken, K.L., and Viergever, M.A. (1998). Multiscale vessel enhancement filtering. Lect Notes Comput Sc *1496*, 130-137.

Gao, L. (2015). Extend the field of view of selective plan illumination microscopy by tiling the excitation light sheet. Opt Express *23*, 6102-6111.

Gao, R., Asano, S.M., Upadhyayula, S., Pisarev, I., Milkie, D.E., Liu, T.L., Singh, V., Graves, A., Huynh, G.H., Zhao, Y., *et al.* (2019). Cortical column and whole-brain imaging with molecular contrast and nanoscale resolution. Science *363*.

Gradinaru, V., Treweek, J., Overton, K., and Deisseroth, K. (2018). Hydrogel-Tissue Chemistry: Principles and Applications. Annual review of biophysics *47*, 355-376.

Greenbaum, A., Chan, K.Y., Dobreva, T., Brown, D., Balani, D.H., Boyce, R., Kronenberg, H.M., McBride, H.J., and Gradinaru, V. (2017). Bone CLARITY: Clearing, imaging, and computational analysis of osteoprogenitors within intact bone marrow. Sci Transl Med *9*, eaah6518.

Hagberg, A.A., Schult, D.A., and Swart, P.J. (2008). Exploring network structure, dynamics, and function using NetworkX. Paper presented at: Proceedings of the 7th Python in Science Conference (SciPy2008).

Hale, G.M., and Querry, M.R. (1973). Optical Constants of Water in the 200-nm to 200-microm Wavelength Region. Appl Opt *12*, 555-563.

Hama, H., Hioki, H., Namiki, K., Hoshida, T., Kurokawa, H., Ishidate, F., Kaneko, T., Akagi, T., Saito, T., Saido, T., *et al.* (2015). ScaleS: an optical clearing palette for biological imaging. Nat Neurosci *18*, 1518-1529.

Hama, H., Kurokawa, H., Kawano, H., Ando, R., Shimogori, T., Noda, H., Fukami, K., Sakaue-Sawano, A., and Miyawaki, A. (2011). Sca*l*e: a chemical approach for fluorescence imaging and reconstruction of transparent mouse brain. Nat Neurosci *14*, 1481–1488.

Hansen, C.M. (2007). Hansen solubility parameters: a user's handbook (CRC press).

Harries, J.E., Hukins, D.W.L., and Hasnain, S.S. (1986). Analysis of the Exafs Spectrum of Hydroxyapatite. J Phys C *19*, 6859-6872.

Harris, D.C. (2011). Quantitative Chemical Analysis 8th Edition (W. H. Freeman).

Hausen, P., and Dreyer, C. (1981). The Use of Polyacrylamide as an Embedding Medium for Immunohistochemical Studies of Embryonic-Tissues. Stain Technol *56*, 287-293.

Hawrylycz, M.J., Lein, E.S., Guillozet-Bongaarts, A.L., Shen, E.H., Ng, L., Miller, J.A., van de Lagemaat, L.N., Smith, K.A., Ebbert, A., Riley, Z.L., *et al.* (2012). An anatomically comprehensive atlas of the adult human brain transcriptome. Nature *489*, 391-399.

Hayashi-Takagi, A., Yagishita, S., Nakamura, M., Shirai, F., Wu, Y.I., Loshbaugh, A.L., Kuhlman, B., Hahn, K.M., and Kasai, H. (2015). Labelling and optical erasure of synaptic memory traces in the motor cortex. Nature *525*, 333-338.

Hensch, T.K. (2005). Critical period plasticity in local cortical circuits. Nat Rev Neurosci *6*, 877-888.

Herculano-Houzel, S., Messeder, D.J., Fonseca-Azevedo, K., and Pantoja, N.A. (2015). When larger brains do not have more neurons: increased numbers of cells are compensated by decreased average cell size across mouse individuals. Front Neuroanat *9*, 64.

Herculano-Houzel, S., Mota, B., and Lent, R. (2006). Cellular scaling rules for rodent brains. Proc Natl Acad Sci U S A *103*, 12138-12143.

Herculano-Houzel, S., Ribeiro, P., Campos, L., Valotta da Silva, A., Torres, L.B., Catania, K.C., and Kaas, J.H. (2011). Updated neuronal scaling rules for the brains of Glires (rodents/lagomorphs). Brain Behav Evol *78*, 302-314.

Hirshburg, J., Choi, B., Nelson, J.S., and Yeh, A.T. (2007). Correlation between collagen solubility and skin optical clearing using sugars. Lasers Surg Med *39*, 140-144.

Hoshino, Y., Nishida, J., Katsuno, Y., Koinuma, D., Aoki, T., Kokudo, N., Miyazono, K., and Ehata, S. (2015). Smad4 decreases the population of pancreatic cancer–initiating cells through transcriptional repression of ALDH1A1. Am J Pathol *185*, 1457-1470.

Hou, B., Zhang, D., Zhao, S., Wei, M., Yang, Z., Wang, S., Wang, J., Zhang, X., Liu, B., Fan, L., *et al.* (2015). Scalable and DiI-compatible optical clearance of the mammalian brain. Front Neuroanat *9*, 19.

Hua, L., Zhou, R.H., Thirumalai, D., and Berne, B.J. (2008). Urea denaturation by stronger dispersion interactions with proteins than water implies a 2-stage unfolding. Proc Natl Acad Sci U S A *105*, 16928-16933.

Inamura, N., Sugio, S., Macklin, W.B., Tomita, K., Tanaka, K.F., and Ikenaka, K. (2012). Gene induction in mature oligodendrocytes with a PLP-tTA mouse line. Genesis *50*, 424-428.

Jiang, J., and Wang, R.K. (2004). Comparing the synergistic effects of oleic acid and dimethyl sulfoxide as vehicles for optical clearing of skin tissue in vitro. Phys Med Biol *49*, 5283-5294.

Johnson, G.A., Badea, A., Brandenburg, J., Cofer, G., Fubara, B., Liu, S., and Nissanov, J. (2010). Waxholm space: An image-based reference for coordinating mouse brain research. Neuroimage *53*, 365–372.

Johnsson, M.S.A., and Nancollas, G.H. (1992). The Role of Brushite and Octacalcium Phosphate in Apatite Formation. Crit Rev Oral Biol Med *3*, 61-82.

Kanemaru, K., Sekiya, H., Xu, M., Satoh, K., Kitajima, N., Yoshida, K., Okubo, Y., Sasaki, T., Moritoh, S., Hasuwa, H., *et al.* (2014). In Vivo Visualization of Subtle, Transient, and Local Activity of Astrocytes Using an Ultrasensitive Ca2+ Indicator. Cell Rep *8*, 311-318.

Kasukawa, T., Masumoto, K.H., Nikaido, I., Nagano, M., Uno, K.D., Tsujino, K., Hanashima, C., Shigeyoshi, Y., and Ueda, H.R. (2011). Quantitative expression profile of distinct functional regions in the adult mouse brain. PLoS ONE *6*, e23228.

Ke, M.T., Fujimoto, S., and Imai, T. (2013). SeeDB: a simple and morphology-preserving optical clearing agent for neuronal circuit reconstruction. Nat Neurosci *16*, 1154–1161.

Ke, M.T., Nakai, Y., Fujimoto, S., Takayama, R., Yoshida, S., Kitajima, T.S., Sato, M., and Imai, T. (2016). Super-Resolution Mapping of Neuronal Circuitry With an Index-Optimized Clearing Agent. Cell Rep *14*, 2718-2732.

Keller, P.J., and Ahrens, M.B. (2015). Visualizing whole-brain activity and development at the single-cell level using light-sheet microscopy. Neuron *85*, 462-483.

Keller, P.J., Schmidt, A.D., Wittbrodt, J., and Stelzer, E.H.K. (2008). Reconstruction of zebrafish early embryonic development by scanned light sheet microscopy. Science *322*, 1065–1069.

Kim, S.Y., Cho, J.H., Murray, E., Bakh, N., Choi, H., Ohn, K., Ruelas, L., Hubbert, A., McCue, M., Vassallo, S.L., *et al.* (2015a). Stochastic electrotransport selectively enhances the transport of highly electromobile molecules. Proc Natl Acad Sci U S A *112*, E6274-6283.

Kim, Y., Venkataraju, K.U., Pradhan, K., Mende, C., Taranda, J., Turaga, S.C., Arganda-Carreras, I., Ng, L., Hawrylycz, M.J., Rockland, K.S., *et al.* (2015b). Mapping social behavior-induced brain activation at cellular resolution in the mouse. Cell Rep *10*, 292-305.

Kiviranta, I., Tammi, M., Lappalainen, R., Kuusela, T., and Helminen, H. (1980). The rate of calcium extraction during EDTA decalcification from thin bone slices as assessed with atomic absorption spectrophotometry. Histochem Cell Biol *68*, 119-127.

Klingberg, A., Hasenberg, A., Ludwig-Portugall, I., Medyukhina, A., Mann, L., Brenzel, A., Engel, D.R., Figge, M.T., Kurts, C., and Gunzer, M. (2017). Fully Automated Evaluation of Total Glomerular Number and Capillary Tuft Size in Nephritic Kidneys Using Lightsheet Microscopy. J Am Soc Nephrol *28*, 452-459.

Koutsoukos, P., Amjad, Z., Tomson, M.B., and Nancollas, G.H. (1980). Crystallization of Calcium Phosphates - Constant Composition Study. J Am Chem Soc *102*, 1553-1557.

Ku, T., Swaney, J., Park, J.Y., Albanese, A., Murray, E., Cho, J.H., Park, Y.G., Mangena, V., Chen, J., and Chung, K. (2016). Multiplexed and scalable super-resolution imaging of three-dimensional protein localization in size-adjustable tissues. Nat Biotechnol *34*, 973-981.

Kubota, S.I., Takahashi, K., Nishida, J., Morishita, Y., Ehata, S., Tainaka, K., Miyazono, K., and Ueda, H.R. (2017). Whole-Body Profiling of Cancer Metastasis with Single-Cell Resolution. Cell Rep *20*, 236-250.

Kuwajima, T., Sitko, A.A., Bhansali, P., Jurgens, C., Guido, W., and Mason, C. (2013). *Clear^{T}*: a detergent- and solvent-free clearing method for neuronal and non-neuronal tissue. Development *140*, 1364-1368.

Lein, E.S., Hawrylycz, M.J., Ao, N., Ayres, M., Bensinger, A., Bernard, A., Boe, A.F., Boguski, M.S., Brockway, K.S., Byrnes, E.J., *et al.* (2007). Genome-wide atlas of gene expression in the adult mouse brain. Nature *445*, 168-176.

Liu, Y.C., and Chiang, A.S. (2003). High-resolution confocal imaging and three-dimensional rendering. Methods *30*, 86-93.

Long, X., Colonell, J., Wong, A.M., Singer, R.H., and Lionnet, T. (2017). Quantitative mRNA imaging throughout the entire Drosophila brain. Nat Methods *14*, 703-706.

Matsushita, N., Okada, H., Yasoshima, Y., Takahashi, K., Kiuchi, K., and Kobayashi, K. (2002). Dynamics of tyrosine hydroxylase promoter activity during midbrain dopaminergic neuron development. J Neurochem *82*, 295-304.

Menegas, W., Bergan, J.F., Ogawa, S.K., Isogai, Y., Umadevi Venkataraju, K., Osten, P., Uchida, N., and Watabe-Uchida, M. (2015). Dopamine neurons projecting to the posterior striatum form an anatomically distinct subclass. Elife *4*.

Mikula, S., Trotts, I., Stone, J.M., and Jones, E.G. (2007). Internet-enabled high-resolution brain mapping and virtual microscopy. Neuroimage *35*, 9-15.

Murphy, K., van Ginneken, B., Reinhardt, J.M., Kabus, S., Ding, K., Deng, X., Cao, K., Du, K., Christensen, G.E., Garcia, V., *et al.* (2011). Evaluation of registration methods on thoracic CT: the EMPIRE10 challenge. IEEE Trans Med Imaging *30*, 1901–1920.

Murray, E., Cho, J.H., Goodwin, D., Ku, T., Swaney, J., Kim, S.Y., Choi, H., Park, Y.G., Park, J.Y., Hubbert, A., *et al.* (2015). Simple, Scalable Proteomic Imaging for High-Dimensional Profiling of Intact Systems. Cell *163*, 1500-1514.

Nagai, T., Nakamuta, S., Kuroda, K., Nakauchi, S., Nishioka, T., Takano, T., Zhang, X.J., Tsuboi, D., Funahashi, Y., Nakano, T., *et al.* (2016). Phosphoproteomics of the Dopamine

Pathway Enables Discovery of Rap1 Activation as a Reward Signal In Vivo. Neuron *89*, 550-565.

Ntziachristos, V. (2010). Going deeper than microscopy: the optical imaging frontier in biology. Nat Methods *7*, 603-614.

Oh, S.W., Harris, J.A., Ng, L., Winslow, B., Cain, N., Mihalas, S., Wang, Q., Lau, C., Kuan, L., Henry, A.M., *et al.* (2014). A mesoscale connectome of the mouse brain. Nature *508*, 207-214.

Okabe, M., Ikawa, M., Kominami, K., Nakanishi, T., and Nishimune, Y. (1997). 'Green mice' as a source of ubiquitous green cells. FEBS Lett *407*, 313-319.

Okamura-Oho, Y., Shimokawa, K., Takemoto, S., Hirakiyama, A., Nakamura, S., Tsujimura, Y., Nishimura, M., Kasukawa, T., Masumoto, K.H., Nikaido, I., *et al.* (2012). Transcriptome tomography for brain analysis in the web-accessible anatomical space. PLoS ONE *7*, e45373.

Pan, C., Cai, R., Quacquarelli, F.P., Ghasemigharagoz, A., Lourbopoulos, A., Matryba, P., Plesnila, N., Dichgans, M., Hellal, F., and Erturk, A. (2016). Shrinkage-mediated imaging of entire organs and organisms using uDISCO. Nat Methods *13*, 859-867.

Papp, E.A., Leergaard, T.B., Calabrese, E., Johnson, G.A., and Bjaalie, J.G. (2014). Waxholm Space atlas of the Sprague Dawley rat brain. Neuroimage *97*, 374-386.

Park, Y.G., Sohn, C.H., Chen, R., McCue, M., Yun, D.H., Drummond, G.T., Ku, T., Evans, N.B., Oak, H.C., Trieu, W., *et al.* (2018). Protection of tissue physicochemical properties using polyfunctional crosslinkers. Nat Biotechnol.

Preibisch, S., Saalfeld, S., and Tomancak, P. (2009). Globally optimal stitching of tiled 3D microscopic image acquisitions. Bioinformatics *25*, 1463–1465.

Priyakumar, U.D., Hyeon, C., Thirumalai, D., and MacKerell, A.D. (2009). Urea Destabilizes RNA by Forming Stacking Interactions and Multiple Hydrogen Bonds with Nucleic Acid Bases. J Am Chem Soc *131*, 17759-17761.

Ragan, T., Kadiri, L.R., Venkataraju, K.U., Bahlmann, K., Sutin, J., Taranda, J., Arganda-Carreras, I., Kim, Y., Seung, H.S., and Osten, P. (2012). Serial two-photon tomography for automated ex vivo mouse brain imaging. Nat Methods *9*, 255–258.

Regev, A., Teichmann, S.A., Lander, E.S., Amt, I., Benoist, C., Birney, E., Bodenmiller, B., Campbell, P., Carninci, P., Clatworthy, M., *et al.* (2017). The Human Cell Atlas. Elife *6*.

Renier, N., Adams, E.L., Kirst, C., Wu, Z., Azevedo, R., Kohl, J., Autry, A.E., Kadiri, L., Umadevi Venkataraju, K., Zhou, Y., *et al.* (2016). Mapping of Brain Activity by Automated Volume Analysis of Immediate Early Genes. Cell *165*, 1789-1802.

Renier, N., Wu, Z., Simon, D.J., Yang, J., Ariel, P., and Tessier-Lavigne, M. (2014). iDISCO: a simple, rapid method to immunolabel large tissue samples for volume imaging. Cell *159*, 896-910.

Rice, D., and Barone, S., Jr. (2000). Critical periods of vulnerability for the developing nervous system: evidence from humans and animal models. Environmental health perspectives *108 Suppl 3*, 511-533.

Richardson, D.S., and Lichtman, J.W. (2015). Clarifying Tissue Clearing. Cell *162*, 246-257.

Rohlfing, T., Kroenke, C.D., Sullivan, E.V., Dubach, M.F., Bowden, D.M., Grant, K.A., and Pfefferbaum, A. (2012). The INIA19 Template and NeuroMaps Atlas for Primate Brain Image Parcellation and Spatial Normalization. Front Neuroinform *6*, 27.

Royer, L.A., Lemon, W.C., Chhetri, R.K., Wan, Y.N., Coleman, M., Myers, E.W., and Keller, P.J. (2016). Adaptive light-sheet microscopy for long-term, high-resolution imaging in living organisms. Nat Biotechnol *34*, 1267-1278.

Rusu, R.B., and Cousins, S. (2011). 3D is here: Point Cloud Library (PCL). Ieee Int Conf Robot.

Saalfeld, S., Cardona, A., Hartenstein, V., and Tomancak, P. (2009). CATMAID: collaborative annotation toolkit for massive amounts of image data. Bioinformatics *25*, 1984-1986.

Sahay, A., and Hen, R. (2007). Adult hippocampal neurogenesis in depression. Nat Neurosci *10*, 1110-1115.

Santi, P.A., Johnson, S.B., Hillenbrand, M., GrandPre, P.Z., Glass, T.J., and Leger, J.R. (2009). Thin-sheet laser imaging microscopy for optical sectioning of thick tissues. Biotechniques *46*, 287-294.

Schindelin, J., Arganda-Carreras, I., Frise, E., Kaynig, V., Longair, M., Pietzsch, T., Preibisch, S., Rueden, C., Saalfeld, S., Schmid, B., *et al.* (2012). Fiji: An open-source platform for biological-image analysis. Nat Methods *9*, 676-682.

Schwarz, M.K., Scherbarth, A., Sprengel, R., Engelhardt, J., Theer, P., and Giese, G. (2015). Fluorescent-protein stabilization and high-resolution imaging of cleared, intact mouse brains. PLoS ONE *10*, e0124650.

Sealy, R.C., Felix, C.C., Hyde, J.S., and Swartz, H.M. (1980). CHAPTER 7 - Structure and Reactivity of Melanins: Influence of Free Radicals and Metal Ions A2 - Pryor, William A. In Free Radicals in Biology (Academic Press), pp. 209-259.

Seiriki, K., Kasai, A., Hashimoto, T., Schulze, W., Niu, M., Yamaguchi, S., Nakazawa, T., Inoue, K.I., Uezono, S., Takada, M., *et al.* (2017). High-Speed and Scalable Whole-Brain Imaging in Rodents and Primates. Neuron *94*, 1085-1100 e1086.

Serper, A., and Calt, S. (2002). The demineralizing effects of EDTA at different concentrations and pH. J Endodont *28*, 501-502.

Sharpe, J. (2004). Optical projection tomography. Annu Rev Biomed Eng *6*, 209-228.

Shimada, T., Kato, K., Kamikouchi, A., and Ito, K. (2005). Analysis of the distribution of the brain cells of the fruit fly by an automatic cell counting algorithm. Physica A Stat Mech Appl *350*, 144-149.

Smith, R.M., Martell, A.E., and Motekaitis, R.J. (2003). NIST Standard Reference Database 46. *Critically Selected Stability Constants of Metal Complexes Database*. US National Institute of Standards and Technology Standard Reference Data Program; Gaithersburg, MD 20899.

Sousa, A.M.M., Meyer, K.A., Santpere, G., Gulden, F.O., and Sestan, N. (2017). Evolution of the Human Nervous System Function, Structure, and Development. Cell *170*, 226-247.

Spalteholz, W. (1914). *Über das Durchsichtigmachen von menschlichen und tierischen Präparaten* (S. Hirzel, Leipzig).

Staudt, T., Lang, M.C., Medda, R., Engelhardt, J., and Hell, S.W. (2007). 2,2'-Thiodiethanol: A new water soluble mounting medium for high resolution optical microscopy. Microsc Res Tech *70*, 1–9.

Susaki, E.A., Tainaka, K., Perrin, D., Kishino, F., Tawara, T., Watanabe, T.M., Yokoyama, C., Onoe, H., Eguchi, M., Yamaguchi, S., *et al.* (2014). Whole-brain imaging with single-cell resolution using chemical cocktails and computational analysis. Cell *157*, 726-739.

Susaki, E.A., Tainaka, K., Perrin, D., Yukinaga, H., Kuno, A., and Ueda, H.R. (2015). Advanced CUBIC protocols for whole-brain and whole-body clearing and imaging. Nat Protoc *10*, 1709-1727.

Susaki, E.A., and Ueda, H.R. (2016). Whole-body and Whole-Organ Clearing and Imaging Techniques with Single-Cell Resolution: Toward Organism-Level Systems Biology in Mammals. Cell Chem Biol *23*, 137-157.

Sylwestrak, E.L., Rajasethupathy, P., Wright, M.A., Jaffe, A., and Deisseroth, K. (2016). Multiplexed Intact-Tissue Transcriptional Analysis at Cellular Resolution. Cell *164*, 792-804.

Tainaka, K., Kubota, S.I., Suyama, T.Q., Susaki, E.A., Perrin, D., Ukai-Tadenuma, M., Ukai, H., and Ueda, H.R. (2014). Whole-body imaging with single-cell resolution by tissue decolorization. Cell *159*, 911-924.

Tainaka, K., Kuno, A., Kubota, S.I., Murakami, T., and Ueda, H.R. (2016). Chemical Principles in Tissue Clearing and Staining Protocols for Whole-Body Cell Profiling. Annu Rev Cell Dev Biol *32*, 713-741.

Tanaka, K.F., Ahmari, S.E., Leonardo, E.D., Richardson-Jones, J.W., Budreck, E.C., Scheiffele, P., Sugio, S., Inamura, N., Ikenaka, K., and Hen, R. (2010). Flexible Accelerated STOP Tetracycline Operator-Knockin (FAST): A Versatile and Efficient New Gene Modulating System. Biol Psychiat *67*, 770-773.

Tanaka, K.F., Matsui, K., Sasaki, T., Sano, H., Sugio, S., Fan, K., Hen, R., Nakai, J., Yanagawa, Y., Hasuwa, H., *et al.* (2012). Expanding the repertoire of optogenetically targeted cells with an enhanced gene expression system. Cell Rep *2*, 397-406.

Tanaka, T., Fillmore, D., Sun, S.T., Nishio, I., Swislow, G., and Shah, A. (1980). Phase-Transitions in Ionic Gels. Phys Rev Lett *45*, 1636-1639.

Tatsuki, F., Sunagawa, G.A., Shi, S., Susaki, E.A., Yukinaga, H., Perrin, D., Sumiyama, K., Ukai-Tadenuma, M., Fujishima, H., Ohno, R., *et al.* (2016). Involvement of Ca(2+)-Dependent Hyperpolarization in Sleep Duration in Mammals. Neuron *90*, 70-85.

Treweek, J.B., Chan, K.Y., Flytzanis, N.C., Yang, B., Deverman, B.E., Greenbaum, A., Lignell, A., Xiao, C., Cai, L., Ladinsky, M.S., *et al.* (2015). Whole-body tissue stabilization and selective extractions via tissue-hydrogel hybrids for high-resolution intact circuit mapping and phenotyping. Nat Protoc *10*, 1860-1896.

Tsai, P.S., Kaufhold, J.P., Blinder, P., Friedman, B., Drew, P.J., Karten, H.J., Lyden, P.D., and Kleinfeld, D. (2009). Correlations of neuronal and microvascular densities in murine cortex

revealed by direct counting and colocalization of nuclei and vessels. J Neurosci *29*, 14553-14570.

Tseng, Y.H., Mou, C.Y., and Chan, J.C.C. (2006). Solid-state NMR study of the transformation of octacalcium phosphate to hydroxyapatite: A mechanistic model for central dark line formation. J Am Chem Soc *128*, 6909-6918.

Tuchin, V.V. (2015). Tissue optics and photonics: light-tissue interaction. J Biomed Photonics Eng *1*, 98-134.

Tuchin, V.V., Bashkatov, A.N., Genina, E.A., Kochubey, V.I., Lakodina, N.A., Simonenko, G.V., Sinichkin, Y.P., Proshina, Y.M., and Razumikhina, N.A. (1999). Optics of living tissues with controlled scattering properties. 1999 International Conference on Biomedical Optics (Bmo'99) *3863*, 10-21.

Tuchin, V.V., Maksimova, I.L., Zimnyakov, D.A., Kon, I.L., Mavlutov, A.K., and Mishin, A.A. (1996). Light propagation in tissues with controlled optical properties. Photon Propagation in Tissues Ii, Proceedings Of *2925*, 118-142.

Tuchin, V.V., Maksimova, I.L., Zimnyakov, D.A., Kon, I.L., Mavlyutov, A.H., and Mishin, A.A. (1997). Light propagation in tissues with controlled optical properties. J Biomed Opt *2*, 401-417.

Tuchin, V.V., Xu, X.Q., and Wang, R.K. (2002). Dynamic optical coherence tomography in studies of optical clearing, sedimentation, and aggregation of immersed blood. Appl Opt *41*, 258-271.

Vanderhaeghen, P., and Cheng, H.J. (2010). Guidance molecules in axon pruning and cell death. Cold Spring Harbor perspectives in biology *2*, a001859.

Vargas, G., Chan, K.F., Thomsen, S.L., and Welch, A.J. (2001). Use of osmotically active agents to alter optical properties of tissue: Effects on the detected fluorescence signal measured through skin. Lasers Surg Med *29*, 213-220.

Vargas, O., Chan, E.K., Barton, J.K., Rylander, H.G., and Welch, A.J. (1999). Use of an agent to reduce scattering in skin. Lasers Surg Med *24*, 133-141.

Velez-Fort, M., Rousseau, C.V., Niedworok, C.J., Wickersham, I.R., Rancz, E.A., Brown, A.P., Strom, M., and Margrie, T.W. (2014). The stimulus selectivity and connectivity of layer six

principal cells reveals cortical microcircuits underlying visual processing. Neuron *83*, 1431-1443.

von Bartheld, C.S., Bahney, J., and Herculano-Houzel, S. (2016). The search for true numbers of neurons and glial cells in the human brain: A review of 150 years of cell counting. J Comp Neurol *524*, 3865-3895.

Vousden, D.A., Epp, J., Okuno, H., Nieman, B.J., van Eede, M., Dazai, J., Ragan, T., Bito, H., Frankland, P.W., Lerch, J.P., *et al.* (2015). Whole-brain mapping of behaviourally induced neural activation in mice. Brain Struct Funct *220*, 2043-2057.

Wang, L.J., and Nancollas, G.H. (2008). Calcium Orthophosphates: Crystallization and Dissolution. Chem Rev *108*, 4628-4669.

Wang, R.K.K., Xu, X.Q., Tuchin, V.V., and Elder, J.B. (2001). Concurrent enhancement of imaging depth and contrast for optical coherence tomography by hyperosmotic agents. J Opt Soc Am B *18*, 948-953.

Warnes, G.R., Bolker, B., Bonebakker, L., Gentleman, R., Huber, W., Liaw, A., Lumley, T., Maechler, M., Magnusson, A., Moeller, S., *et al.* (2009). gplots: Various R programming tools for plotting data. R package version *2*.

Weast, R.C. (1983). CRC Handbook of Chemistry and Physics 62nd Edition (CRC Press, Inc).

Wray, S., Cope, M., Delpy, D.T., Wyatt, J.S., and Reynolds, E.O. (1988). Characterization of the near infrared absorption spectra of cytochrome aa3 and haemoglobin for the non-invasive monitoring of cerebral oxygenation. Biochim Biophys Acta *933*, 184-192.

Xu, X.Q., and Wang, R.K.K. (2003). The role of water desorption on optical clearing of biotissue: Studied with near infrared reflectance spectroscopy. Med Phys *30*, 1246-1253.

Yang, B., Treweek, J.B., Kulkarni, R.P., Deverman, B.E., Chen, C.K., Lubeck, E., Shah, S., Cai, L., and Gradinaru, V. (2014). Single-cell phenotyping within transparent intact tissue through whole-body clearing. Cell *158*, 945-958.

Zhang, M., Wu, T., and Bennett, K.M. (2015). Small blob identification in medical images using regional features from optimum scale. IEEE Trans Biomed Eng *62*, 1051-1062.

Zhu, D., Larin, K.V., Luo, Q.M., and Tuchin, V.V. (2013). Recent progress in tissue optical clearing. Laser Photonics Rev *7*, 732-757.

Zimnyakov, D.A., Tuchin, V.V., Mishin, A.A., Kon, I.L., and Serov, A.N. (1996). In-vitro human sclera structure analysis using tissue optical immersion effect. Ophthalmic Technologies Vi, Proceedings Of *2673*, 233-242.